ornl

OAK RIDGE NATIONAL LABORATORY

LOCKHEED MARTIN

ORNL/HTSPC-7

ORNL Superconducting Technology Program for Electric Power Systems

Annual Report for FY 1995

MANAGED AND OPERATED BY
LOCKHEED MARTIN ENERGY RESEARCH CORPORATION
FOR THE UNITED STATES
DEPARTMENT OF ENERGY

ORNL-27 (3-96)

ORNL/HTSPC-7

ORNL SUPERCONDUCTING TECHNOLOGY PROGRAM FOR ELECTRIC POWER SYSTEMS

ANNUAL REPORT FOR FY 1995

Compiled by
R. A. Hawsey

Edited by
J. W. Turner

Manuscript Completed: March 1996
Date Published: May 1996

Prepared for the
Office of Utility Technologies
Office of Energy Efficiency and Renewable Energy
U.S. DEPARTMENT OF ENERGY
(AK 06 00 00 0)

Prepared by
OAK RIDGE NATIONAL LABORATORY
P.O. Box 2008
Oak Ridge, TN 37831-6285
Managed by
LOCKHEED MARTIN ENERGY RESEARCH CORPORATION
for the
U.S. DEPARTMENT OF ENERGY
under contract DE-AC05-96OR22464

Contributors

J. D. Budai
D. K. Christen
A. Goyal
R. A. Hawsey
Q. He[1]
H. Hsu[2]
D. R. James
E. C. Jones[3]
H. R. Kerchner
D. M. Kroeger
D. F. Lee[3]
F. A. List
M. S. Lubell
J. W. Lue
P. M. Martin
B. W. McConnell
H. E. McCoy
D. P. Norton
M. Paranthaman
B. Saffian[1]
S. W. Schwenterly
V. Selvamanickam[4]
S. S. Shoup[3]
V. K. Sikka
E. D. Specht
J. E. Tkaczyk[5]
M. Tomsic[6]
R. K. Williams

---

[1]The University of Tennessee
[2]Imtech Corporation
[3]Postdoctoral research fellow
[4]Intermagnetics General Corporation
[5]General Electric Corporate Research and Development
[6]Plastronic, Inc.

Note: Photomicrographs in this document were produced electronically and archived (No. 96/1091) by ORNL Graphics and Imaging Services.

Contents

List of Figures

List of Tables

Acronyms and Initialisms

ADC	analog-to-digital converter
ANL	Argonne National Laboratory
CRADA	cooperative research and development agreement
CSL	coincident site lattice
DAC	digital-to-analog converter
DOE	U.S. Department of Energy
DOE-HQ	DOE Headquarters
EBSP	electron backscatter diffraction patterns
EDS	energy-dispersive spectroscopy
EPRI	Electric Power Research Institute
FWHM	full width half maximum
GE	General Electric Company
HTS	high-temperature superconductivity/superconductor
IBAD	ion-beam-assisted deposition
IBM	International Business Machines
IGC	Intermagnetics General Corporation
LANL	Los Alamos National Laboratory
NIST	National Institute of Standards and Technology
ORNL	Oak Ridge National Laboratory
PIT	powder-in-tube
RABiTS	rolling-assisted biaxially textured substrates
SEM	scanning electron microscopy
SUNY	State University of New York
TCSUH	Texas Center for Superconductivity at the University of Houston
TEM	transmission electron microscopy
TOC	total owning cost
UT	The University of Tennessee
WDC	Wireless Data Corporation
XRD	X-ray diffraction

Executive Summary

The Oak Ridge National Laboratory (ORNL) Superconducting Technology Program is conducted as part of a national effort by the U.S. Department of Energy's Office of Energy Efficiency and Renewable Energy to develop the science and technology base needed by U.S. industry for commercial development of electric power applications of high-temperature superconductivity. The two major elements of this program are wire development and systems development. This document describes the major research and development activities for this program together with related accomplishments. The technical progress reported was summarized from information prepared for the FY 1995 Annual Program Review held August 1–2, 1995. This ORNL program is highly leveraged by the staff and other resources of U.S. industry and universities. In fact, nearly three-fourths of the ORNL effort is devoted to cooperative projects with private companies. Interlaboratory teams are also in place on a number of industry-driven projects. Patent disclosures, working group meetings, staff exchanges, and joint publications and presentations ensure that there *is* technology transfer with U.S. industry. Working together, the collaborative teams are making rapid progress in solving the scientific and technical issues necessary for the commercialization of long lengths of practical high-temperature superconductor wire and wire-using systems.

Highlights for Fiscal Year 1995

- U.S. Patent No. 5,357,756 was issued on October 25, 1994, for Oak Ridge National Laboratory's (ORNL's) "Biopolar Pulse Field for Magnetic Refrigeration"—the first patent for Superconducting Technology Program technology development.

- Stability and normal zone propagation experiments were completed on a single length of conductor and on a double-pancake coil made of Bi-2223/silver tape. No sustained normal zones were observed during local pulsed heating of the material. In addition, for the cases when spontaneous quenches were experienced in the double-pancake coil (presumably caused by the accumulation and spreading of large amounts of heat generated at a low critical current density segment of the wire), no normal front propagation was measured. ORNL and American Superconductor Corporation (ASC) demonstrated that coils designed for good radial and axial heat conduction will result in ultrastable power devices such as motors, generators, and transformers.

- Using proton irradiation, ORNL researchers produced the first evidence of enhanced performance of the thallium-based superconductors. In collaboration with Los Alamos National Laboratory and International Business Machines Corporation, TI-1223 spray-pyrolyzed deposits on yttria-stablized zirconia were irradiated with protons to create random fission tracks that enhance the ability of the material to carry current in the presence of a magnetic field. Nearly an order of magnitude improvement in critical current density was obtained at 2 T, moving the current density closer to a technologically useful range.

- ORNL researchers conducted novel pulsed current experiments to show that, for YBCO wires with relative resistivities approaching 3% of silver, an operational current density of 75,000 A/cm^2 may be achieved relatively independent of the "quality" of the wires. This operational current density is well above the critical current density of the superconductor. ORNL concluded that many wires with relatively "low" critical current densities could be used at 77 K, in the dissipative regime, if the trade-off of high refrigeration load can be accommodated.

- ORNL researchers performed transport property measurements of TI-1223 thick deposited conductors. The irreversibility field of thick (10–30 μm) thallium deposits on silver is systematically larger than that of thinner yet higher critical current density deposits on yttria-stabilized zirconia. These results are the first to suggest that thallium films on silver are produced with additional grown-in defects that enhance flux pinning and, hence, the transport current at the high applied magnetic fields that will be present in electric machines.

- ORNL researchers successfully increased the rate of production of their aerosol pyrolysis system to >10 g/h. This increased rate of production will greatly facilitate aerosol powder-in-tube (PIT) processing experiments for the cooperative agreements with industry.

- In partnership with five other national laboratories and numerous industries and universities, ORNL staff chaired and developed the agenda for the successful High-Temperature Superconducting Wire Development Workshop held January 31–February 1, 1995. Hosted once again by Florida Power Corporation, the workshop was attended by a record 80 participants representing a broad range of stakeholders. Priority areas for wire development were identified, and several new avenues for collaboration were discussed during the meeting.

- ORNL staff unveiled a new demonstration motor based on commercial high-temperature superconducting (HTS) wire at the EnvironMental Fair held in October 1994 in Oak Ridge. The motor was also demonstrated at the Technology 2004 Conference, Office of Energy Management booth, in Washington, D.C., in November 1994. The motor was developed for demonstrating applications of the new superconducting wires to electric power systems such as motors and generators. Designed primarily for educational use at area schools, museums, and for visitors to ORNL, the 0.91-kg (2-lb) motor uses liquid nitrogen to cool the superconductor.

- Eight new Disclosures of Possible Subject Invention based on Superconducting Technology Program technology (a new record) were submitted to the U.S. Department of Energy's Oak Ridge Operations Office during the first half of FY 1995.

- ORNL researchers designed, developed, and tested a new automated system for measurement of the critical current of HTS wires. The system will enable rapid screening of wire samples up to 5-cm (2-in.) long as a function of temperature, magnetic field, and field orientation. The closed-cycle refrigerated system enables cost-effective testing of wires made by ORNL and many of the industrial collaborators in the program at 20–90 K. This unique apparatus is fully automated, requires no user interaction, and does not rely on refills of expensive liquid helium.

- ORNL researchers completed microstructural examination of some of the highest critical current density Bi-2223 PIT tapes. The examinations reveal that 40% of the grain boundaries are "small angle" and that the superconductor texture permits increased percolative flow of supercurrent. In addition, a mechanism for current flow perpendicular to the tape surface, without the need to traverse basal plane twist boundaries, was determined. These results help in understanding the mechanisms for high current flow in the best BSCCO wires.

- Using ORNL's aerosol decomposition process, optimal compositions that lead to highly phased pure thallium/lead-based HTS powders were produced. The thallium-lead-1223 phase forms were for lead levels ≤ 0.3 to ≤ 0.5 in the powder $(Tl_{1-x}Pb_x)_{1.15}(Sr_{1.6}Ba_{0.4})Ca_2Cu_3Ag_{0.4}O_y$. The critical temperatures for these samples varied from 105 to 116 K. Reliable chemical routes are needed for production of phase-pure powders for use in tapes and thick-film, or "deposited," wires. Because of their high critical temperature and relatively good properties in background magnetic fields, these compositions may be useful for superconducting wire applications above 40 K.

- Alternating-current (ac) power loss measurements were made on a series of high-quality, twisted, multifilamentary BSCCO-2223/silver superconducting tapes produced by ASC. For one sample wire, the 60-Hz power loss was ~50 mW at 77 K and in a 750-G background field. The ac losses are induced by applying either an external field ranging from 45 to 500 Hz with peak amplitudes up to 1300 G [in a 10.2 cm (4-in.) bore] or an ac transport current of up to 100 A, or both. The calorimeter is sensitive in the milliwatt range, and the data are in close agreement with those measured by industry. The first tests with the calorimeter revealed that the hysteretic and eddy/coupling losses can be easily determined. The latter form of loss can occur when superconducting filaments touch each other inside a wire or when the sheath material is in contact through different layers of the test coil.

- The critical current of short lengths of surface-coated Bi-2212/silver tape conductors was measured for a range of temperature (25–77 K), externally applied magnetic field (0–1.5 T), and field orientation (−90° to +90°). The wires were supplied by industry, and the new ORNL automated system was used for determinations of the critical current. For zero-applied magnetic fields, critical currents ranged from 75 A at 25 K to 2 A at 77 K. More recent samples approach 8 A at 77 K. In all cases critical currents decrease with applied fields, as expected. Moreover, owing to the anisotropy of Bi-2212, the

ratio of critical current with field applied perpendicular to the tape surface to the critical current with field applied parallel decreases with increasing field and decreases rapidly at higher temperatures. Such behavior is undesirable for applications involving randomly oriented fields, such as motors and generators.

- Three variants of the $TlBa_2Ca_2Cu_3O_x$ (Tl-1223) superconductor wire were synthesized. The materials were fabricated as bulk, phase-pure Tl-1223 and also strontium (TBS-1223) and lead-substituted (TP-1223) compounds by solid state reaction of the individual metal oxides. The work was motivated by evidence in the literature that substituted materials may offer advantages in magnetic field-dependent properties, phase formation, and stability. The TP-1223 has the largest irreversibility field and the weakest temperature dependence, indicating that the flux pinning is more effective in the lead-substituted materials.

- Using an all-alkoxide, sol-gel, dip-coating technique, highly *c*-axis-oriented TlBaCaCuO (Tl-1223) deposits on silver substrates were grown. Sol-gel processing is an inexpensive method of general utility for the formation of ceramic coatings and powders. The measured critical current density of ~19,000 A/cm^2 at 77 K and zero field is consistent with a high-quality Tl-1223 film.

- Critical current measurements at 77 K were completed on a 10-cm (4-in.) section of an 8.2-m (27-ft) tape fabricated by Plastronic, Inc. Plastronic uses a unique "tubular wire process," adapted from the welding wire industry, to produce HTS tapes. A 39-cm (15.4-in.) section was divided into ten 3.8-cm (1.5-in.) lengths, and the observed critical current varied between 3.5 and 9.0 A. Experiments to insulate these tapes with Aquadag, a colloidal graphite suspension, were initiated. Aquadag may be useful for insulation of low-voltage dc coils. At room temperature the resistance between two tape layers was 0.05–0.1 Ω, but this increased by an order of magnitude at 77 K.

- "Evaluation of Technology Transfer by Peer Review" was selected by the *Journal of Technology Transfer* as their finest article for 1994. Coauthored by T. P. Sheahen, R. E. Rosenthal, S. W. Freiman, R. A. Hawsey, and J. G. Daley, the paper received the Gold Award at the Annual Conference of the Technology Transfer Society on July 18, 1995.

- The "1223" structural type of an HTS, $(Tl_{0.8}Bi_{0.2})(Sr_{1.6}Ba_{0.4})Ca_2Cu_3O_{9-\delta}$ (referred to as Tl,Bi-1223), based on oxides of thallium and bismuth was prepared by reaction of prereacted powders of $(Sr_{1.6}Ba_{0.4})Ca_2Cu_3O_7$ with Tl_2O_3 and Bi_2O_3. The "as-synthesized material" has a superconducting transition temperature (T_c) of 113 K, which is relatively unaffected by postannealing either in an oxygen or argon atmosphere. Polycrystalline samples of Tl,Bi-1223 exhibit a high persistent current density (J_p) of 1.62×10^7 A/cm^2 at 5 K and 1 T, and maintain significant J_p values to temperatures over 60 K. The structure of Tl,Bi-1223 has been refined using neutron powder diffraction data.

- The next generation of advanced power transformers is being developed by a vertically integrated research and development team consisting of Intermagnetics General Corporation (IGC), Waukesha Electric Systems (formerly the transformer division of MagneTek), Rochester Gas and Electric, and ORNL. The HTS transformer will provide lower operating losses and potentially lower total owning cost than today's equipment and will provide the nation's electric utilities and their customers with power transformers that offer reduced environmental hazards, enhanced fire safety, smaller size, and reduced noise and weight. Because electricity typically passes through four to five transformers between the generating station and the consumer, the energy savings impact of these advanced transformers can be multiplied several times when the technology becomes widespread. Success of the program depends on the availability of low-cost, high-temperature superconducting wires. IGC and

ORNL have been developing several families of HTS wires for electric power applications. The team plans to begin testing a 1-MVA, single-phase demonstration unit in early 1997.

- ORNL developed a quantitative model for percolative current flow in polycrystalline HTS wires. The model explains how large critical current densities are possible in materials in which only a small fraction of the grain boundaries are small angle. The model predicts that critical currents (I_c) in BSCCO tapes can be much higher than has been demonstrated (i.e., 3–30% of the single crystal I_c, depending on grain boundary misorientation angle, vs 0.5% for the best tapes made this far). In addition, in common with other models, the percolative model predicts that I_c will increase as the aspect ratio of grains increases.

- A new transport-current method for ac loss determination was implemented at ORNL. Tl-1223 thick films on polycrystalline YSZ and Bi-2223/silver tapes supplied by industry were studied. The product of the time-dependent current and voltage is averaged to determine power loss. For the BSCCO tape, an extremely weak dependence of the loss on frequency was measured, suggesting that filament coupling is the primary loss mechanism.

- The report titled *Rotor Instrumentation Study for High-Temperature Superconducting Generators* was submitted to GE in support of ORNL work on the Superconductivity Partnership Initiative Superconducting Generator Project. The objective was to develop a system for transmitting data from sensors in the spinning rotor to a stationary data acquisition system. Conventional electrical slip rings are not acceptable because of their noise and limited lifetime. Three possible methods of data transmission were identified, and data transmission systems using each were described and evaluated. The report contains extensive manufacturer data on recommended sensors and equipment for the various systems.

- Preliminary design and conceptual drawings for the 1-MVA HTS transformer were delivered to Waukesha Electric Systems. Design issues such as dc offset during surge and in-rush, voids in encapsulation material, and outgassing of welds for the tank are being addressed. Transformer coil forces are of the expected magnitude, and the design provides for proper winding and encapsulation to accommodate these forces.

- A new process called rolling-assisted biaxially textured substrates (RABiTS™) was developed to fabricate long lengths of flexible, near single-crystal-like, chemically compatible substrates. Superconducting deposits of $Y_1Ba_2Cu_3O_x$ on these substrates show sharp biaxial texture. The zero-field critical current density of early samples exceeds 8×10^4 A/cm^2 at 77 K. Moreover, the magnetic field behavior indicates that at least a small portion of the YBCO film is strongly linked. This new development may enable wires for use in applications requiring high (>1 T) magnetic fields that operate near liquid nitrogen temperature. Ten private companies visited Oak Ridge in September 1995 for commercialization strategy discussions.

Technical Progress in Wire Development

FABRICATION OF $(Bi,Pb)_2Sr_2Ca_2Cu_3O_{10}$ SUPERCONDUCTORS FROM Mg-DOPED AEROSOL PRECURSOR POWDER

Bismuth-based conductors are currently the only candidates for near-term conductor applications. Even though $(Bi,Pb)_2Sr_2Ca_2Cu_3O_{10}$ (Bi-2223) powder-in-tube (PIT) tapes can be utilized at 77 K, the range of applications for which such conductors are adequate would be greatly expanded by improvement of their J_c performance in a magnetic field. Consequently, ways to improve flux pinning in these materials are needed.

In the $YBa_2Cu_3O_x$ superconductor, inclusions such as Y_2BaCuO_5 result in improved flux pinning and enhanced J_c.[1] Because of the large Y_2BaCuO_5 particle size (typically 0.5–20 μm), whether enhanced pinning is due to the inclusions themselves or the atomic defects associated with the inclusions is still under debate. Nevertheless, it is generally agreed that the superconducting properties of the high-temperature superconductor (HTS) are enhanced when the majority of the inclusions are ≤ 1 μm.[2] Because of the similarities between various HTS compounds, the same beneficial effects should also be found in Bi-2223 as long as the inclusions do not react adversely with the HTS. In addition to the requirement of being chemically inert, the inclusions should also be much smaller than 1 μm and be homogeneously distributed throughout the grains. Magnesium oxide particles have been shown to be chemically compatible with Bi-2223 at elevated processing temperatures[3] and are a potential candidate as the inclusion phase. Because of problems involved in dispersing small agglomerates by mechanical means, the later requirement is difficult to accomplish if the particles are added after precursor formation. One alternative, then, is to dope the precursor solution chemically such that particle and precursor formation occur simultaneously. In this study, series of magnesium-doped precursor powders were prepared through an Oak Ridge National Laboratory (ORNL) patented aerosol technique. Preliminary results on the effects of dopant on Bi-2223 formation and transition temperature, as well as the characteristics of the inclusions, are presented.

Preparation of Magnesium-Doped Precursor Powders

Aerosol precursor solutions with stoichiometry $Bi_{1.80}Pb_{0.33}Sr_{1.87}Ca_{1.99}Cu_{3.00}Mg_yO_x$ ($y = 0$, 1.01, 2.02), which correspond to 0, 6.7, and 13.4 vol % magnesium oxide contents, were prepared using the standard processing procedure developed at ORNL.[4] Phase analyses of these precursor powders using X-ray diffraction (XRD) revealed that the magnesium-doped powders are identical to the undoped one except for the presence of the magnesium oxide phase. Specimens weighing 2 g were pressed under a pressure of 500 MPa into 0.32-cm-diam (0.13-in.) pellets and were sintered at 845°C for various amounts of time in 7.5% oxygen. After sintering, portions of these specimens were ground into powder and examined by XRD for Bi-2223 conversion and the presence of magnesium oxide. Figure 1.1 shows the diffraction patterns of undoped Bi-2223 sintered for 12 h and Bi-2223 containing 6.7 and 14.6 vol % magnesium oxide after 24 h of sintering. This figure shows that the amount of 2212 in the specimens increases with magnesium doping. In addition, magnesium oxide is the only magnesium-bearing phase that is present in the magnesium-doped materials. These results indicate that while magnesium dopant may not react adversely with Bi-2223, its presence does affect the reaction kinetics of the HTS. Therefore, adjustments in the heat treatment schedule will have to be made to achieve an optimal phase content.

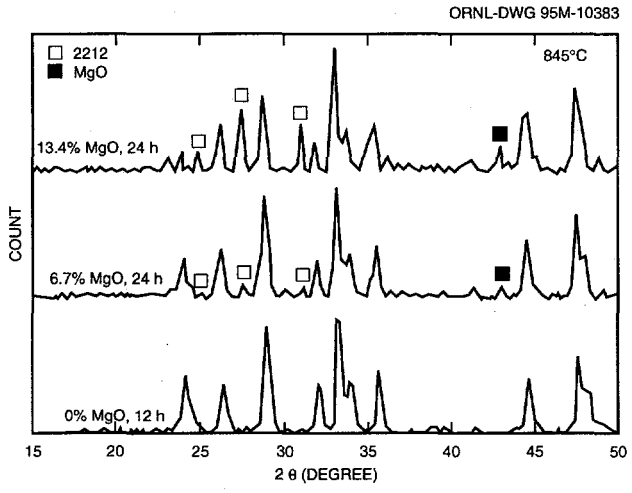

Fig. 1.1. Diffraction patterns of sintered Bi-2223 fabricated from magnesium-doped and undoped aerosol precursor powders.

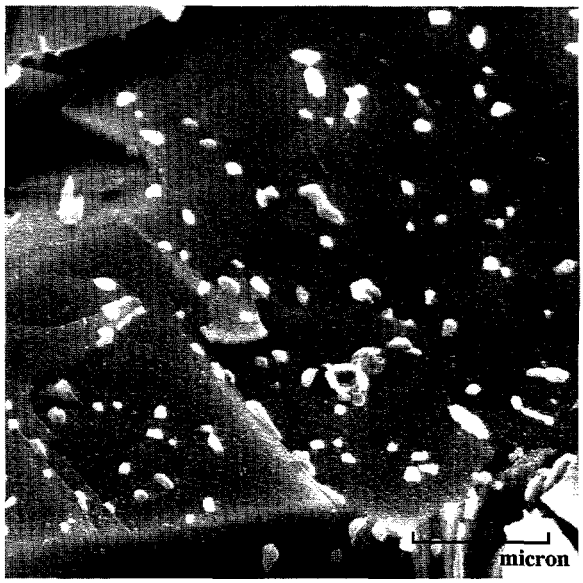

Fig. 1.2. Scanning electron microscope fracture surface image of Bi-2223 containing 6.7 vol % magnesium oxide particles sintered at 845°C for 24 h.

Examination of the Magnesium Oxide Particles

Characteristics of the magnesium oxide particles in doped HTS were examined by both scanning and transmission electron microscopy (TEM). Figure 1.2 shows an SEM fracture surface image of the 6.7 vol % magnesium oxide specimen that had been sintered for 24 h. This figure shows that the magnesium oxide particles are homogeneously distributed, and particle size is typically ~100 nm. Analyses by TEM further confirmed that magnesium oxide particle size ranges from 50 to 200 nm. Moreover, these particles are found to be distributed within the Bi-2223 matrix, do not show any preference to segregate at the grain boundaries, and reflect no chemical interdiffusion between magnesium oxide and the HTS. Also, the size of the particles is relatively independent of the concentration of magnesium in the compound, but particle density is directly related to the amount of dopant. In addition to the fine particle size, interfacial regions between the magnesium oxide particles and the HTS matrix are found to be populated by a high density of dislocations as seen in Fig. 1.3. Therefore, even if the magnesium oxide particles are too large to provide effective point pinning, these line defects should be effective pinning centers that can interact with several flux lines at a time.

Preliminary Results

More important, however, is the question of phase purity of the matrix and the particles. Energy-dispersive spectroscopy (EDS) analysis of the matrix revealed that no magnesium is in the Bi-2223 HTS within the detection limit (Fig. 1.4). Consequently, the transition temperature should not be affected by any magnesium substitution. To confirm this, ac susceptibility measurements were conducted on 1-g sections of the three specimens shown in Fig. 1.1. Figure 1.5 shows that under an ac field of 2 G and 800 Hz, the onset of superconducting transition ranges from 106 to 107 K, and magnesium-doping indeed has negligible effect

on the occurrence of superconductivity in Bi-2223. On the other hand, EDS results show that the magnesium oxide particles do contain a small amount of copper (Fig. 1.6). This indicates that unless the dissolved copper is compensated

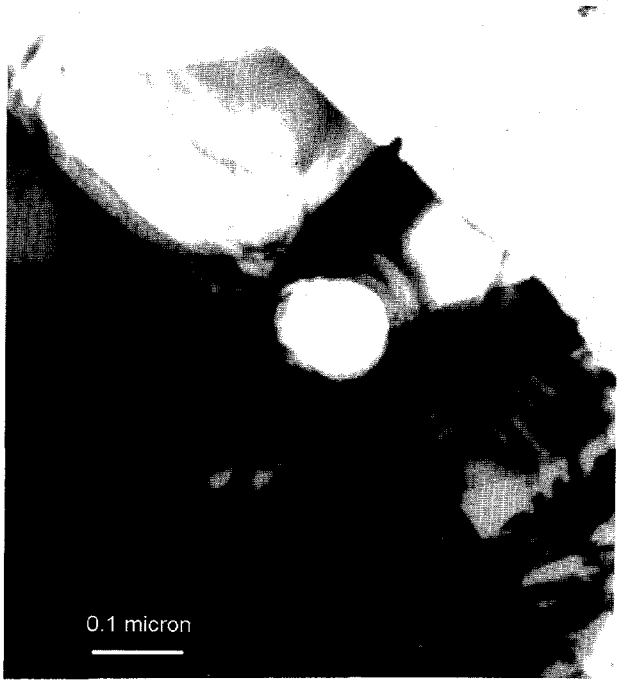

Fig. 1.3. Transmission electron microscope image of a magnesium oxide particle within the grain of sintered Bi-2223 fabricated from magnesium-doped aerosol precursor powder. Note the high density of dislocations in the high-temperature superconductor at the magnesium/Bi-2223 interfacial region.

for, a possibility of degradation exists in the superconducting properties as a result of the tendency to form low-copper content secondary phases rather than the high-T_c Bi-2223 phase. Powders with appropriately adjusted compositions have been prepared, and processing of PIT tapes containing these precursors is under way.

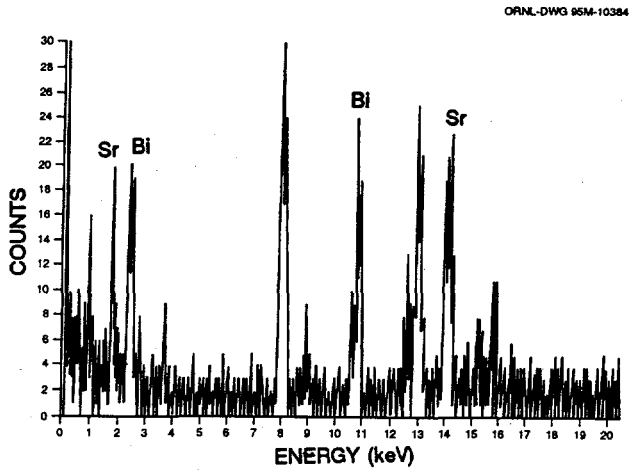

Fig. 1.4. Energy-dispersive spectroscopy pattern of the matrix material in a Bi-2223 sample containing 6.7 vol % magnesium oxide particles and sintered at 845° for 24 h.

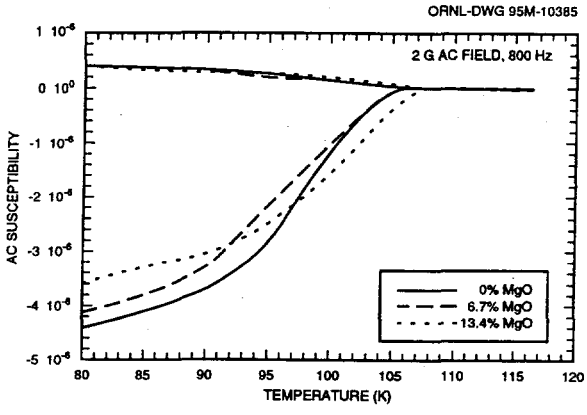

Fig. 1.5. Changes in ac susceptibility of sintered magnesium-doped and undoped Bi-2223 with temperature.

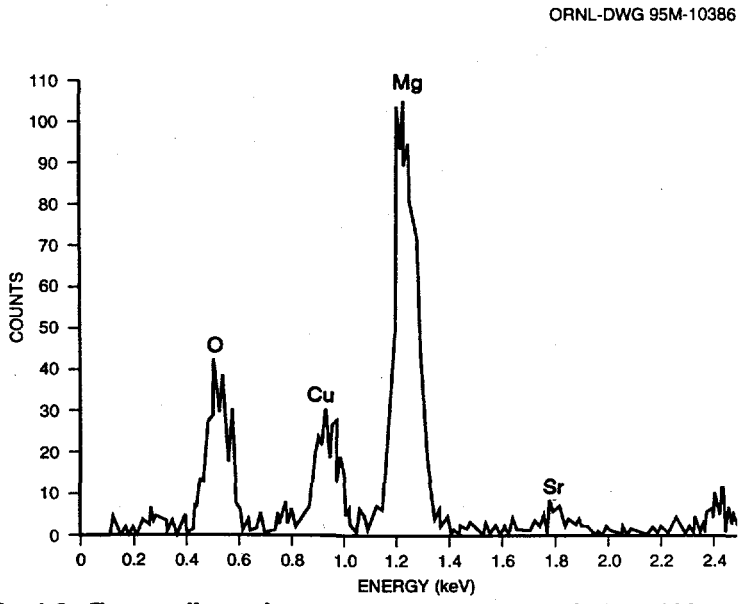

Fig. 1.6. Energy-dispersive spectroscopy pattern of 50- to 200-nm-diam particles in a sintered Bi-2223 fabricated from magnesium-doped aerosol precursor powder.

EFFECT OF FRICTION ON THE DEFORMATION AND CRITICAL CURRENT DENSITY OF $(Bi,Pb)_2Sr_2Ca_2Cu_3O_{10}$ POWDER-IN-TUBE TAPES

To obtain high critical current density (J_c) in PIT $(Bi,Pb)_2Sr_2Ca_2Cu_3O_{10}$ (BSCCO-2223), the tapes have to be subjected to repeated heating and deformation cycles. The deformation steps lead to greater density and better alignment of the BSCCO-2223 grains[5] and are considered to be a vital part of the thermomechanical treatment. In addition to a high density and grain alignment, a smooth interface between the silver sheath and oxide core is necessary for high J_c.[6]

Even though the deformation process is recognized to be extremely important, little information is available on the effect of deformation conditions on the microstructure and properties of these tapes. In this investigation the effects of friction on the deformation and J_c of BSCCO-2223 monofilament and multifilament tapes have been studied.

Monofilament BSCCO-2223 Tapes

In the fabrication of monofilament tapes, precursor powder of $Bi_{1.84}Pb_{0.34}Sr_{1.91}Ca_{2.03}Cu_{3.06}O_x$ overall composition was produced by the aerosol process and was filled into silver tubes. These wires were then drawn and rolled to a thickness of 250 μm. Sections 30 mm long were cut from these tapes and were deformed by both uniaxial pressing and rolling under various lubrication conditions. For uniaxial pressing, individual specimens were placed between two polished steel plates and were deformed under a pressure of 1 GPa. To alter the deformation friction, mineral oil and Teflon tapes were introduced between the silver sheath and the steel plates for some specimens. Deformation by rolling was conducted using a 10-cm-diam (4-in.) rolling mill; a portion of the rollers was coated with soap to provide lubrication. Specimens were rolled to various thicknesses under both unlubricated and lubricated conditions at 6-μm reduction per pass.

The top surfaces of BSCCO-2223 monofilament tapes pressed between steel plates, with mineral oil, and with Teflon tapes are shown in Fig. 1.7(*a*), (*b*) and (*c*) respectively. These figures show that, as the effectiveness of the lubricants improves (i.e., from unlubricated to mineral oil to Teflon tapes), the amount of lateral spreading increases to a point where cracks in the sheath appear [Fig. 1.7(*b*)]. More dramatic is the amount of deformation experienced by the tapes pressed between Teflon where the cracks at the silver sheath propagate through the entire tape thickness [Fig. 1.7(*c*)]. The transverse cross-sectional areas of these three tapes are shown in Fig. 1.8(*a*), (*b*) and (*c*). These figures show that, as lubrication improves, sausaging of the core reminiscent of longitudinal sections in rolled tapes starts to appear. In pressing between Teflon tapes, the deformation is so inhomogeneous that exposed or terminated sections of the core are seen. These results all point to the fact that, as the friction coefficient between the ductile silver sheath and the loading fixture is decreased, the silver at the interface is free to flow (as opposed to an ideal case of zero interface velocity). Consequently, deformation is less homogeneous, and the core deforms nonuniformly as cracks appear at regions of lower density and perpendicular to the elongation direction.

In deformation by rolling, the BSCCO-2223 core thickness of monofilament tapes processed between smooth roller surfaces decreases with rolling, and sausaging starts to be evident when the core thickness is reduced to less than about 25 μm. On the other hand, deformation of the core is noticeably more nonuniform when lubrication is provided by a soap coating. This inhomogeneous deformation can be seen in Fig. 1.9(*a*) to (*c*), which show the longitudinal cross section of tapes deformed to various extents. Figure 1.9(*b*) shows that sausaging occurs at an earlier stage where the core thickness is still in excess of 50 μm. As the tape thickness is further reduced, the degree of sausaging becomes progressively worse. In addition, transverse cracks start to appear in the silver sheath that correspond to the periodic appearance of the core [Fig.1.9(*c*)].

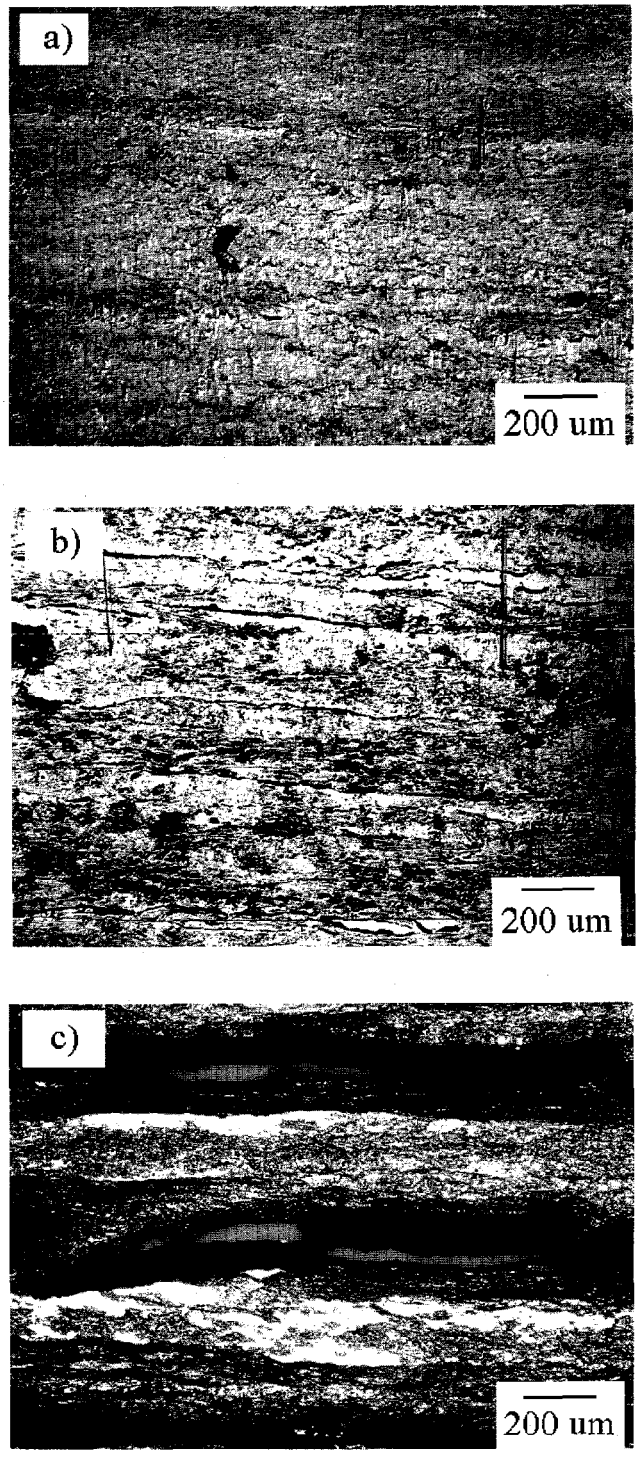

Fig. 1.7. Optical micrographs of the top surfaces of BSCCO-2223 tapes pressed (*a*) between polished steel plates, (*b*) with mineral oil, and (*c*) with Teflon tapes.

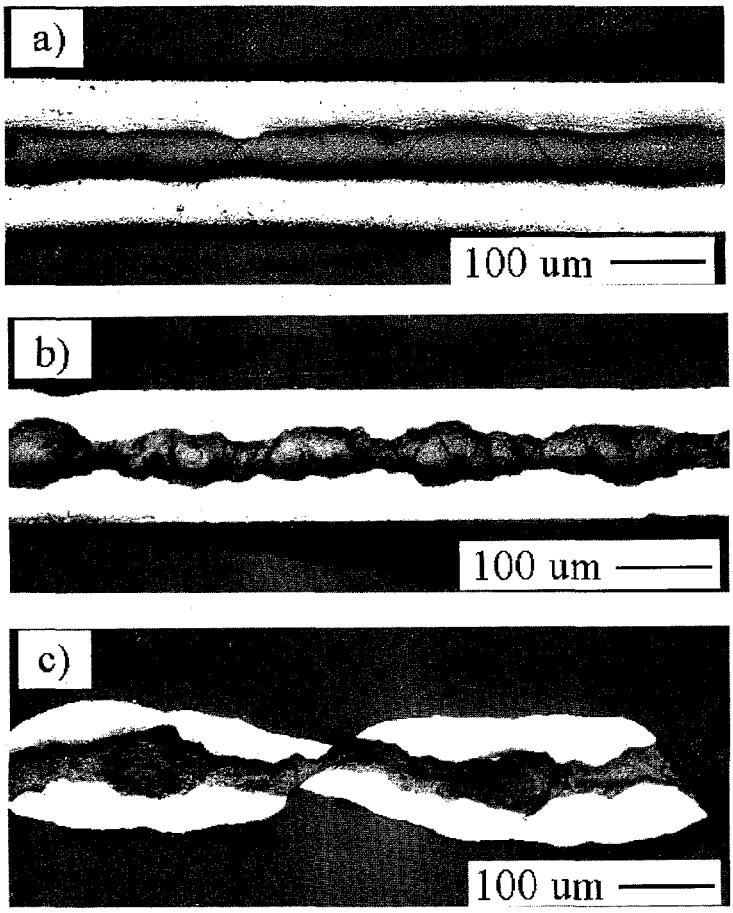

Fig. 1.8. Transverse cross sections of powder-in-tube BSCCO-2223 tapes uniaxially pressed (*a*) between polished steel plates, (*b*) with mineral oil, and (*c*) with Teflon tapes.

From the above results, it appears that an increase in deformation friction can provide an avenue toward a more homogeneous and denser core. This is in contrast to traditional deformation processes where lubrication is employed to reduce the power requirement of the machinery. To examine the validity of this approach, a portion of the rolling mill was roughened using 80-grit grinding paper. Tapes 30 mm (1.2 in.) long and 250 μm in initial thickness were cut from two sets of BSCCO-2223 monofilament tapes containing aerosol powder with 0.32 and 0.42 lead content. Both sets of tapes were then rolled between smooth and roughened surfaces down to 165 μm at 6-μm reduction per pass. These tapes were subsequently subjected to thermo-mechanical treatment at 825°C in 7.5% oxygen for 25 to 50 h. Deformation was carried out by uniaxial pressing between polished steel plates at 2 GPa between heat treatments. Figures 1.10 and 1.11 show the variation in J_c of these tapes with accumulated processing time. These figures show that regardless of the tape composition, the J_c of those tapes that were initially deformed by roughened rolls is consistently higher than those processed by smooth rolling surfaces. These results indicate that increased friction during the initial deformation of monofilament tapes will lead to more homogeneous and denser superconducting cores and is beneficial to the performance of monofilament BSCCO-2223 tapes.

Multifilament BSCCO-2223 Tapes

To determine whether increased friction during initial deformation has the same beneficial effects on multifilament tapes, BSCCO-2223 wires containing 85 aerosol precursor filaments were manufactured by American Superconductor Corporation (ASC). Sections [50 mm (2 in.) long] of these wires were initially deformed from a starting diameter of 1250 μm to a thickness of ~250 μm between smooth and roughened rolls. In addition to the different roller surfaces, deformation was also performed at various values of reduction per pass such that the effect of strain rate could also be examined. The different reduction per pass and thermomechanical treatment schedules are summarized in Table 1.1.

Transverse cross sections of the multifilament tapes at various stages of initial deformation are shown in Figs. 1.12 to 1.14. These figures show that it is possible to examine the degree of core densification qualitatively: gray areas represent dense precursor material, while black areas represent porous cores. These

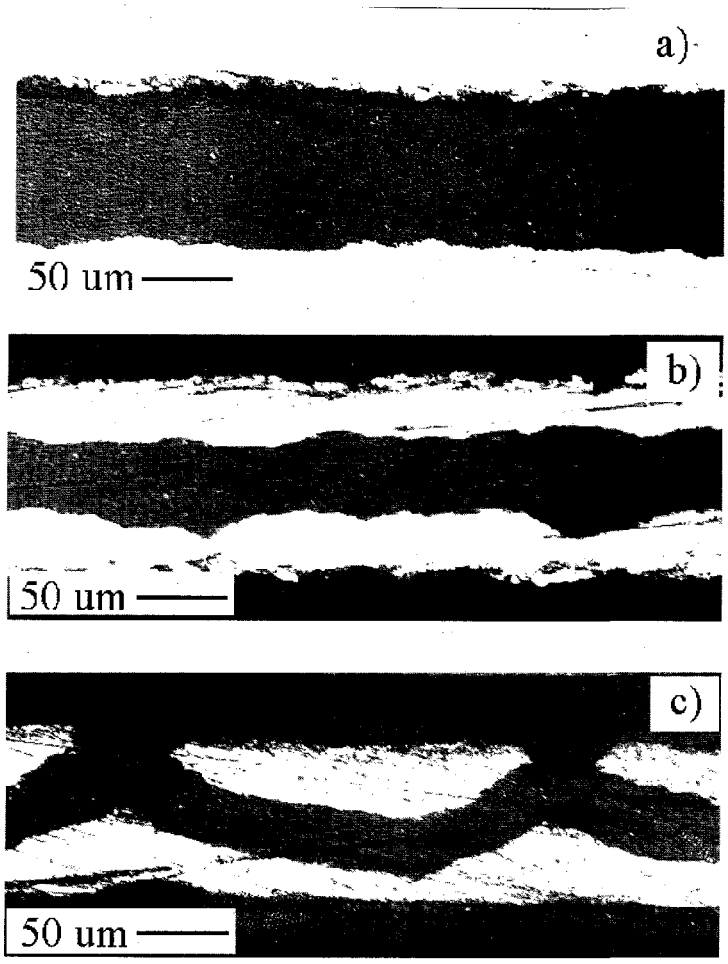

Fig. 1.9. Longitudinal cross sections of powder-in-tube BSCCO-2223 tapes rolled to various thicknesses with soap coating as lubricant.

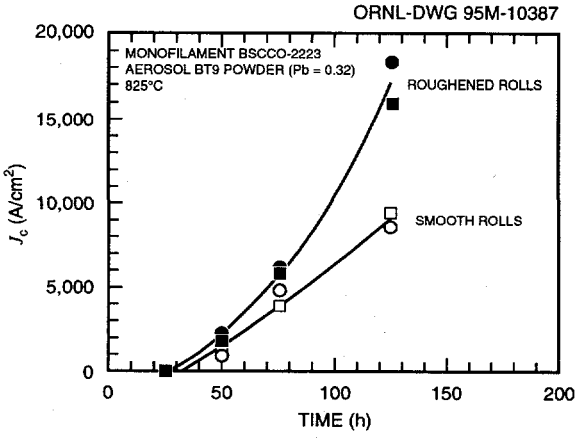

Fig. 1.10. Variation in J_c with heat treatment for power-in-tube tapes (Pb = 0.32) initially rolled between smooth and roughened surfaces.

contrasts clearly reveal that mechanical deformation of these composite tapes is inhomogeneous. In addition, the degree of inhomogeneity increases with friction (i.e, from smooth rolls to roughened rolls) and strain rate (i.e., from small to large reduction per pass). In fact, the deformation pattern of these tapes closely resembles that of the "dead metal zones" or "dead zones" frequently encountered in metal forming. One such deformation pattern of a steel upset specimen deformed at room temperature under condition of high friction[7] is shown in Fig. 1.15. Because of high friction, zones of limited deformation (i.e., dead zones) are generated in the area of the workpiece in contact with the dies. Separating these areas of limited deformation from the deforming bulk are thin regions of much higher than normal deformation known as shear bands.

In the BSCCO-2223 multifilament tapes the same deformation pattern results because of friction between the tape surfaces and the rollers. As frictional force or strain rate is increased, areas of limited deformation (i.e., size of the dead zone) penetrate deeper toward the interior of the tape. Because the amount of total tape reduction is fixed by the roller gap, however, higher strain is then localized within the central portion as well as the

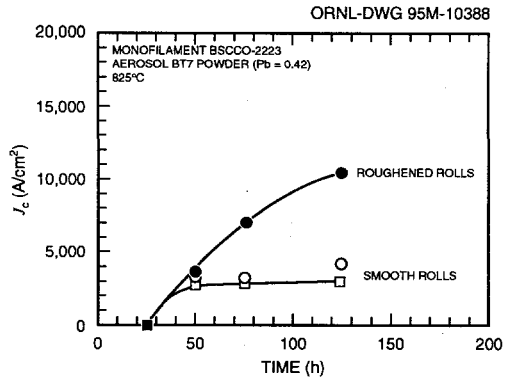

Fig. 1.11. Variation in J_c with heat treatment for powder-in-tube tapes (Pb = 0.42) initially rolled between smooth and roughened surfaces.

Table 1.1. Deformation conditions, thermomechanical treatment schedules, and current capacity of multifilament BSCCO-2223 tapes

Rolls	Reduction per pass	Initial deformation: rolled from (μm)	HT 1[a]	Rolled to (μm)	HT 2	I_c per 250-μm tape thickness (A)
Smooth	6 μm	1250–250	10 h at 825°C	220	10 h at 825°C	6.2
Smooth	20%					7.6
Roughened	6 μm					6.6
Roughened	20%					5.7
Smooth	3 μm	1250–270	5 h at 825°C	240	5 h at 825°C	5.5
Smooth	20%					6.7
Roughened	μm					5.3
Roughened	20%					4.7

[a]HT = heat treatment.

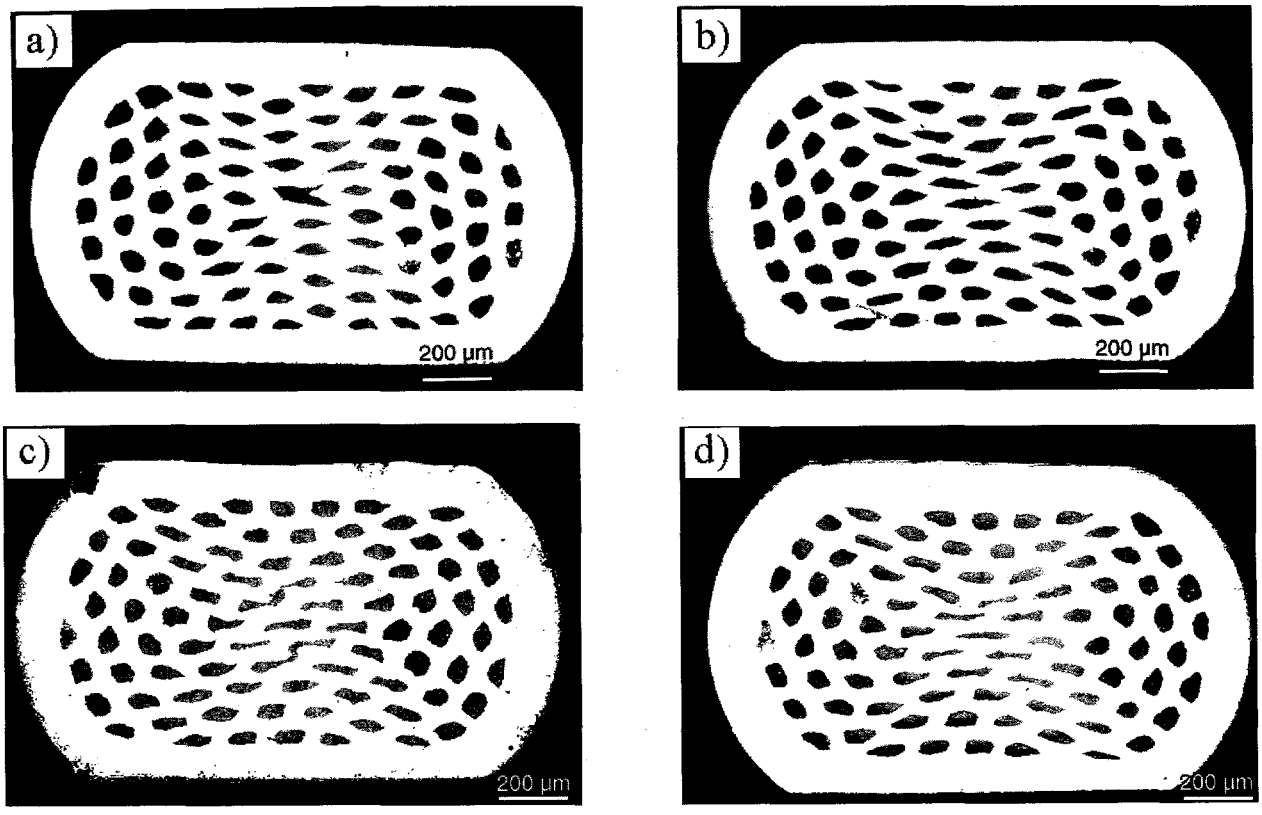

Fig. 1.12. Transverse cross sections of multifilament BSCCO-2223 tapes deformed to roughly 900 μm before first heat treatment under the following conditions: (*a*) smooth rolls, 6-μm reduction per pass; (*b*) smooth rolls, 20% reduction per pass; (*c*) roughened rolls, 6 μm per pass; and (*d*) roughened rolls, 20% reduction per pass.

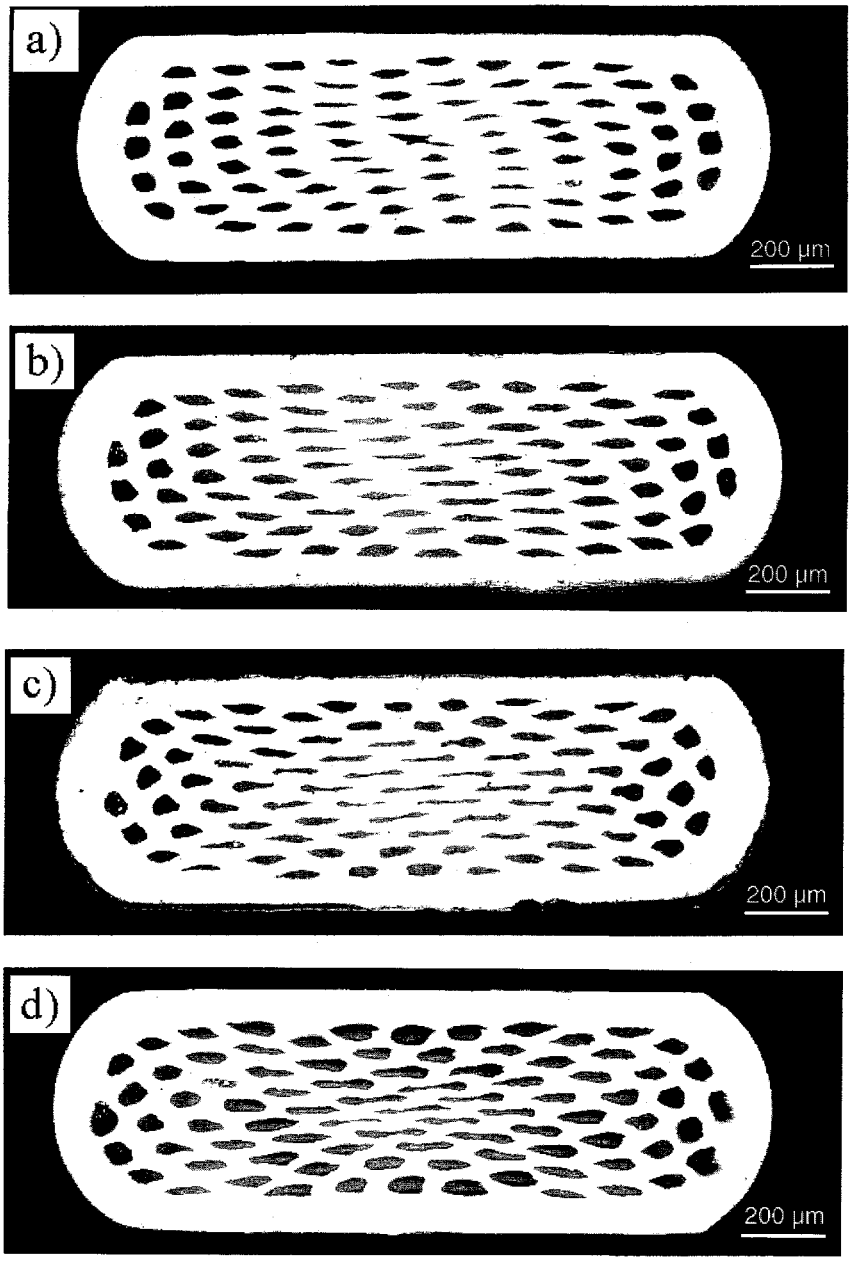

Fig. 1.13. Transverse cross sections of multifilament BSCCO-2223 tapes deformed to roughly 600 μm before first heat treatment under the following conditions: (*a*) smooth rolls, 6-μm reduction per pass; (*b*) smooth rolls, 20% reduction per pass; (*c*) roughened rolls, 6 μm per pass; and (*d*) roughened rolls, 20% reduction per pass.

diagonals of the tapes. This increase in localized strain can be seen in Fig. 1.16(*a*) to (*d*), which show the transverse cross sections of the 250-μm tapes at a higher magnification. These figures clearly demonstrate that, with increased friction or strain rate, the filaments at the central portion of the tapes become highly densified, thinner, and elongate more in the lateral direction. In contrast, the filaments near the tape surfaces remain thick, porous, and are subject to little or no deformation. In addition, the filaments at the edges of the tapes experience only limited deformation because of both the initial geometry of a round wire and flow localization (barreling).

Critical current measurements of these tapes revealed that, unlike monofilament BSCCO-2223, deformation of multifilament PIT under high friction conditions does not necessarily result in the best I_c. In fact, the highest I_c is exhibited by the tape deformed at large reduction per pass with smooth rolls, which shows the most homogeneous deformation characteristics. The different responses of mono- and multifilament tapes to friction can now be explained with the aid of dead zone development, as is shown in Fig. 1.17. In a monofilament tape the precursor core, which is sandwiched between thick silver sheaths, is located within the central region of the tape. Consequently, even though an increase in friction leads to larger dead zones, these zones of limited deformation are still located within the silver sheath. The net effect of increased friction on monofilament tapes is then to increase the amount of strain experienced by the core, leading to denser cores and high I_c.

In multifilament tapes, on the other hand, precursor filaments are distributed throughout the entire cross section. Therefore, an increase in friction (i.e., size of dead zones) means that a larger number of the filaments are located within these zones and will experience only limited deformation. These porous filaments cannot contribute significantly to the current- carrying capability of the tapes. Thus, deformation under high friction in multifilament tapes of present geometry does not lead to enhanced I_c. Yet, even though only a limited number of filaments are expected to transport supercurrent in tapes deformed under high friction and large reduction per pass, their I_c is only slightly lower than that of the tapes with the most homogeneous deformation (i.e., smooth rolls and large reduction per pass). This result indicates the importance of high core density as well as the benefit of thin filament cores, and points toward various strategies that may increase the overall performance of multifilament tapes. One possible modification is the employment of a thicker outer sheath to maintain the dead zones within the sheath under high friction conditions while taking advantage of the higher strain experienced by the central region. Another modification is the reorientation of the filament packing geometry to minimize the number of filaments at the edges of the tapes. An opposite approach may involve the utilization of lubricant to limit the dead zone size, although further alterations of the rolling setup have to be made to minimize the occurrence of sausaging.

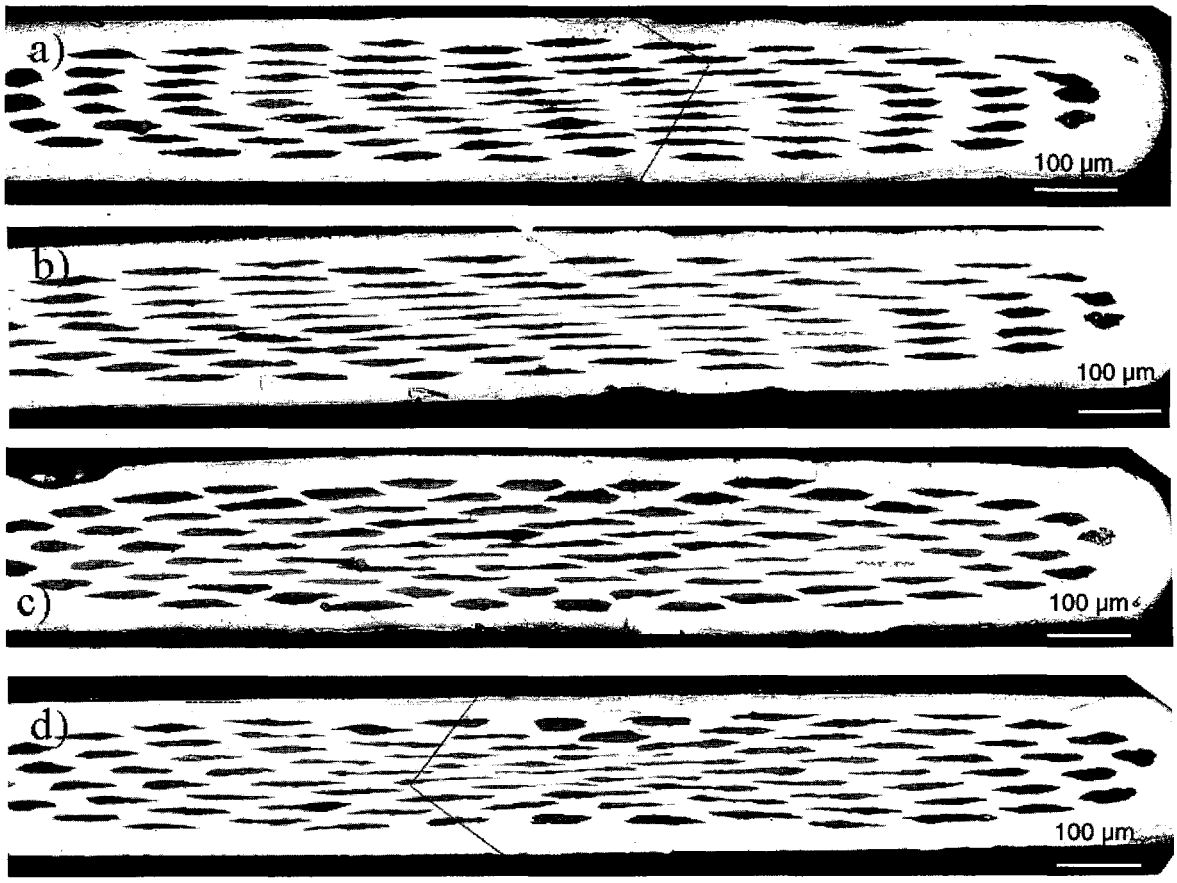

Fig. 1.14. Transverse cross sections of multifilament BSCCO-2223 tapes deformed to roughly 250 μm before first heat treatment under the following conditions: (*a*) smooth rolls, 6-μm reduction per pass; (*b*) smooth rolls, 20% reduction per pass; (*c*) roughened rolls, 6 μm per pass; and (*d*) roughened rolls, 20% reduction per pass.

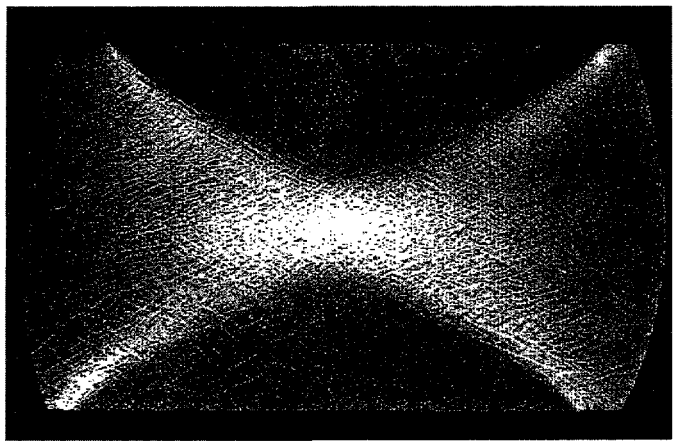

Fig. 1.15. Transverse section of steel upset specimen deformed at room temperature under conditions of high friction. Dark dead metal zones on the top and bottom of the specimens are separated from the deformed bulk by narrow regions of high deformation that etch lighter in the micrograph.

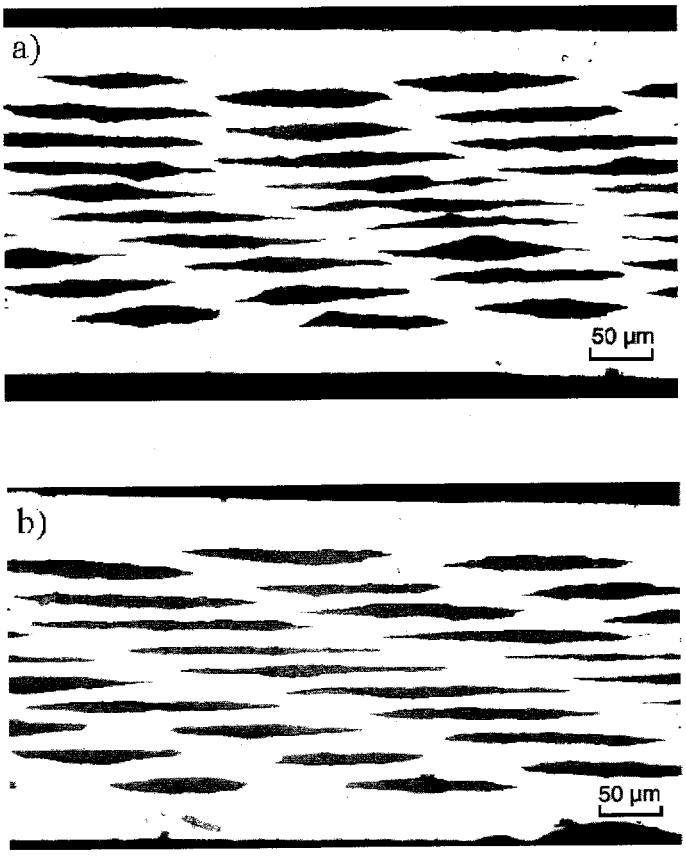

Fig. 1.16. Higher magnification of samples shown in Fig. 1.14. Deformation conditions are also the same.

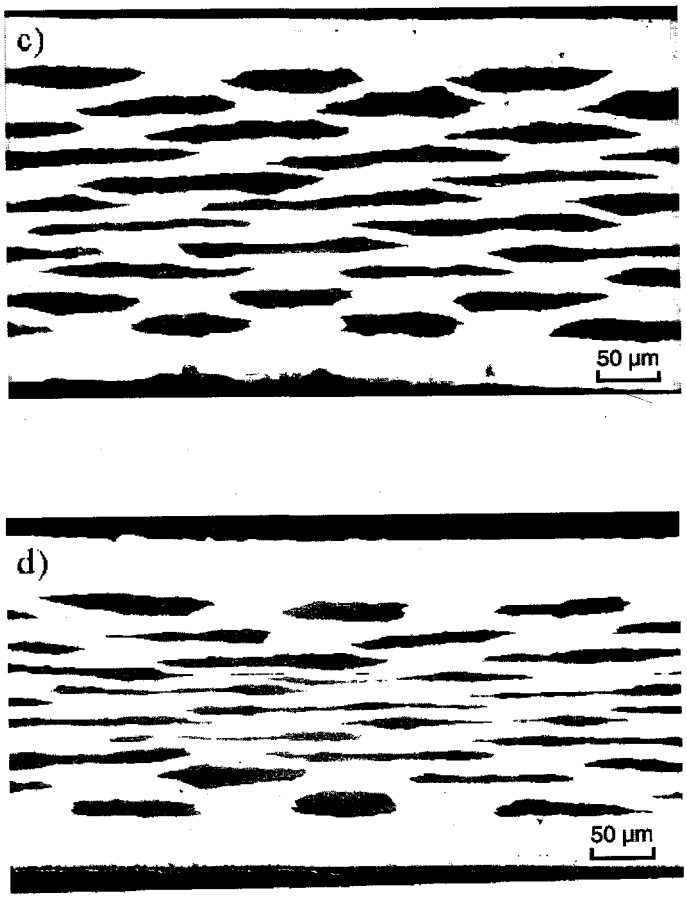

Fig. 1.16 (continued).

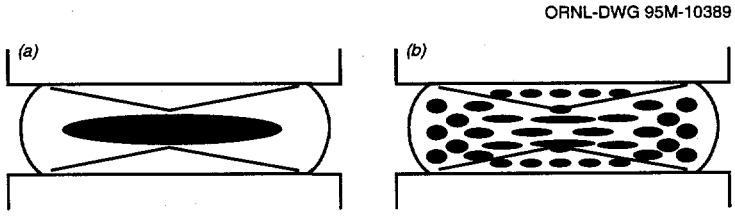

Fig. 1.17. Schematic of dead zones within (*a*) monofilament and (*b*) multifilament tapes deformed under conditions of high friction. The single core in monofilament tape is expected to lie outside the dead zones, while a large number of filaments in the multifilament tape will be located within the dead zones.

FABRICATION OF MAGNESIUM OXIDE WHISKER-REINFORCED BSCCO-2223 TAPES BY POWDER-IN-TUBE AND TUBULAR WIRE PROCESSES

The ability to maintain a high critical current density (J_c) when subjected to a considerable bending strain is essential for the fabrication and operation of $(Bi, Pb)_2Sr_2Ca_2Cu_3O_{10}$ (BSCCO-2223) superconducting tapes. Because of the brittle nature of the superconductor, however, the current capacity of monofilamentary BSCCO-2223 tapes is found to decrease in an irreversible fashion when the wires are subjected to a strain of only a few tenths of a percent.[8] This irreversible reduction in J_c is believed to be the result of transverse crack propagation in the weak superconducting core,[9] leading to a decrease in size of the percolation path. Therefore, to utilize the superconductor in practical conductor applications, the strain tolerance of the BSCCO-2223 tapes has to be improved.

Selection of the Reinforcement Material

We know that the forming of a composite can enhance the mechanical and fracture properties of a ceramic. Unfortunately, the high reactivity of HTS with most materials at elevated processing temperatures results in the degradation or even complete loss of superconductivity. In this ongoing investigation, magnesium oxide, being one of the few materials that are relatively inert with respect to BSCCO-2223, is selected as the reinforcement material. Besides its low reactivity with BSCCO-2223, magnesium oxide has several additional advantages over other potential reinforcement materials. First, the coefficient of thermal expansion of magnesium oxide (12–13.5 $\times$ 10^{-6}/°C) is compatible with that of BSCCO-2223 (11.7–16 $\times$ 10^{-6}/°C) and is expected to minimize any undesirable microscopic residual thermal stresses that can cause microcracks. Second, magnesium oxide can be obtained in whisker form that, when aligned along the tape axis, can bridge and arrest propagating transverse cracks that are responsible for the irreversible decrease in J_c. Also, significant improvements in mechanical and fracture properties of the superconducting core are expected because of the high modulus (250 GPa) and high strength (>10 GPa) of the magnesium oxide whiskers.

The magnesium oxide whiskers used in this investigation were prepared by slow hydrolysis of a mixture of molten salts composed of $MgCl_2$ and KCl. The reaction was performed in an all-Al_2O_3 apparatus consisting of container, thermocouple well, and sparge line. Typical reaction conditions were 35 mol % $MgCl_2$, reaction temperature of 900°C, and carrier gas flow rate of 150 cm^3. After reaction had been completed, the whiskers were extracted with hot water, which also removed the KCl and any unreacted $MgCl_2$. Utilization of this improved reaction technique resulted in a whisker yield of better than 85%. The typical whiskers are found to be 1 to 10 μm in diameter and up to 3-mm (0.12 in.) long.

Using a commercial (SSC) precursor powder of overall composition $Bi_{1.8}Pb_{0.34}Sr_{1.91}Ca_{2.03}Cu_{3.06}O_x$, BSCCO-2223 tapes with 0 and 15 vol % magnesium oxide whisker addition were fabricated by the standard PIT technique. XRD revealed that the phase assemblage of the powder was comprised of BSCCO-2212, Ca_2PbO_4, CaO, and CuO. The magnesium oxide whiskers were mixed homogeneously with the precursor powder and packed in silver tubes. The tubes were then drawn through a series of dies and rolled to 0.25-mm-thick tapes. The tapes were first heat-treated in vacuum at 700°C for 12 h to reduce the carbon content; they were then subjected to a series of thermomechanical treatment with sintering temperatures of 816–825°C, sintering duration of 50 h, and pressing pressure of 1–3 GPa.

Microstructural Observations

Microstructural observations of the reinforced tapes revealed that the magnesium oxide whiskers provided a template for aligned growth of the 2223 phase at the whisker-superconductor interface even in the early stages of processing. The 2223 phase tends to align

along the length of the tape parallel to the orientation of the magnesium oxide whisker. This phenomenon of aligned formation of 2223 phase adjacent to the whiskers can be used to enhance the formation and texturing of the 2223 phase in the core if the magnesium oxide whiskers can be aligned along the tape axis. Unfortunately, this preferred whisker alignment has not been obtained in BSCCO-2223 tapes fabricated by the standard PIT technique. This lack of preferred whisker alignment is believed to be due to the manner by which precursor powder is packed into the silver tube. As is shown in Fig. 1.18, uniaxial compaction of precursor powder will result in a certain degree of whisker alignment perpendicular to the loading direction (side view), while within the alignment plane (top view) the whisker orientation is completely random. Because of this unfavorable whisker orientation within the compact, final whisker alignment is marginal at best after extrusion, drawing, and rolling of the tapes.

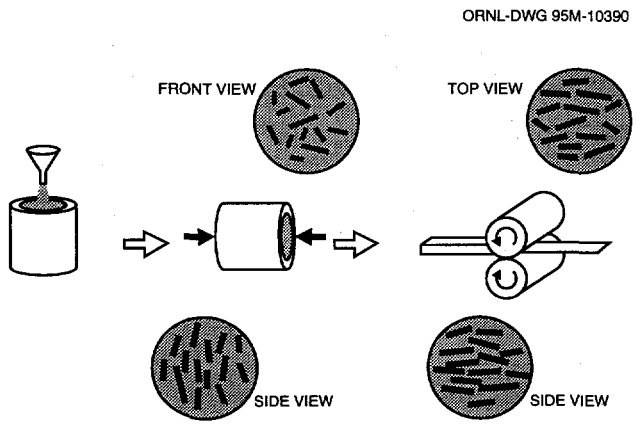

Fig. 1.18. Schematic of magnesium oxide whisker alignment in BSCCO-2223 tapes fabricated by the standard powder-in-tube process.

Because the magnesium oxide whiskers are misaligned with respect to the tape axis, full advantage of the BSCCO-2223 texturing at the whisker-superconductor interface cannot be obtained. Instead, the misaligned whiskers will tend to reduce the effective cross-sectional area of the superconducting core and will lead to a decrease in J_c. This reduction in J_c is indeed found in the reinforced tapes when compared with their unreinforced counterpart (Fig. 1.19). The figure shows that after 200 h of thermomechanical treatment, the J_c of 15 vol % magnesium oxide whisker-reinforced PIT tape is almost 30% less than the unreinforced value. This decrease cannot be accounted for by the reduction in superconducting volume alone.

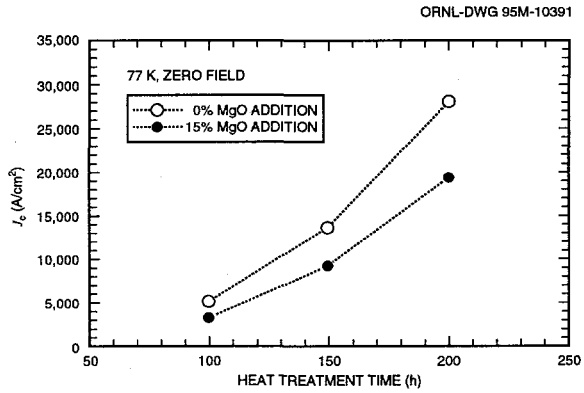

Fig. 1.19. Critical current density development of BSCCO-2223 tapes at various stages of the thermomechanical process.

Even though the alignment of magnesium oxide whiskers is not ideal, strain tolerance studies performed on the PIT tapes (Fig. 1.20) show that the onset of irreversible drop in J_c is extended to a higher strain level in the reinforced tapes. A more impressive tolerance to strain in the reinforced tapes is observed in the "bend only" tests. As the figure shows, the reinforced tapes sustain 90% of their initial J_c up to a strain of 0.6%. Microstructural analyses of the test tapes revealed evidence of the magnesium oxide whiskers having provided resistance to transverse crack propagation by means of crack bridging and crack deflection. As a result, the driving force for the crack becomes less than the resistive force, resulting in crack arrest. These results indicate that if the whiskers can be oriented along the tape axis, additional enhancement in both the J_c by interface-induced texture and strain tolerance by more favorable whisker bridging should occur.

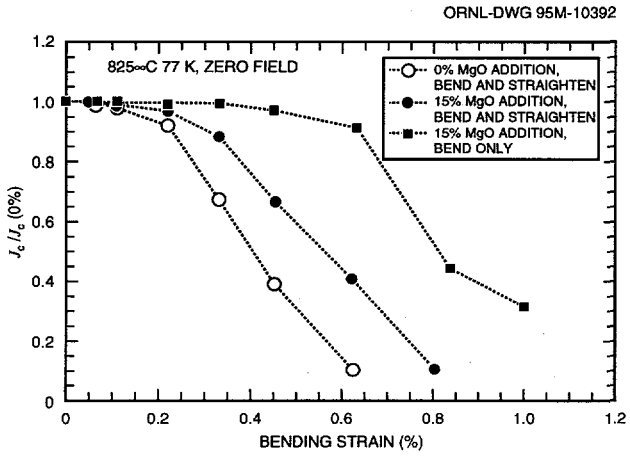

Fig. 1.20. Comparison of the influence of bend strain on the J_c of BSCCO tapes after heat treatment at 825°C for 150 h.

The Tubular Wire Process

The study in magnesium oxide whisker-reinforced BSCCO-2223 tapes is currently being extended to tapes fabricated by Plastronic, Inc., using the tubular wire process, which has the advantages of near net shape manufacturing and a lower silver-to-superconductor ratio. More importantly, the manner by which precursor powder is loaded into the tubular wire offers the possibility of preferential alignment in the magnesium oxide whiskers. As is seen in Fig. 1.21, the precursor powder in the tubular wire process is deposited on a long silver foil formed in the shape of a trough. By incorporating the powder in this manner, the whiskers should tend to settle in an orientation parallel to the wire axis (top and side views). After powder deposition, the silver foil is then folded into a tubular shape, and the seam is carefully welded. The tubular wire is then drawn to the required diameter and rolled into tapes of 0.25-mm thickness. These mechanical working steps should further align the magnesium oxide whiskers, resulting in tapes of enhanced superconducting and mechanical characteristics.

BSCCO-2223 tapes with 0, 5, and 15 vol % magnesium oxide whisker reinforcement have been fabricated by the tubular wire process. Microstructural studies are currently under way to determine the whisker alignment and distribution within the precursor core. The appropriate thermomechanical treatment procedures will be developed to optimize the current density of the tubular wire process tapes. Strain tolerance of these reinforced tapes will be determined, and the results will be reported at a future date.

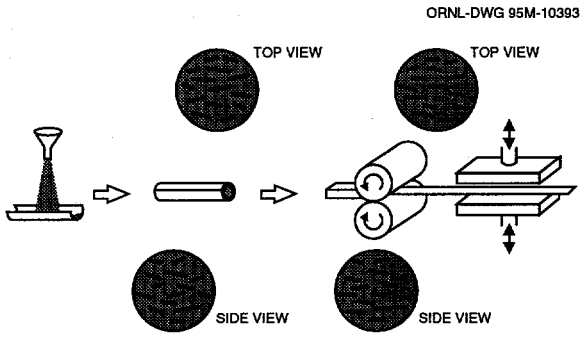

Fig. 1.21. Schematic of the tubular wire process and the anticipated magnesium oxide whisker alignment in BSCCO-2223 tapes fabricated by this process.

UNIVERSALITY IN BEHAVIOR OF THE DISSIPATIVE REGIMES OF YBCO CONDUCTORS

To confirm and to extend the "robust" behavior previously observed in the dissipative regime, dissipative regimes of different YBCO conductors were explored at current densities well above their critical values. In earlier work we had shown that many practical materials currently available have usefully low resistivities, even at current density (J) values significantly above J_c. Variations in J_c between different samples of a given material (e.g., YBCO) made by similar methods may be caused by the presence of grain boundaries in the direct path of the current. At currents less than the bulk J_c, the superconducting domains are without loss, and the dissipation occurs mainly within the grain boundaries. However, in the dissipative regime

well above J_c, the superconductor itself is resistive for intrinisic reasons. Thus, as J is raised significantly above J_c, the influence of the grain boundaries on the overall resistivity diminishes, making the dissipative regime less sensitive to details of the sample's microstructure. This point is illustrated in Fig. 1.22. Samples *A*, *B*, and *C* have, respectively, no grain boundaries, a low-angle strongly coupled grain boundary, and a large-angle weakly coupled grain boundary. The ordinate is the resistivity of each sample at 77 K normalized to that of silver at this temperature. The abscissa is the absolute current density. As expected, the J_c values are markedly different (23 kA/cm^2, 10 kA/cm^2, and 53 A/cm^2). However, as J is increased, the curves approach a nearly universal behavior ~60,000 A/cm^2. Thus, if one were to operate at a relative resistivity of 3%, as is illustrated in Fig 1.22, the operational J (75 kA/cm^2) would not only be much higher than any of the J_c's (defined at the 1-μV/cm criterion) but would also be relatively independent of sample microstructure details. This fact greatly increases the reliability and reproducibility of the production process, since fewer samples would fail when judged for application in the dissipative regime.

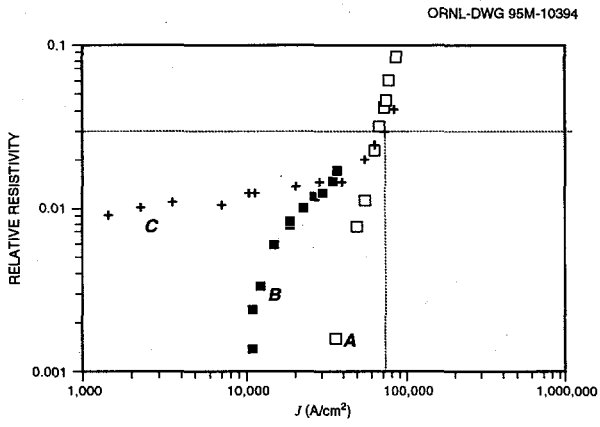

Fig. 1.22. The relative resistivity of ρ(YBCO)/ρ (silver) as a function of current density of 77 K. Melt-processed samples *A*, *B*, and *C* have different grain boundaries. Their resistivities seem to merge to a common dependence for $J > 60$ kA/cm^2. The dashed lines illustrate operation in the dissipative state at a resistivity level ~3% that of silver.

GRAIN BOUNDARY MISORIENTATIONS AND PERCOLATIVE CURRENT PATHS IN HIGH-J_c POWDER-IN-TUBE Bi-2223

Great progress has been made in the processing and fabrication of high-J_c PIT tapes consisting of polycrystalline $Bi_2Sr_2CaCu_2O_8$ (Bi-2212) and $Bi_2Sr_2Ca_2Cu_3O_{10}$ (Bi-2223) sheathed in silver. This is in sharp contrast to the lack of success in fabricating strongly linked conductors using polycrystalline $YBa_2Cu_3O_x$ (Y123). We assume that long-range current flow in polycrystalline materials is dictated by grain boundary characteristics. The effects of grain boundary characteristics on current transmission across the boundary have been studied extensively for Y123. For clean, stoichiometric boundaries, J_c(gb), the grain boundary critical current, appears to be determined primarily by the grain boundary misorientation. The dependence of J_c(gb) on misorientation angle has been determined in Y123 for grain boundary types that can be formed in epitaxial films on bicrystal substrates.[10] These include [001] tilt, [100] tilt, and [100] twist boundaries. In each case high-angle boundaries were found to be weak-linked. The low J_c observed in randomly oriented polycrystalline Y123 can be understood on the basis that the population of low-angle boundaries is small and that frequent high-angle boundaries impede long-range current flow. Recently, the Dimos experiment[10] has been extended to artificially fabricated [001] tilt bicrystals in $Tl_2Ba_2CaCu_2O_8$, $Tl_2Ba_2Ca_2Cu_3O_x$, $TlBa_2Ca_2Cu_3O_x$, and $Nd_{1.85}Ce_{0.15}CuO_4$. In each case it was found that, as in Y123, J_c depends strongly on grain boundary misorientation angle. Although no measurements have been made on Bi-2223, data on current transmission across artificially fabricated grain boundaries in Bi-2212 indicate that most large-angle [001] tilt and twist boundaries are weak links except some coincident site lattice–related (CSL) boundaries. The variation in J_c with grain boundary misorientation in Bi-2212 and Bi-2223 is likely similar to that observed in the well-characterized cases of Y123 and thallium-based superconductors. This then leaves unanswered

the question of how current flows in Bi-2223 and Bi-2212 polycrystalline PIT tapes where no macroscopic in-plane texture is observed.

Path for Strongly Linked Conduction

The "Brick Wall" Model

Various ideas and models for the path for strongly linked conduction, including the possibility that grain boundaries in BSCCO are fundamentally different from boundaries in other high-T_c materials, have been proposed. The most extensively discussed explanation for strongly linked current in BSCCO has been the brick wall model in which large-area [001] twist boundaries are seen as paths for current to flow around large-angle, weak-linked [001] tilt boundaries (assuming that tilt boundaries in BSCCO are similar to those in Y123). However, measurements of the temperature dependence and anisotropy of J_c suggest that long-range current flow involves little or no *c*-axis conduction; thus, doubt is cast on the brick wall mechanism.

The "Railway Switch" Model

As an alternative to the brick wall model, another theory is that the numerous boundaries connecting grains (i.e., those that appear in polished cross sections to have only modest *c*-axis misalignment) are strongly linked in (Bi, Pb)$_2$ $Sr_2Ca_2Cu_3O_x$ PIT conductors.[11] Current is envisioned to flow in "tracks" formed by a series of many such boundaries. The texture of these PIT conductors was found to be much less perfect than that of the idealized brick wall microstructure.[11] In the absence of *c*-axis conduction, misaligned grains seem to provide a mechanism for making current flow three-dimensional.[11,12] In this railway switch model the assumptions of the brick wall model are reversed. In the absence of *c*-axis conduction, *c*-axis twist boundaries cannot be utilized; so boundaries with planes running approximately transverse to the current direction are assumed to be strongly linked. These boundaries were characterized as "small-angle" if their *apparent* *c*-axis misalignment was small (i.e., <15°). However, note that examinations of polished cross sections cannot provide unique information about either *c*-axis or basal plane misalignments. An apparent assumption of this model is that current transmission at grain boundaries in (Bi, Pb)-2223 is determined solely by *c*-axis misorientation, irrespective of relative basal plane orientation. This is in conflict with bicrystal experiments on [001] tilt boundaries in a number of high-T_c materials, as is discussed above.

Although it is well recognized that grain boundary characteristics in all polycrystalline materials determine the bulk critical current density, the microstructure of Bi-2223 PIT tapes has not been adequately studied up to now. Here we report results on a detailed study of the microstructure of Bi-2223 PIT tapes (i.e., the distribution of grain boundary misorientations, their spatial correlations, and the population of low-sigma CSL boundaries). We show that the population of small-angle boundaries in these materials is very high and that percolative current paths can be traced through these low- energy boundaries, providing an explanation for the strongly linked current flow in these materials.

Microstructural Analysis

Using standard oxide PIT techniques, ASC prepared multifilamentary Bi(Pb)-2223 conductors for microstructural analysis. Oxide powders with an initial metals ratio of 1.7:0.4:1.9:2.1:3.1 (Bi:Pb:Sr:Ca:Cu) were used. These powders were packed into silver billets; using extrusion, swaging, and drawing techniques, these billets were subsequently deformed to hexagonal rods. Nineteen of these hexagonal rods were bundled together and inserted into a silver tube. The resulting composite bundle was drawn and then rolled to a tape. An iterative thermomechanical process was used to optimize the superconducting properties of the tape. Heat treatments were performed between 800 and 830°C in 0.0075 atm O_2, the thermodynamic stability field of the Bi-2223

phase. Rolling was used to densify the tape between heat treatments. Fully processed tapes are near 100% dense and have a transport critical current density of 20,000 A/cm^2 at 77 K in self-field using a 1-μV/cm criterion. Individual filaments in the tape are ~20 μm thick and 200 μm wide. To facilitate microstructural analysis, silver was chemically etched from one side to reveal the superconductor. The etching procedure does not interact with the superconductor. Figure 1.23 shows an SEM image of a filament surface. Typical grain size is ~20 μm.

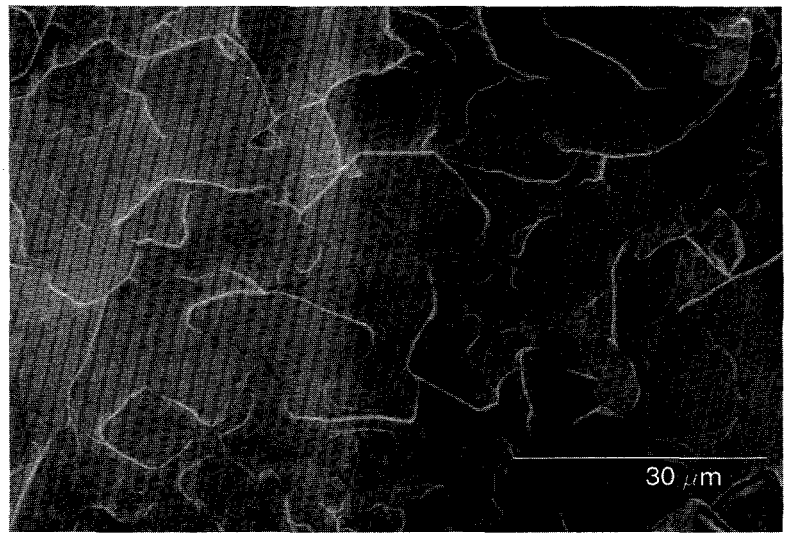

Fig. 1.23. Scanning electron microscope image of the Bi-2223 surface of a filament revealed by etching away the silver from a multifilamentary powder-in-tube specimen. Grain boundaries are clearly visible, permitting determinations by electron backscatter diffraction patterns of the orientations of contiguous grains.

XRD studies were performed to determine the degree of *c*-axis texture and to reveal the presence of any local or macroscopic texture. X-ray rocking curves of the (0010) reflection indicated a full width half maximum (FWHM) of ~20°. Pole figures (1 1 19) indicated a random in-plane texture. X-ray ϕ scans, performed with incident beams of varying sizes, were used to rule out the presence of local in-plane texture, as was observed by this technique in *c*-axis-aligned, $TlBa_2Ca_2Cu_3O_x$, spray-pyrolyzed thick films. Measurements performed with effective illuminated areas of ~0.5 and 0.01 mm^2 indicated random in-plane orientation of the 2223 grains. Grain dimensions in the plane of the sample were ~15–25 μm; thus, local in-plane texture involving as few as 30–50 grains would have been detected with the 0.01-mm^2 beam.

Determination of Grain Orientations

To study the texture more locally and to measure individual grain boundary misorientations, electron backscatter diffraction was performed. Using facilities at TexSEM Laboratories in Salt Lake City, Utah, the orientations of hundreds of contiguous grains were determined. A Cambridge 800 SEM fitted with a silicon-intensified, low-light television camera was used to detect electron backscatter diffraction patterns (EBSPs) from a 50-mm-diam (1-in.) phosphor screen placed inside the microscope. The distance between the sample and the phosphor screen was 40 mm (1.6 in.). The angle between the incident electron beam and the sample surface was 19.4°. The sample was tilted in the SEM to maximize the yield of backscattered electrons. Typical accelerating voltages of 10–15 kV and beam currents of ~5 nA were used. Figure 1.24 shows a typical EBSP from a Bi-2223 grain in the sample. Electrons inelastically scattered from the sample surface are Bragg-diffracted as they exit the specimen, forming a wide-angle backscattered Kikuchi pattern on the phosphor screen. An EBSP is essentially a line diffraction pattern in which each band is a gnomonic-projected lattice plane from the diffracting crystal.

Using a silicon-intensified, low-light television camera, the diffraction pattern was captured. The digitized image from the camera was sent to the frame grabber installed in the Silicon Graphics workstation used to record and to display the diffraction pattern. Image processing in the form of background subtraction was done to improve the quality of the pattern. Indexing of the diffraction patterns was based on

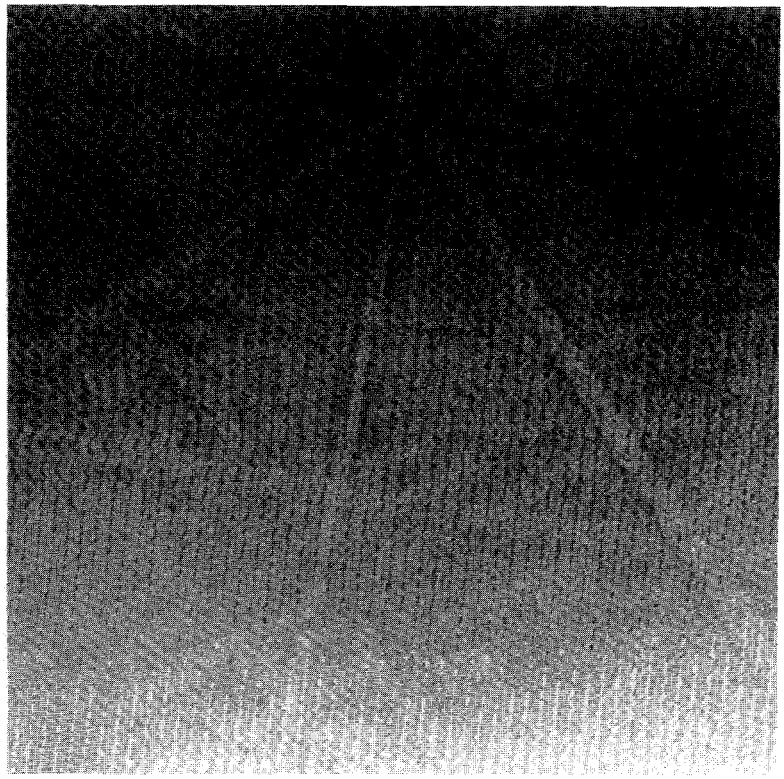

Fig. 1.24. Typical electron backscatter diffraction pattern from a silver-removed, Bi-2223 powder-in-tube sample.

comparison with theoretical values calculated for the crystal structure. Using the "known orientation" silicon crystal method, the pattern center was determined prior to the measurements. Because of nonideal sample surface conditions (typically the samples are quite rough), in most cases indexing was performed by manually identifying the location of the bands in the diffraction pattern. In some cases semiautomatic indexing using the Burns algorithm and the Hough transform was possible. Once the diffraction pattern was indexed, the crystallographic orientation could be expressed as a 3×3 orientation matrix or as three independent Euler angles. This rotation matrix, [R], is essentially the matrix of direction cosines that maps the specimen coordinate system onto the crystal coordinate system. Once the orientation matrix was established, a complete simulated EBSP was worked and superimposed on the experimental EBSP as a check of the indexing.

Small-Angle and Coincident Site Lattice Boundaries

In Fig. 1.23, most grain boundaries are clearly visible, permitting the determination of EBSPs from individual, adjacent grains. Diffraction patterns were obtained for all of the grains that could be distinguished in several small areas containing from 15 to ~100 contiguous grains. The dominant pole in the diffraction pattern shown in Fig. 1.24 exhibits four-fold symmetry and was indexed as the [001] pole of the approximately tetragonal Bi-2223 subcell. From the absolute orientations of grains, grain boundary misorientations were calculated in the form of axis/angle pairs. If the orientation matrices for two contiguous grains are A1 and A2, a matrix that defines the misorientation between them is given by $M12 = A1^{-1}A2$. The geometrical characteristics of the boundary [i.e., the angle and axis of misorientation (the so-called disorientation)] is extracted from the misorientation matrix. Depending on the crystal symmetry, the angle/axis for a given misorientation has many symmetrically equivalent forms (e.g., 24 for cubic, 8 for tetragonal, etc.), and the variant containing the smallest positive misorientation angle was chosen as the description of the disorientation. Figure 1.25 shows the proportion of small-angle and CSL boundaries found in an area containing 227 identifiable boundaries. More than 40% of the boundaries are Σ-1 boundaries (i.e., they have misorientation angles $<15°$), and 30% of the boundaries have misorientations $<10°$. Small-angle boundaries have low energies and can be expected to be less detrimental to J_c than high-angle boundaries. In addition, 8% of the boundaries were found to be

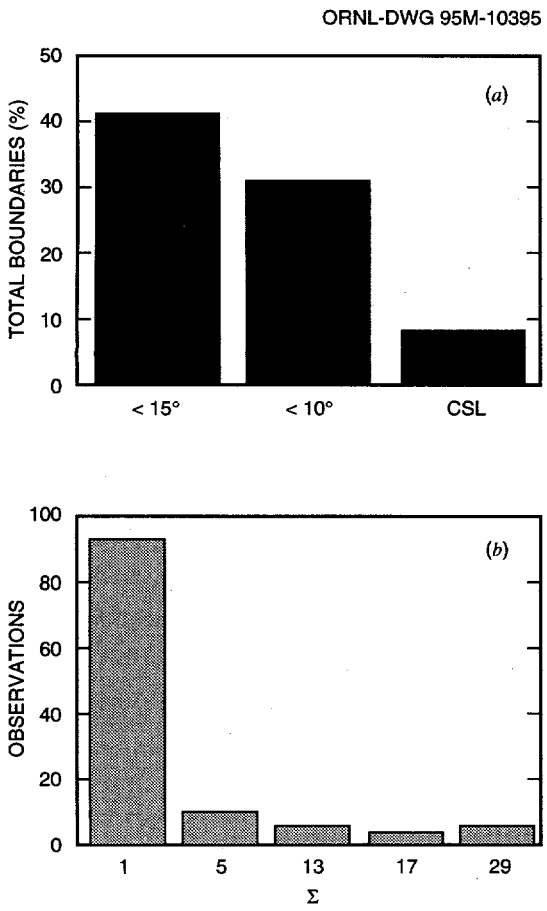

Fig. 1.25. (*a*) Statistics for small-angle and coincident site lattice (CSL) boundaries (total = 227) for a Bi(Pb)-2223 conductor and (*b*) frequency of CSL boundaries (total = 227) with rotation axis [001].

within the Brandon criterion for CSLs >1 and <50 and with rotation axis [001]. The boundaries were classified as low- Σ if the composite axis/angle deviation from the exact Σ orientation was within the Brandon criterion. The deviations were calculated using a previously published method.[13] However, the properties, and therefore the importance, of CSL boundaries have not been determined, although there are indications that some CSL boundaries may be better than other large-angle boundaries. The data in Fig. 1.25(*a*) suggests that their numbers may be only slightly enhanced. Figure 1.25(*b*) shows the frequency of CSL boundaries with the Σ to be <50. The high fraction of Σ-1 boundaries is evident.

Spatial Distribution of Grain Boundaries

The large fraction of low-angle grain boundaries suggests that percolative paths for strongly linked flow may exist. Examination of maps of misorientation angles over small areas indicates that two-dimensional percolative paths among grains at the silver-superconductor interface can indeed be found. Figure 1.26 shows the spatial distribution of grain boundaries in a region of the BSCCO tape. Small-angle boundaries are marked by dashed lines, solid lines designate large-angle boundaries, and dot-dash lines indicate those boundaries that are within the Brandon criterion for a CSL. Many small-angle boundaries are present in this region. Percolative paths consisting of low-angle boundaries can easily be traced through the microstructure from the bottom left to the top right in Fig. 1.26. Because the *c*-axes are not perfectly aligned, most boundaries have a mixed character (i.e., both tilt and twist components). Mixed boundaries that have a significant *c*-axis misalignment component and still have a small, absolute misorientation angle (in other words have small basal plane misorientations) provide opportunities for the current to percolate in the thickness direction of the tape, ensuring three-dimensional current flow. An example of such a boundary is at the top left corner of Fig. 1.26.

In addition, note that the samples contain many "bent" grains. By moving the electron probe within grains that morphologically appear "bent" in the SEM image, in many such grains the (001) pole in the EBSP pattern changes continuously and not abruptly. This indicates that the bent grains contain a series of boundaries that accommodate the change in orientation without the presence of any large-angle boundary. It is surprising to find that such low-angle boundaries are not replaced by a high-angle boundary after the final extended high-temperature anneal that is given to the sample (i.e., the typical polygonization process boundaries observed in metals does not occur). Also, recent nanoindentation studies of Bi-2212 and Bi-2223 PIT samples reveal that these materials possess a unique deformation behavior.

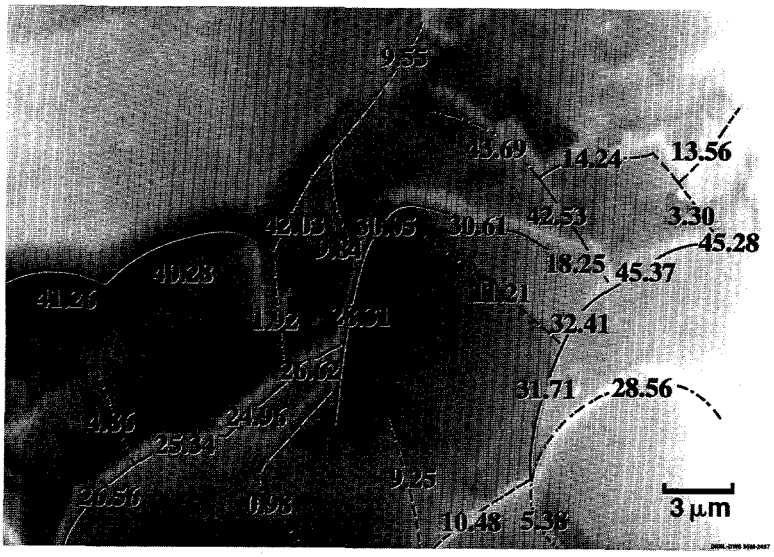

Fig. 1.26. Spatial distribution of grain boundaries in a region of the Bi-2223 tape. Misorientations are indicated at the grain boundaries: dashed lines denote small-angle boundaries (<15°), solid lines depict large-angle boundaries, and dot-dash lines designate those boundaries that are within the Brandon criteria for a coincident site lattice. Percolative paths consisting primarily of low-angle boundaries can be traced from the bottom left to the top right.

This is dominated by extensive cleavage on (001) planes at small applied loads. Once cleaved into thin sheets, individual sheets are highly flexible, and their deformation characteristics are similar to those observed for mica. The typical deformation processing schedule that is normally used to fabricate these tapes can be expected to result in numerous bent grains. Such bent grains can easily be found in metallographic examination of transverse cross sections of these tapes. If many such bent grains accommodate the change in orientation comprising the bend by a series of small-angle boundaries as observed here, then they provide an important mechanism for current flow between *c*-axis misaligned grains and further ensure three-dimensional current flow in the tapes.

Most grains examined here may actually contain a stack of subgrains. Such a structure is commonly observed in TEM examinations of Bi-2223 tapes and is referred to as a "colony" of subgrains. Because EBSPs are formed only by a thin layer (10–50 nm) on the surface, these subgrains do not contribute to the EBSP. TEM examinations have indicated that in most cases the subgrains are connected by [001] twist boundaries. Misorientation angle distributions of such boundaries have been carefully analyzed: the distribution is random with no preference for low Σ boundaries.[14] Within the confines of the microstructural model proposed here (i.e., percolation through low-angle boundaries), the presence of a colony structure in the *c*-direction of the grains essentially serves to increase the available percolative options for current flow. Such a model is also consistent with other published observations.[15] They find that J_c decreases with the presence of 2212 intergrowths at grain boundaries. Because most grain boundaries observed here have a mixed character (i.e., have both tilt and twist components), the presence of thin layers of 2212 at the vicinity of the boundary can be expected to result in a decrease in J_c even if the misorientation angle is low.

The percolative model of current flow proposed here is also consistent with estimates of the active cross section of the material carrying the current. The J_c of Bi-2223 tapes for *H*//c in small magnetic fields has been compared with that of the best epitaxial films, and the J_c in the tapes was found to be smaller by 25–50.[16,17] In addition, using magnetization measurements, the J_c of good tapes was found to be an order of magnitude lower than the intragranular J_c.[18] Note that in all cases the active, strong-linked cross section is not greater than 10%. Also, at high fields the pattern of current flow appears to fragment into macroscopic islands connected by "narrow bridges," the dissipation within which is similar to that found within grains or across strong links.[18] Such observations are also consistent with the microstructural model developed here. The "narrow bridges" and

macroscopic islands may, in fact, be formed within the percolative network of low-energy boundaries, as the weaker boundaries in the network become resistive with increasing fields.

Results

In summary, X-ray and electron diffraction were used to study the microstructure of high-J_c PIT Bi-2223. Although the *c*-axis is nominally aligned perpendicular to the tape surface (FWHM ~20°), no in-plane grain orientation texture was observed on any scale. Characterization of grain boundary misorientations of 227 spatially correlated grain boundaries, however, indicates a grain misorientation texture in that a high fraction (~40%) of Σ-1, or low-angle, boundaries were found. In addition, 8% of the boundaries were within the Brandon criterion for CSLs >1 and <50. Grain boundary misorientation "texture maps" derived from the SEM image and misorientation data reveal the presence of percolative current paths consisting primarily of low-angle boundaries. *C*-axis misaligned and bent or curved grains increase percolative options for current flow. We propose that long-range, strongly linked current flow occurs through a percolative network consisting primarily of low-angle boundaries and perhaps also including low-Σ CSLs. Percolative current flow through a fraction of strongly linked boundaries has also been suggested by other studies of the transport properties of such tapes. Because most boundaries were found to have a mixed character (i.e., have both tilt and twist components), such a model assumes extension of the Dimos result[10] to mixed boundaries. The properties of such mixed boundaries have yet to be measured; however, energy-based arguments similar to those used to explain strongly linked behavior at other boundaries (e.g., [001] tilt boundaries) may apply.

TWO- AND THREE-DIMENSIONAL PERCOLATION IN HIGH- TEMPERATURE SUPERCONDUCTORS

We have developed a quantitative model for the high critical current densities (J_c) supported by superconducting materials with uniaxial alignment, such as *c*-axis textured Bi-Sr-Ca-Cu-O (BSCCO) tapes. Current follows percolative paths across small-angle grain boundaries. Because J_c is low for intragranular conduction parallel to the *c* axis, the three-dimensional flow required for percolation is produced by conduction perpendicular to the *c* axis in tilted grains. For optimized microstructures, J_c ranging from 3 to 30% of the intragranular value is predicted for percolation across small-angle grain boundaries with misorientations below 10° and 20° respectively.

Long lengths of BSCCO superconducting tape have recently been fabricated with high J_c, even in high magnetic fields. For the best samples, J_c ~ 5×10^4 A/cm^2 both at T = 77 K in zero-applied magnetic field *B* and at T = 4.2 K, *B* = 20 T. We hope that these materials will be useful for applications such as magnets and power transmission once their properties are optimized.[19]

These tapes consist of a uniaxially aligned layer or layers of BSCCO within a silver sheath. The layers are composed of grains with a high aspect ratio: grain thickness H (normal to the tape surface) is ~1 μm, while length L and width W are ~20 μm (Fig. 1.27). The *c* axes of the grains are aligned normal to the films, with a distribution of ~15° FWHM, while the *a* axes are oriented randomly in the plane of the tape. We use these essential properties to model current transport. More detailed microstructural characterization and its implications for current transport have been published.[20] What we refer to as "grains" are in fact "colonies" of grains joined by low-angle boundaries.

Despite broad agreement on the above description of BSCCO tapes, there is no consensus on the path followed by electrical current. The first model for the current path in *c*-axis textured materials without in-plane alignment was the brick wall model.[21,22] The brick wall model is based on an ideal microstructure shown three-dimensionally in Fig. 1.27 and in cross section in Fig. 1.28. The solid lines in Fig. 1.29 denote [001] tilt boundaries that we will call *ab* boundaries. The dashed lines are [001] twist boundaries that we call *c* boundaries. Both will typically be high-angle. The brick wall model assumes that the narrow *ab* boundaries carry negligible current. Although the *c* boundaries are high-angle, their large cross-sectional area can support high currents in spite of low J_c. Hence current follows the path shown schematically by the fine line in Fig. 1.28, crossing *c* boundaries only. Such a current path requires intragranular conduction in the *c* direction. Because intragranular J_c is much smaller in the *c* direction than in the *ab* planes, it limits the critical current density in the brick wall model.

However, measurements of the temperature dependence and anisotropy of J_c suggest that long-range current flow involves little or no *c* axis conduction, casting doubt on the brick wall mechanism.[23-26] Furthermore, cross sections of superconducting samples do not resemble the idealized brick wall of Fig. 1.28: few pure twist boundaries are observed. In addition, J_c measurements on BSCCO bicrystals show that most high-angle [001] twist boundaries do act as weak links.[27,28] These difficulties with the brick wall model led to the development of the railway switch model.[24,25]

According to the railway switch model, current within grains flows only in *ab* planes: conduction in the *c* direction does not significantly contribute. Current is transported across the thickness of the sample by grains tilted with respect to the average texture. Current flows between grains across apparent small-angle tilt boundaries.[24,25]

ORNL-DWG 95M-10396

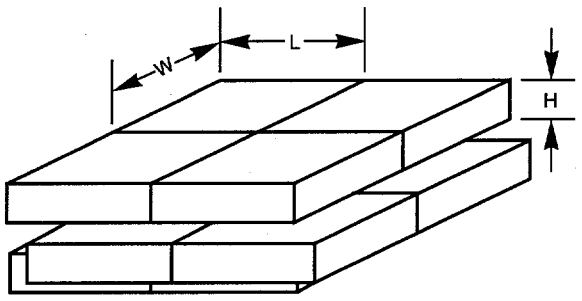

Fig. 1.27. Perspective view of a face-centered tetragonal brick wall microstructure. Each (001) plane forms a square lattice with primitive translations of ±½½ 0.

ORNL-DWG 95M-10396R

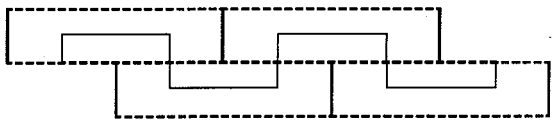

Fig. 1.28. Cross section of a brick wall microstructure. Heavy solid lines: [001] tilt boundaries. Dashed lines: [001] twist boundaries. Light solid line: current path in the brick wall model.

A key premise of the railway switch model is that the most frequently observed boundaries are small angle [*hk*0] tilt boundaries, also called *c*-axis tilt boundaries.[24,25] This conclusion is based on SEMs of cross sections of superconducting tapes.[25] We believe this conclusion is based on a misinterpretation of these micrographs. Many boundaries are observed that appear in cross section to be low-angle [*hk*0] tilt boundaries, as shown schematically in Fig. 1.29(*a*). However, the micrographs give no indication of the [001] tilt component of such a boundary. While some are

in fact low-angle boundaries [Fig. 1.29(*b*)], most are close to high-angle [001] tilt boundaries [Fig. 1.29(*c*)].

Little data has been published concerning J_c of grain boundaries in HTSs as a function of grain boundary character. The few published studies indicate that J_c for small-angle grain boundaries is close to intragranular J_c, while most high-angle grain boundaries act as weak links.[27,29-33] Reported values of the critical misorientation angle θ_c below which grain boundary J_c is high, range from 10 to 20°. Unfortunately, no estimate of θ_c is available for the BSCCO materials used in superconducting tapes.

We have characterized networks of small-angle grain boundaries in superconducting tapes and have proposed that long-range, strongly linked conduction occurs through a percolative network of small-angle grain boundaries.[34] Here we present a quantitative percolative model that explains how large J_c can be observed in materials in which only a small fraction f of the grain boundaries are small-angle. We assume that J_c is large when grain boundary misorientation is below θ_c of 10 to 20°, independent of other aspects of grain boundary geometry: this is consistent with all available data (Fig. 1.30). We further assume that all current flows in *ab* planes, as is indicated by $J_c(B,T)$ at high B. Our percolative model has an ideal face-centered tetragonal lattice of grains (Figs. 1.27 and 1.28). While grains in real superconducting tapes are far from close-packed,[25] we are most interested in the ultimate J_c that may be attained in superconducting tapes when the structure is optimized. As in the railway switch model, tilted grains carry current in the n direction (normal to the tape's surface). Quantitative numerical results are presented for the percolation of current through a small fraction of grain boundaries that are small-angle.

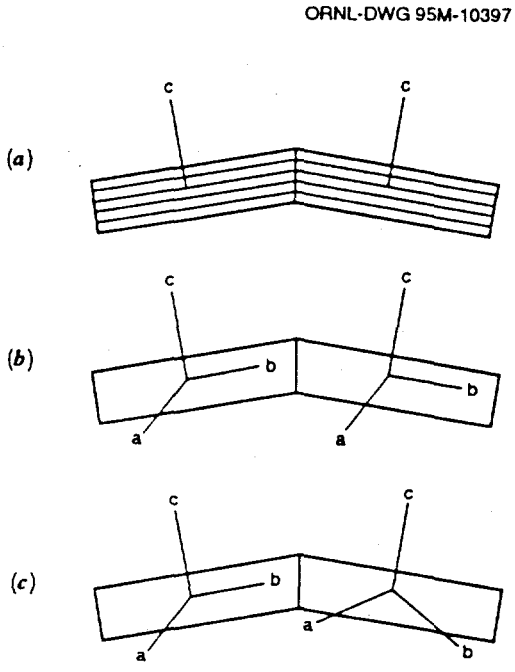

Fig. 1.29. (*a*) A cross section of the most commonly seen boundary shows only the [*hk*0] tilt component. (*b*) The boundary may in fact be a low-angle [*hk*0] tilt boundary. (*c*) But it is more likely to have a large [001] tilt component.

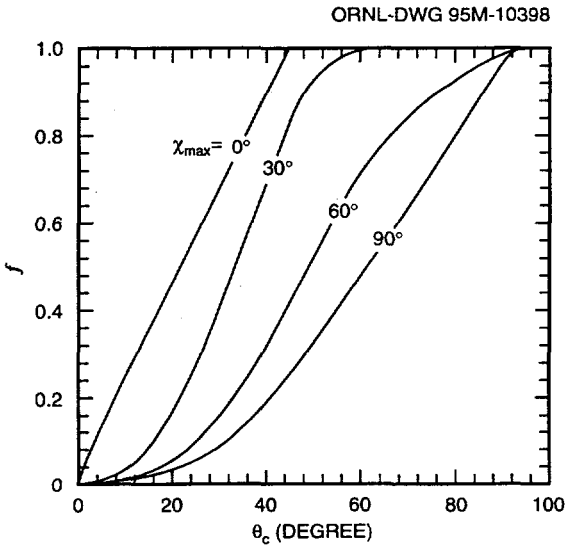

Fig. 1.30. Fraction f of grain boundaries with misorientation below θ_c for maximum tilt χ_{max} calculated numerically using 10^6 randomly oriented pairs of grains for each value of χ_{max}.

Percolation and Dimensionality

High total J_c can be carried by a material with a small fraction f of high J_c grain boundaries only when the sample combines the best aspects of

two- and three-dimensional current flow. For a sample with perfect *c*-axis alignment, the maximum misorientation of a boundary between tetragonal grains is 45°. We assume that high-J_c boundaries require misorientations θ less than a critical angle θ_c of 10–20°. With a random orientation about the *c* axis, 22–44% of grain boundaries have $\theta < 10$ to 20° (Fig. 1.31). Current flow, however, is strictly two-dimensional because there are no tilted grains to carry current normal to the sample thickness. In each *ab* plane of the model, the grains form a two-dimensional square lattice with a bond percolation threshold of 50%;[35] our model predicts that no current can percolate across a sample with perfect *c*-axis alignment. Even for the most favorable two-dimensional case of a hexagonal lattice, the percolation threshold is 35%; so the material is near or below the percolation threshold and high J_c is not possible.

The situation is the opposite for unaligned material. Current flow is truly three-dimensional; so percolation will occur when only 12% of the grain boundaries are conducting (for bond percolation on an fcc lattice).[36] However, only 3% of the grain boundaries have misorientations below θ_c of 20° (Fig. 1.31); so current cannot flow through low-angle boundaries in this limit either. An optimum *c*-axis texture lies between these extremes. When the grains are slightly tilted, current is transported three dimensionally, and large numbers of small angle boundaries are present. Numerical calculations demonstrate that large J_c can be supported in this manner.

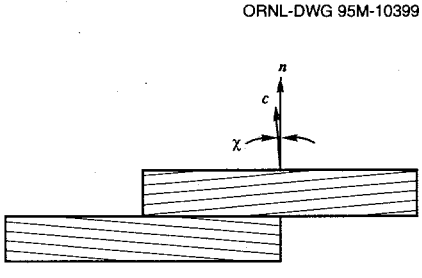

Fig. 1.31. The *c* axes superconducting grains make an angle χ to the sample normal *n*.

Calculation of J_c

As is described above, a face-centered tetragonal (fct) lattice of grains, shown in Figs. 1.27 and 1.28, is used to calculate J_c. Boundaries between grains separated by ±½ ½ 0 translations (with respect to the fct lattice) are *ab* boundaries and have a {110} habit (with respect to the fct lattice). Boundaries between grains separated by ±½ 0 ½ translations are *c* boundaries and have a (001) habit. This describes a brick wall microstructure.

Grains are assigned random orientations with the angle χ between their *c* axes and the sample normal *n* following a uniform distribution between 0° and χ_{max}; there is no preferred orientation of the *a* and *b* axes. Grain boundaries with misorientation greater than θ_c are nonconducting (i.e., $J_c = 0$). A key assumption is that θ_c depends on misorientation only. Grain boundary misorientation is the smallest angle of rotation between neighboring grain orientations. For tetragonal grain symmetry, misorientation angles fall between 0 and 45°. For misorientations below θ_c, conduction is anisotropic, reflecting the *c*-axis texture of the material: critical current density J_c^{ab} for *ab* boundaries will be larger than J_c^c for *c* boundaries. Small-angle *ab* boundaries do not act as weak links; so they will have critical current density $J_c^{ab} = J_c^{SC}$, the single crystal value, and critical current $I_c^{ab} = HW\ J_c^{SC}$, where H and W are defined in Fig. 1.27.

Because current flows in *ab* planes, current flows parallel to the sample normal *n* only in grains where the *c* axis is tilted by a nonzero angle χ from the sample normal *n* (Fig. 1.30). This angle is taken to be uniformly distributed between 0° and χ_{max}, where the tetragonal crystal symmetry requires that $0° < \chi_{max} < 90°$. In real materials, both the *c* axes of the grains and the grain boundaries will be tilted; we have simplified the model by considering only *c* axis tilts, leaving grain boundaries aligned to *n*.

Intragranular critical current density is J_c^{SC} flowing in the *ab* planes; so current density

across strongly linked c boundaries is $J_c^{SC}\sin\chi$. While we have calculated the fraction of strongly linked boundaries by assigning tilts to individual grains, we make the mean field approximation that the critical current densities of all strongly linked c boundary (i.e., those with $\theta < \theta_c$) are equal to the average value of the minimum critical current density of two neighboring grains. This was done to simplify calculations. Total J_c of the sample will depend on only three parameters: the fraction f of strongly linked boundaries and the critical currents of ab and c boundaries. The average critical current density normal to a c boundary for a single grain is, for small χ_{max},

$$\frac{J_c^{SC}}{\chi_{max}} \int_0^{\chi_{max}} d\chi \, \sin(\chi) = J_c^{SC}\left[1 - \frac{\cos(\chi_{max})}{\chi_{max}}\right] \approx \frac{J_c^{SC}\,\chi_{max}}{2}, \tag{1}$$

and the average of the minimum value for two grains is

$$\frac{J_c^{SC}}{\chi_{max}^2} \int_0^{\chi_{max}} d\chi_1 \int_0^{\chi_1} d\chi_2 \sin(\chi_2) = \frac{2J_c^{SC}}{\chi_{max}^2}\left[\chi_{max} - \sin(\chi_{max})\right] \approx \frac{J_c^{SC}\chi_{max}}{3}. \tag{2}$$

The area of c boundaries is LW/4; so the critical current normal to the c boundary is $I_c^c = LWJ_c^{SC}\chi_{max}/12$. Results are normalized so that a sample with perfect biaxial alignment (i.e., a c-aligned single crystal) has a total $I_c = 1$:

$$I_c^{ab} = \frac{1}{N^2}; \quad I_c^c = \frac{L}{H}\frac{\chi_{max}}{12N^2}, \tag{3}$$

where N^2 is the number of ab boundaries in a sample cross section. We take L/H = 20.

Each grain boundary can carry currents between $-I_c$ and I_c (as given by Eq. 3). The total critical current I_c of the sample is calculated using the labeling method[37] in which an exact solution is found by adding percolative paths until no conducting path can be added without exceeding the critical current of some boundary. Each grain forms a node on an fcc lattice. Each node is connected by 12 arcs (grain boundaries) to neighboring nodes.

I_c^{ab} (in the plane of the tape, as it is commonly measured) is calculated by applying periodic boundary conditions in the [010] and [001] directions (with respect to the fct lattice). The current source and sink are on the [100] faces. Infinite capacity is assumed within these faces, corresponding physically to good contacts covering each end of the sample. I_c^c (across the thickness of the tape) is similarly calculated by applying periodic boundary conditions in the [100] and [010] directions and placing the source, sink, and contacts on [001] faces. Note that I_c^{ab} flows across a cross section N^2HW, while the cross section for I_c^c is N2LW, larger by a factor of L/H = 20. Thus $J_c^{ab} / J_c^c = 20\, I_c^{ab} / I_c^c$.

The labeling algorithm is most efficient near and below the percolation threshold, where there are few percolative paths. Because this is the case where the largest sample size is required to obtain accurate results, sample size is varied to keep calculation time roughly constant, varying between a 14 × 14 × 14 lattice with 65,856 grain boundaries below the percolation threshold to a 5 × 5 × 5 lattice with 3000 grain boundaries well above the percolation threshold.

Results

For each combination of χ_{max} and θ_c, the fraction f of grain boundaries with misorientations below θ_c is calculated by examining 10^6 randomly generated boundaries.[38] Selected results are shown in Fig. 1.31. I_c is calculated from f and I_c. We calculate I_c using Eq. 3. Fig. 1.32 illustrates the relationship between I_c and f for several values of the grain boundary critical current anisotropy I_c^c/I_c^{ab}.

Random scatter in Fig. 1.32 is due to statistical variations in the calculation of I_c due to finite simulation size. For I_c^{ab}, these fluctuations

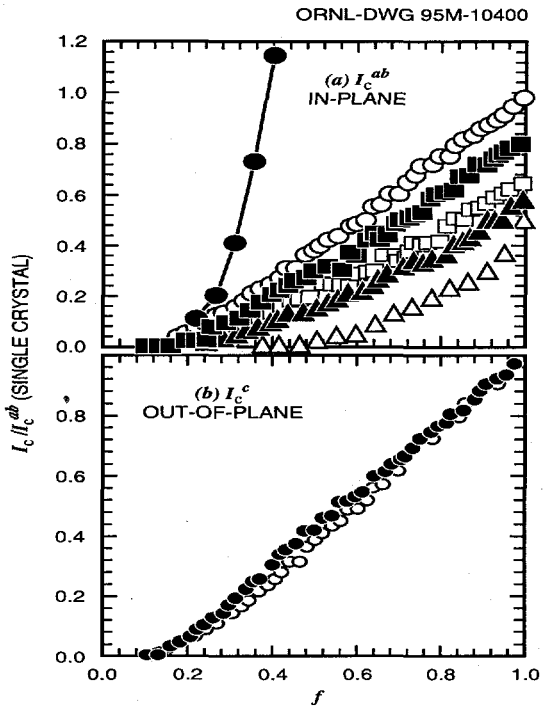

Fig. 1.32. Total (*a*) in-plane and (*b*) out-of-plane critical current as a function of the fraction of conducting grain boundaries for a variety of anisotropies in grain boundary critical current: $I_c^{ab} = \infty$ and $I_c^c = 1$(●), the three-dimensional case $I_c^{ab} = 1$ and $I_c^c = 1$(○), $I_c^{ab} = 1$ and $I_c^c = 63$(■), $I_c^{ab} = 1$ and $I_c^c = 0.32$(□), $I_c^{ab} = 1$ and $I_c^c = 0.16$(▲), and the two-dimensional case $I_c^{ab} = 1$ and $I_c^c = 1$(△). In each case, $I_c = 1$ correspondes to the single crystal in-plane value.

become large for anisotropies less than 0.1. Results are obtained for these values by multiplying the result for $I_c^{ab} = \infty$ and $I_c^c = 1$ by the value of I_c^c. Accurate values for $I_c^{ab} = \infty$ and $I_c^c = 1$ were obtained by running calculations on a 14 × 14 × 14 lattice. This calculation is time-consuming but must be performed only once for each value of f. Note that Fig. 1.32(*a*) includes two sets of points for the limit $I_c^{ab} >> I_c^c$. In this limit, I_c is zero for conducting fraction $f < 0.12$ (the three-dimensional fcc bond percolation threshold), proportional to (1) I_c^c [filled circles, Fig. 1.32(*a*)] for $0.12 < f < 0.5$ (the two-dimensional square bond percolation threshold) when weak *c* boundaries couple *ab* planes that are themselves below the percolation threshold and (2) I_c^{ab} [open triangles, Fig. 1.32(*a*)] for $0.5 < f < 1$ when current can flow without crossing weak *c* boundaries. As f approaches 0.5 from below, I_c diverges to ∞ times I_c^c [filled circles, Fig. 1.32(*a*)]; as f approaches 0.5 from above, I_c approaches 0 times I_c^{ab} [open triangles, Fig. 1.32(*a*)].

I_c^c depends only weakly on I_c^{ab}. As shown in Fig 1.32(*b*), there is at most a 20% difference between I_c^c for $I_c^{ab} = 1$ and $I_c^c = 1$ [open circles, Fig. 1.32(*b*)] and I_c^c for $I_c^{ab} = \infty$ and $I_c^c = 1$ [closed circles, Fig 1.32(*b*)]. For this reason, we can make the approximation $I_c \approx I_c^{ab} I_c(I_c^{ab} = 1, I_c^c = 1)$. Although I_c^c depends primarily on I_c^c, note that I_c^c depends on intragranular J_c^{ab}, because our percolation model neglects intragranular J_c^c.

I_c, normalized to single crystal I_c^{ab}, is shown in Fig. 1.33. The maximum I_c^{ab} is sensitive to θ_c, increasing from 3 to 30% as θ_c is doubled from 10 to 20°. This is because the material is close to the threshold for percolation of current through *ab* boundaries with high J_c; and a small change in θ_c, and thus in f, makes a large change in the number of *c* boundaries with low J_c needed for current to traverse the sample. The optimum χ_{max} varies proportionately to θ_c from 5 to 10°. I_c will vary proportionately with the grain aspect ratio L/H as well, finally saturating when three-dimensional percolation is reached at L/H = $12/\sin(\chi_{max})$, or 70–140.

I_c^c varies much as I_c^{ab}. This is to be expected, since our model predicts conduction by a three-dimensional percolation mechanism. For small θ_c, f is far below the two-dimensional percolation threshold of 0.50; so percolation is very isotropic and $I_c^c \approx I_c^{ab}$. For $\theta_c = 10°$ and $\chi_{max} = 8°$ (e.g., $I_c^{ab}/I_c^c = 1.1$). As is noted above, the ratio of total critical current densities will be $J_c^{ab}/J_c^c = 22$. For larger θ_c, f is closer to the two-dimensional percolation threshold, percolation is more anisotropic, and $I_c^c < I_c^{ab}$. For $\theta_c = 20°$ and $\chi_{max} = 8°$ (e.g., $I_c^{ab}/I_c^c = 2.0$ and $J_c^{ab}/J_c^c = 40$).

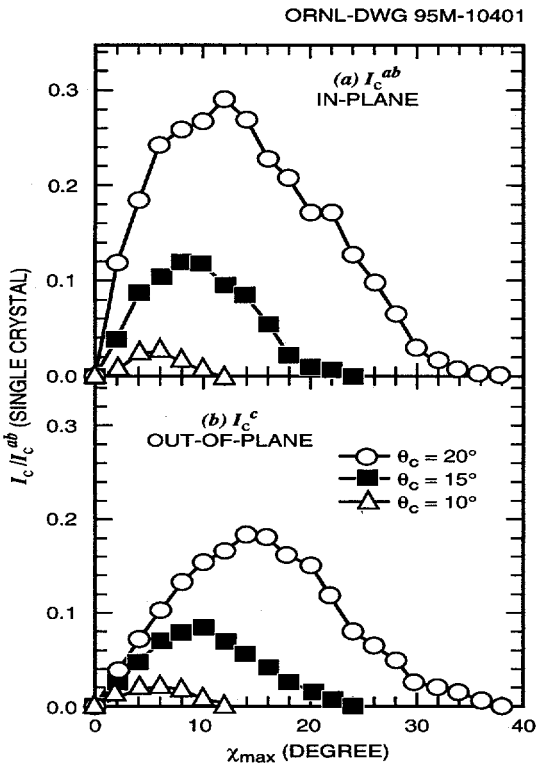

Fig. 1.33. Total (*a*) in-plane and (*b*) out-of-plane critical current, normalized to single crystal values, as a function of maximum tilt for the experimentally observed range of critical misorientation values.

Discussion

The I_c's predicted by the percolative model are higher than those observed in BSCCO tapes. The percolative model predicts 3–30% of single crystal I_c, depending most on θ_c, for an ideal structure. The best tapes have $J_c \sim 5 \times 10^4$ A/cm^2 (T = 77 K, B = 0), or ~0.5% of single crystal J_c. Existing tapes contain numerous gaps between grains;[24,25] so it is to be expected that substantial increases in J_c will result from the production of a more closely packed microstructure. The optimum χ_{max} of 5–10° is consistent with the 15° FWHM typically observed in optimized tapes. A better check of the percolative model calculation will require measurement of θ_c for BSCCO materials as well as production of more closely packed tapes.

The measurement of J_c^c remains an experimental challange. While the critical current I_c^c has been measured,[23,25] the critical current density J_c^c has not been reported. Such measurements will test our prediction that J_c^{ab}/J_c^c is 20 to 40 for the percolative model. A key distinction between the percolative model and the brick wall model is that I_c for the percolative model falls to zero as *c*-axis texturing is reduced below its optimum value of 5 to 10°.

According to the brick wall model, I_c should remain high for even the best-aligned samples. A test of this prediction will require production of BSSCO films with excellent *c*-axis alignment (<2° FWHM) and no in-plane alignment. According to the percolative model, significant current in such films cannot flow through a network of strongly linked grain boundaries, and high J_c cannot be produced in strong applied magnetic fields.

In common with other models, the percolative model predicts that I_c will increase as the aspect ratio of grains increases. Further experimental data is required to check a key premise of the percolative model: that grain boundaries are weak links unless total misorientation is small and conversely that all small-angle boundaries act as strong links.

The calculations presented here are best-case predictions because they assume a perfect lattice of grains. In real materials there will always be some gaps separating grains; so real J_c can only approach these values. Three-dimensional percolation requires $f > 12\%$; for $\chi_{max} = 0°$ (which maximizes f), f ranges from 22 ($\theta_c = 10°$) to 44% ($\theta_c = 20°$). Thus a minimum of 27–55% of the grain boundaries must be connected for strongly linked conductivity to occur.

The assumption that only small-angle grain boundaries can have high critical currents may be unduly pessimistic, however. Some large-angle [001] twist boundaries have been found with J_c as large as the intragranular value.[27] Note, however, that intragranular J_c for these boundaries is in the *c* direction and is therefore limited to low values. Large-angle grain boundaries with truly high J_c have not been observed. A final possibility for J_c greater than

predicted by the percolative model is that low-angle boundaries may occur with greater frequency than dictated by chance alone (i.e., local orientational order may occur).[34]

ROLLING-ASSISTED BIAXIALLY TEXTURED SUBSTRATES

A new process to fabricate long lengths of flexible, near single-crystal-like, chemically compatible substrates was developed. The process is termed rolling-assisted biaxially textured substrates (RABiTS™). Figure 1.34 shows the (111) pole figure of the substrate surface. Clear evidence of the strong in-plane texture is evident. Determination of grain boundary misorientations in millimeter-size regions of the substrate shows that over 95% of the boundaries are small angle.

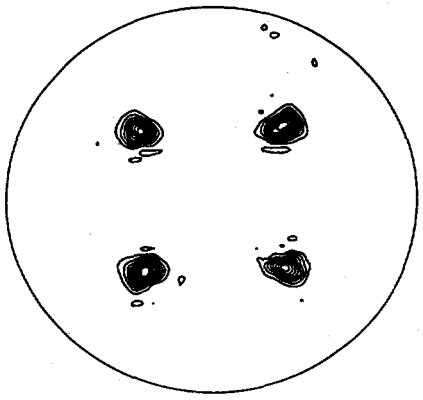

Fig. 1.34. Pole figure (111) of a RABiT™ substrate surface showing strong in-plane texture.

Superconducting films were successfully grown on these substrates. Figure 1.35 shows a (226) ϕ scan for a $Y_1Ba_2Cu_3O_x$ (YBCO) film on RABiTS™. Sharp biaxial texture is evident. The films have sharp superconducting transitions at 90 K. The critical current density (J_c) of the film is shown in Fig. 1.36. Zero-field J_c of an early film is about 3×10^4 A/cm^2. The data are compared with a typical ion-beam-assisted

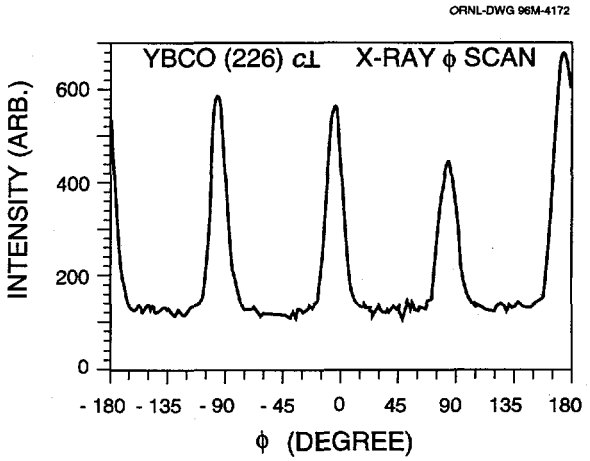

Fig. 1.35. X-ray (226) ϕ scan for a $Y_1Ba_2Cu_3O_x$ 1-μm-thick deposit on a RABiT™ substrate showing sharp biaxial texture.

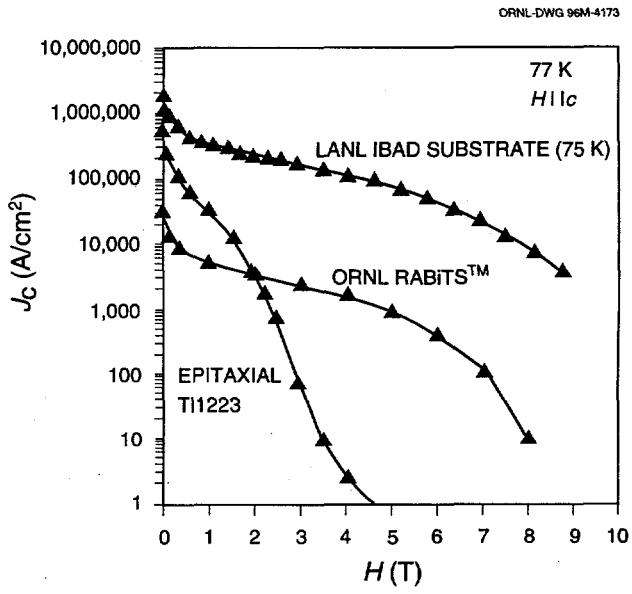

Fig. 1.36. Critical current density of $Y_1Ba_2Cu_3O_x$ deposits on an Oak Ridge National Laboratory RABiT™ substrate and a Los Alamos National Laboratory ion-beam assisted (IBAD) substrate as a function of applied magnetic field (*H*⊥*c*). The films are compared with an epitaxial T1-1223 film prepared by the State University of New York at Buffalo.

deposition (IBAD) film from Los Alamos National Laboratory and a new State University of New York epitaxial, T1-1223 film. The film is quite porous (i.e., the substrate may be seen through "gaps" in the superconductor); therefore, there is significant room for improvement in J_c.

The in-field J_c of the film on the RABiT™ substrate is similar to that of the IBAD film (Fig. 1.37) where the normalized J_c is plotted. This indicates that the film on RABiTS™ is well linked, but there is some geometrical scaledown of the J_c . The in-field behavior of the film for *H*||*ab* is indicated in Fig. 1.38. The field behavior and anisotropy are typical to that of a single-crystal YBCO film on $LaAlO_3$ or $SrTiO_3$. A newer film has a yet higher J_c (~80,000 A/cm^2) and shows superior in-field performance compared with the thallium films on YSZ substrates (Fig. 1.39). Further efforts are in progress to overcome the current limitations.

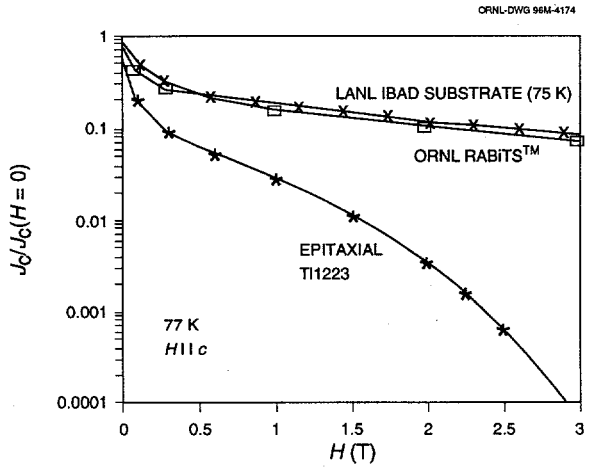

Fig. 1.37. Normalized critical current density of $Y_1Ba_2Cu_3O_x$ films on RABiT™ and IBAD substrates as a function of applied magnetic field (*H*||*c*). The YBCO films are compared with an excellent epitaxial T1-1223 film prepared by the State University of New York at Buffalo.

Regarding scale-up of the process, many issues still need to be addressed. However, no significant bottleneck is currently envisaged. A number of companies have indicated an interest in the technique and are currently in the process of submitting proposals to ORNL for joint work/ development. In conclusion, the feasibility of RABiTS™ as a process has been successfully demonstrated. Ongoing work is aimed at achieving higher J_c's and in developing bulk processes for depositing the YBCO (or thallium) on RABiTS™.

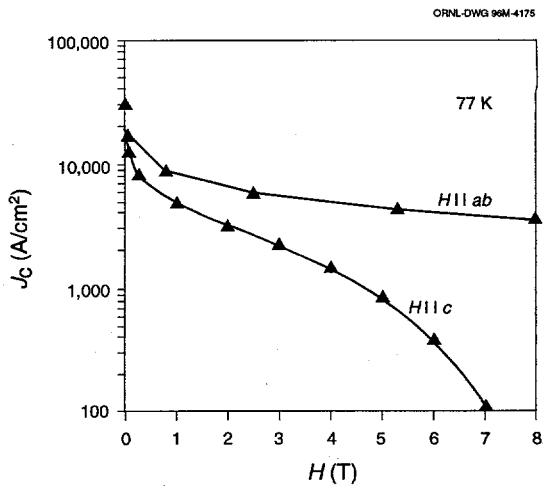

Fig. 1.38. Anisotrophy of an Oak Ridge National Laboratory $Y_1Ba_2Cu_3O_x$ deposit (1-μm thick) on RABiTS™. The field behavior is typical of that observed for single-crystal YBCO on $LaA1O_3$.

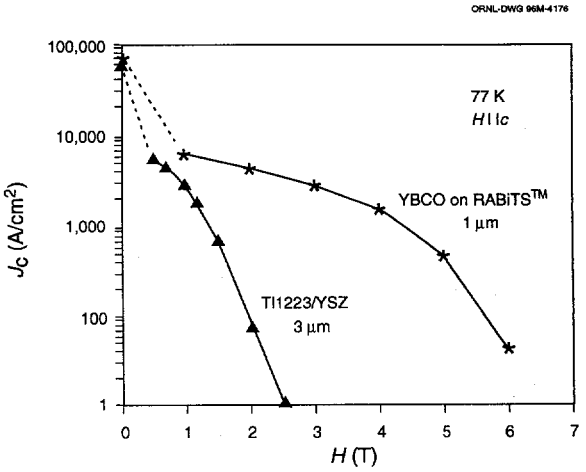

Fig. 1.39. Critical current density of a second $Y_1Ba_2Cu_3O_x$ deposit on RABiTS™ as a function of applied magnetic field. The J_c (*H* = 0) is now ~80,000 A/cm^2. A typical T1-1223 thick deposit on yttria-stabilized zirconia is shown for comparsion.

CONDUCTORS FOR HIGH-TEMPERATURE, HIGH-FIELD APPLICATIONS

Work on thallium conductors was performed in close collaboration with General Electric Company (GE) and Intermagnetics General Corporation (IGC). The key objectives of this joint technology development were:

- investigation of the effect of local texture and grain boundary networks on J_c and development of superior microstructures;
- analysis of the effects of processing conditions on microstructural modifications with respect to grain boundary networks;
- fabrication of thicker films with higher J_c's and determination of J_c limiting mechanisms in these thicker films made using powder deposits;
- development of alternate deposition techniques to make precursor films;
- thallination of long lengths of conductors in a scalable, continuous thallination reactor;
- demonstration that two-zone thallination is competitive with current BSCCO technology in terms of processing times required;
- development of an alternate thallination scheme to thallinate long lengths or coils of coated precursor tapes in a static configuration; and
- microstructural superconducting characterization of post-thallinated dip-coated samples.

Reported in detail here are results of the first four listed tasks (with GE), which were performed primarily at ORNL, and results of the last task (with IGC).

Effect of J_c on Local Texture and Grain Boundary Networks and Design of Superior Microstructures

Microstructural studies were aimed at (1) obtaining a direct correlation of the microtexture and percolative current flow as predicted by prevalent colony microstructure in the films, first, by studying the effect of conductor geometry on J_c and, secondly, by magneto-optical visualization of current flow in the films and (2) expanding the database of grain boundary characteristics in Tl-1223 films.

Effect of Conductor Geometry on J_c

Figure 1.40 shows the most likely *a*-axis orientations in a 4 × 5 mm^2 region of a 3-μm-thick Tl-1223 film on YSZ made by spray pyrolysis followed by two-zone thallination. The data were obtained at the National Synchrotron Light Source at ORNL beam line X-14. A sagittally focusing silicon (111) monochromator was used to select an X-ray wavelength of 0.1409 nm, which is slightly longer than the copper-potassium absorption edge, yielding a small X-ray absorption coefficient of 0.11 μm^{-1} for Tl-1223 and ensuring that the entire 3-mm film was illuminated. A 0.1-mm-diam circular

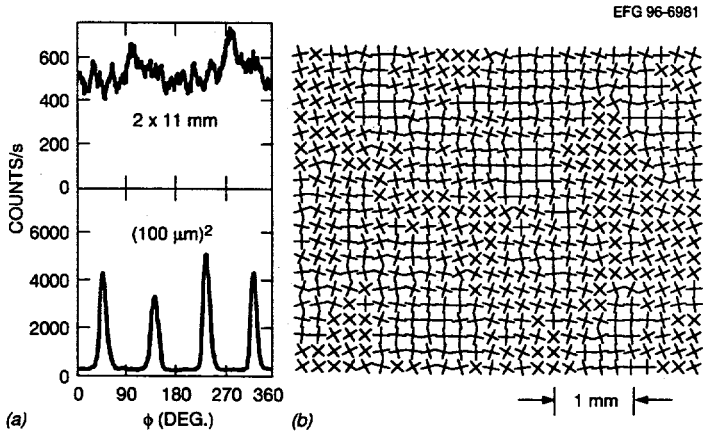

Fig. 1.40. Colony microstructure in General Electric Company Tl-1223 films leading to superior transport properties: (*a*) X-ray scans with a large and a small beam (the presence of local texture is evident on reducing the size of the beam) and (*b*) map of the most likely grain orientations in a 4 × 5-mm region of a film.

aperture in a platinum foil was placed 32 mm upstream of the sample. Convolution of the 4.5-mrad (0.17) horizontal and vertical divergence of the beam with the aperture size yields a spot size at the sample of 0.13-mm (0.09) FWHM. The flux was ~10^9 photons/s. As reported previously, the *c* axis is aligned to within 2° of normal to the film. Using the {1 1 18} reflection, X-ray ϕ scans were then measured. Typically, four peaks are observed for a rotation of 360° about the sample normal, consistent with the tetragonal symmetry of the material. The colony structure in the sample is evident. It would be intuitively expected that the critical current density of a sample with such a microstructure will be dependent on the bridge dimensions because of change in percolative options by the geometry of the bridge.

The critical current density of the sample was then measured as a function of the applied field by successively reducing the bridge width. The dimensions of the entire sample were 8 × 12 mm^2. The first measurement was made at a full width of 8 mm. On successively reducing the bridge width further, the J_c is expected to decrease as the percolative options decrease, as can be envisioned by Fig. 1.40. Figure 1.41(*a*) shows the J_c(0 T, *H*//*c*) and J_c(1 T, *H*//*c*) as a function of the bridge width. The sample marked SS-638 is the sample for which local orientation data is shown in Fig. 1.40. Both at 0 T as well as 1 T, the J_c decreases with decrease in bridge width. This indicates that both the fraction of weakly coupled, as well as strongly coupled, regions change with decrease in bridge width. This is well illustrated by Fig. 1.41(*b*), which shows J_c as a function of field for sample SS-638 and the curve at a width of 0.08 mm corresponding to SS-520. At the smaller widths an increase in the fraction of weak links is evident.

The critical current density of the sample with the microstructure shown in Fig. 1.40 can also be theoretically estimated using limiting path calculations. Details of the methodology of the limiting path calculations have been

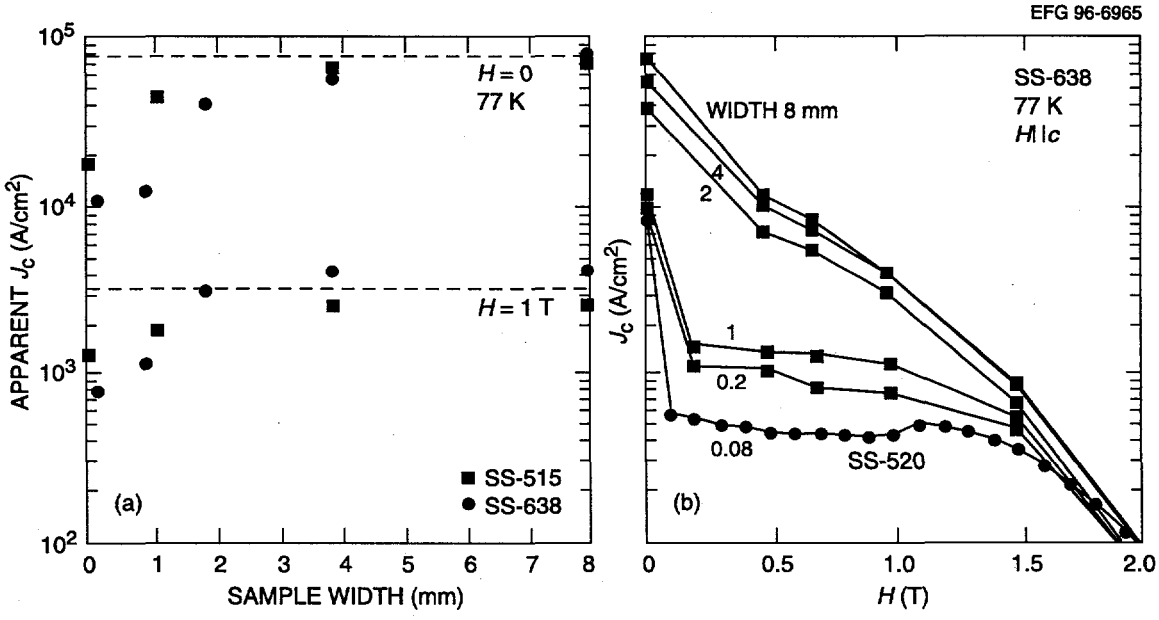

Fig. 1.41. Recent experiments on bridge width dependence on J_c. As the percolative options decrease, the fraction of well-coupled regions becomes small, and the dissipative properties are dominated by weak links at low and intermediate fields: (*a*) J_c (0 T, *H*//*c*) and J_c (1 T, *H*//*c*) as a function of bridge width; (*b*) J_c as a function of field for various bridge widths for sample S- 638.

reported.[39] The calculations were made using the J_c vs misorientation data reported by Nabatame et al.[40] The results obtained are shown in Fig. 1.42. Calculations were made by placing the bridge at all possible locations on the 4 × 5 mm^2 region depending on the width of the bridge. The average value of J_c is indicated by the solid line. The maximum and minimum J_c for each bridge width is also shown by the dashed lines. Consistent with the experimental data shown in Fig.1.41, the J_c decreases with decrease in bridge width. The magnitude of the decrease is also similar. This provides the first such result on a polycrystalline superconductor where the percolative nature of the current is clearly illustrated.

preparation) and the University of Wisconsin (magneto-optical imaging). Shown in Fig. 1.43 is a plot of most likely *a*-axis orientations as a function of location on the bridge. The inset of the figure shows the bridge geometry. The bridge dimensions were 0.2 × 4 mm; the bridge has four segments of 1 mm each. The measured J_c of the bridges is shown on the *x* axis of the figure. Between regions 2 and 4 of the bridge, the *a*-axis orientation changes continuously by ~30°. However, at no point was this accomplished by an abrupt change in the *a*-axis orientation. The J_c of this region is expected to be high—in agreement with the measured values of > 80 kA/cm^2. On the left of point 2, there is an abrupt change in the *a*-axis orientation,

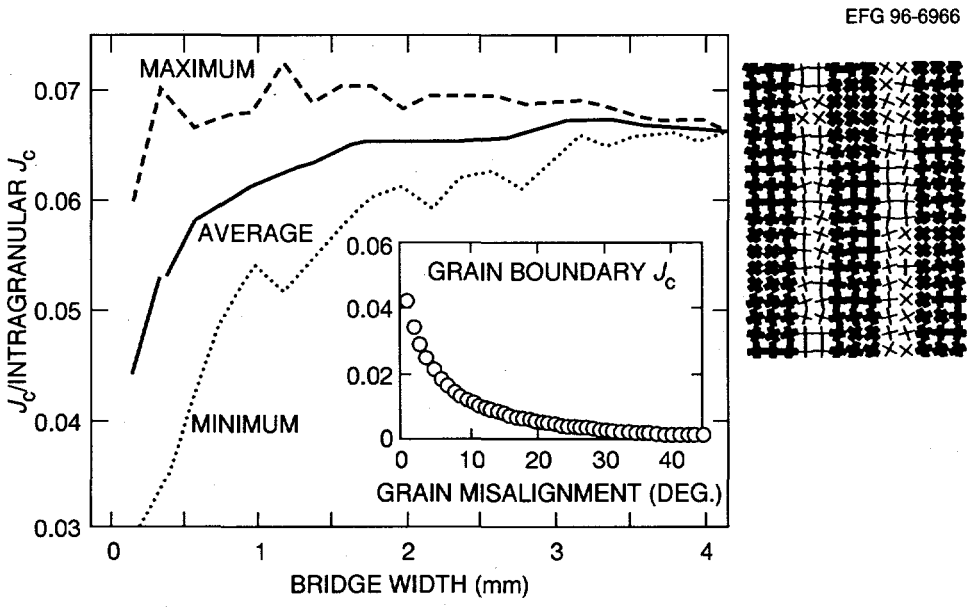

Fig. 1.42. Limiting path calculations correctly predict large variations in the critical current of short, narrow bridges and the decrease in J_c with decrease in bridge width.

Visualization of Current Flow in the Films

The percolative nature of the current flow was further studied by correlating the observed microtexture with measured J_c and current flow visualization by magneto-optical imaging. Figures 1.43 and 1.44 show two such cases. This experiment was a collaboration between ORNL (microtexture measurements), GE (sample

corresponding to a high-angle colony intersection, where the average misorientation between the colonies is ~30°. Hence a reduction in J_c is expected at this point in agreement with the measured value. Note that even though the average misorientation between the colonies is 30°, because the colony FWHM is also close to 20°, there is a significant overlap in orientations, resulting in many small-angle boundaries at the

colony intersections (as has been previously observed by electron backscatter diffraction). The presence of such small-angle boundaries is what allows the passage of some current through such a high-angle intersection. Shown at the bottom of the figure are two magneto-optical images taken at 9 K at 232 and 400 Oe respectively. The light regions in the image correspond to locations where flux has penetrated and can be interpreted as lower J_c regions. Magneto-optical images show most of the area between region 1 and 3 of the bridge. The image is in complete agreement with the microtexture results and the measured J_c.

To further establish the correlation between microtexture and J_c observed in Fig. 1.43, another sample that contained the highest J_c segment obtained thus far was studied. Figure 1.44 shows the results. At the top of the figure is a contour plot of the most likely *a*-axis orientations, and at the bottom are the corresponding magneto-optical images. Again, the correlation between microtexture and J_c is clearly evident. The results in Figs. 1.43 and 1.44 demonstrate (the first time for any polycrystalline high-temperature superconductor) a direct correlation between texture, measured J_c and current visualization.

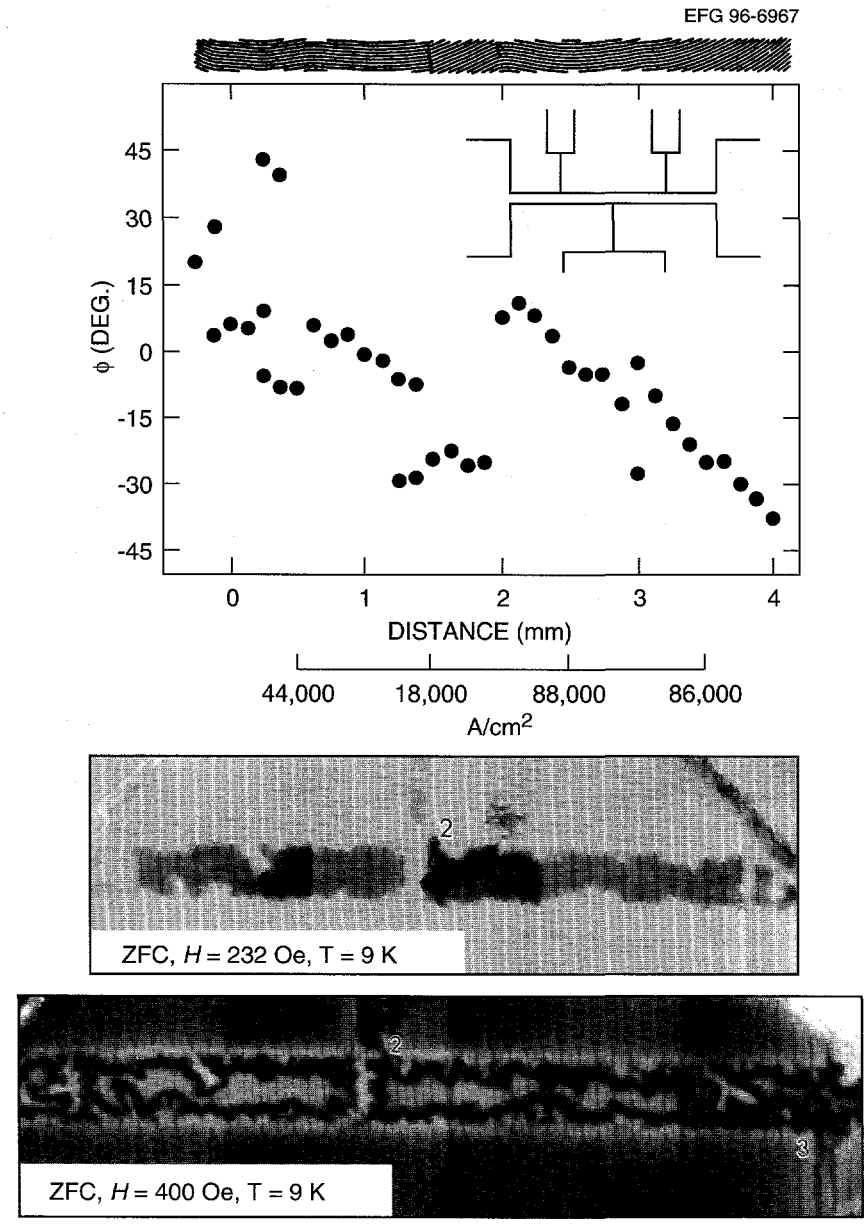

Fig. 1.43. Excellent correlation between microtexture data and percolative current flow as determined by magneto-optical imaging.

Statistics of Grain Boundary Misorientations in Tl-1223 Films

Using electron backscatter Kikuchi diffraction, grain boundary studies were expanded to over 1500 grain boundaries. Results show that small-angle boundaries are predominant (>60%) and that a large fraction of high-angle boundaries at colony intersections are within the Brandon criterion for a coincident site lattice boundary. These statistics on grain boundary characteristics serve to confirm earlier measurements and interpretations on current flow in these films.

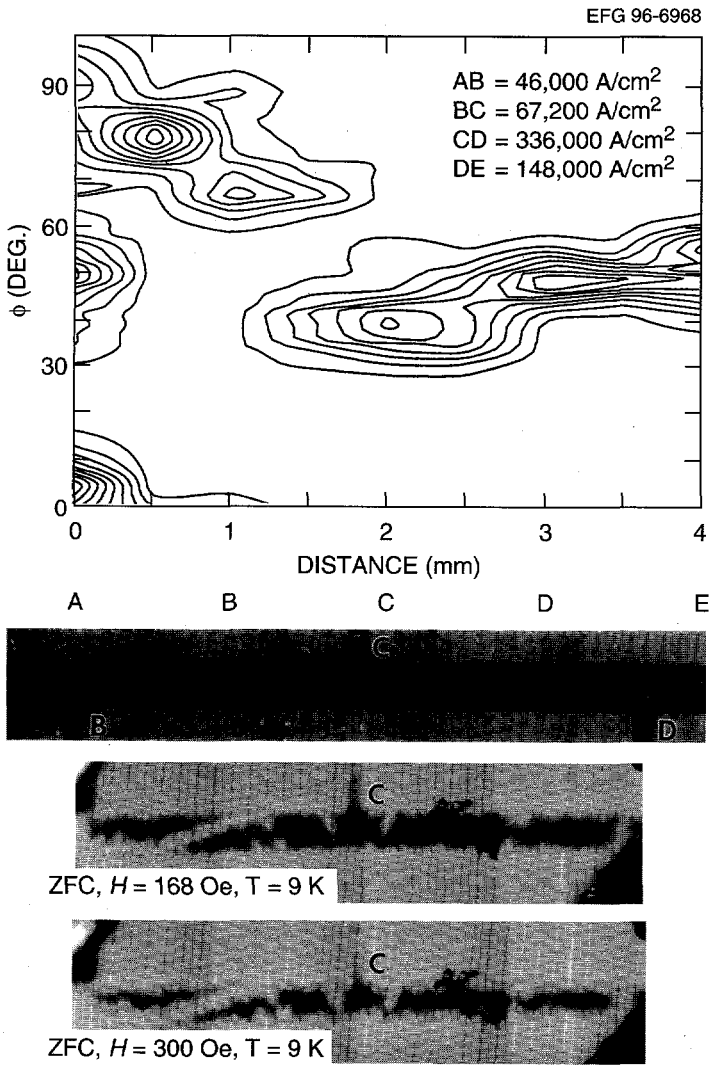

Fig. 1.44. Grain orientation texture and percolative current flow in highest J_c sample.

Effects of Processing Conditions on Microstructural Modifications with Respect to Colony Structure

We previously reported that colonies form on crystallization, that nucleation of the colonies occurs at the film/substrate interface, and that this effectively results in directional solidification for typical two-zone thallination conditions. We also reported that the average colony mosaic decreases with processing time and that colonies grow during cooling in a typical flow reactor when the sample is stationery. Continuing our previous work in accordance with the goals of the program for scale-up of the thallination process, samples fabricated in a specially designed, continuous thallination reactor at GE were studied.

Figure 1.45 (*a* and *b*) shows colony characteristics as a function of holding time for films made in a continuous thallination reactor. The samples were moved by stepping along the furnace to the appropriate zone and then air- quenching after the desired holding time. Fig. 1.45(*a*) shows that the colony mosaic, or the spread in *a*-axis orientations, decreases with increase in holding time. Fig. 1.45(*b*) shows that colonies grow with holding time. These results are in agreement with observations made previously on samples made using a

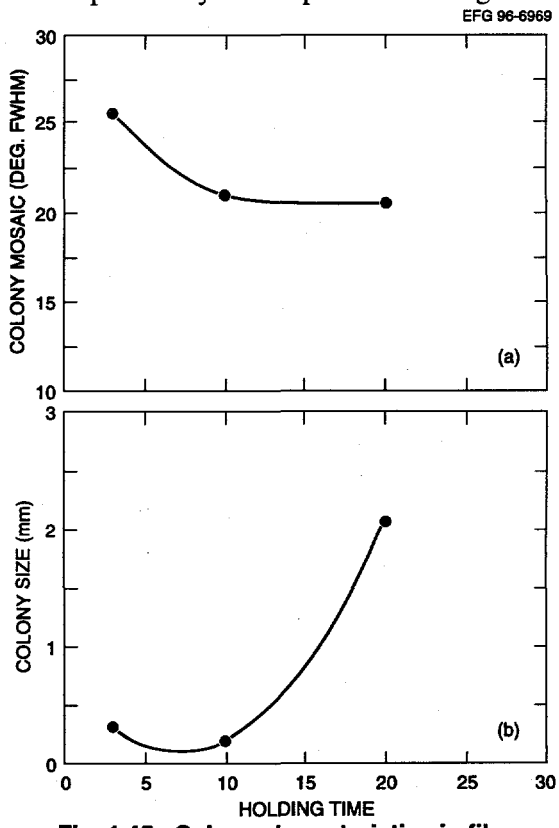

Fig. 1.45. Colony characteristics in films processed in a special, continuous thallination reactor: (*a*) colony mosaic; (*b*) colony size with holding time.

stationery flow reactor and indicate that the hypothesis developed earlier will be applicable to samples made using the continuous reactor.

One of the scale-up issues is processing time: this should be minimized for thallination as much as possible. This can be accomplished by increasing the thallium flow rate, which increases the rate at which thallium is incorporated into the precursor film. However, more rapid solidification can be expected to result in less-well-formed colonies. Figure 1.46 shows the colony mosaic as a function Tl_2O flow rate for a fixed sample holding time at the thallination temperature of 860°C for 5 min. As expected, the colony mosaic increases with increase in flow rate, concomitant with a decrease in J_c. While complete thallium incorporation is accomplished within 5 min, further optimization of the flow rate, hence the colony FWHM, is required to maximize the critical current density. The effect of colony FWHM on J_c is reported elsewhere.[39]

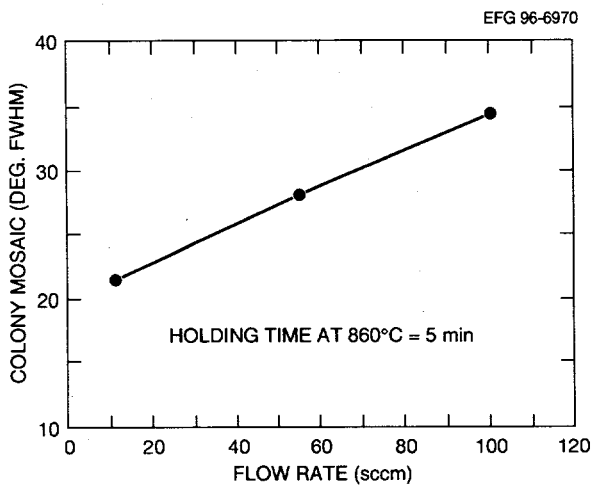

Fig. 1.46. Colony characteristics as a function of Tl_2O flow rate. J_c (55 sccm) = 17.5 kA/cm²; J_c (100 sccm) = 10.1 kA/cm².

Under special conditions during thallination, a continuous reactor, long-range, biaxial texture was obtained in one case. Figure 1.47 shows a contour plot of most likely *a*-axis orientations as a function of the distance on the sample. A single large colony is seen to span the entire length of the sample. Clearly, further work aimed at establishing conditions where such a microstructure is obtained is required.

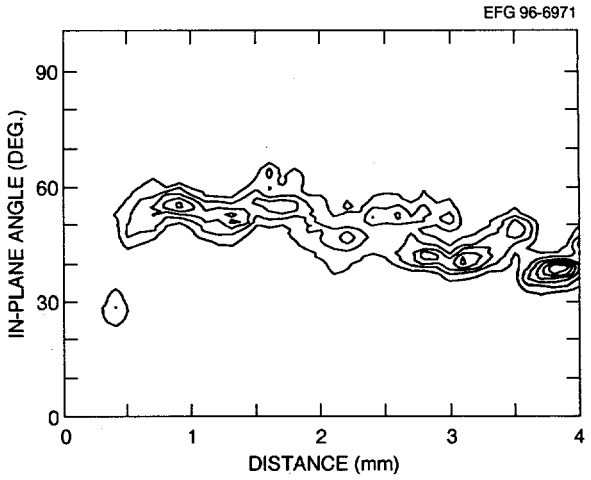

Fig. 1.47. Continuous thallination under special conditions resulted in long-range biaxial alignment.

Fabrication of High-J_c and I_c Thick Films

Efforts at ORNL for the last year were focused on developing methods to fabricate high-J_c and I_c Tl-1223 films on practical substrates (e.g., silver). A variety of deposition processes were explored including spray-pyrolysis, sol-gel, sputtering, and spin-coating/dip-coating/painting to fabricate the precursor films. The films were subsequently thallinated in a two-zone reactor. The objective in each case was to be able to fabricate films with a performance criterion of 10 A/mm as stated by industry (GE). Results are shown in Table 1.2.

Table 1.2. Performance criteria of fabricated films at Oak Ridge National Laboratory

Disposition technique	Film thicknesses (μm)	Maximum J_c, *H*//*c*, 77 K (A/cm)
Spray-pyrolysis on silver	1–3	65,000
Sputtering	1–2	50,000
Powder percursors	10–20	20,000[a]
Sol-gel and spin-coating	1	20,000

[a] I_c = 30 A.

While high J_c's are obtained in films made by spray-pyrolysis and sputtering on silver, these techniques are less amenable to scale-up to produce long lengths, as well as thicker films, to meet the I_c/width criterion of 10 A/mm. Films made at GE using spray-pyrolysis on YSZ indicate that in some cases, relatively thick films can be made that do meet this criterion.

Thick films can be rapidly made by deposition of powder precursors on the substrate and can be accomplished by dip-coating, doctor-blading, screen printing, or painting. Table 1.2 shows that the highest J_c achieved to date is only 20,000 A/cm^2. Among all reports for powder precursor films, this is the highest number achieved thus far. Figure 1.48 shows the field dependence of the J_c for these films compared with typical results obtained using any of the other deposition techniques (e.g., spray-pyrolysis or sputtering). The thicker powder deposits (up to 30 μm) on silver are not

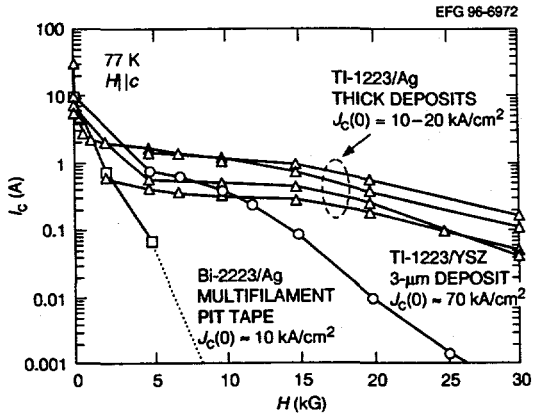

Fig. 1.48. High J_c and improved high-field critical current observed in powder deposits on silver.

as well *c*-axis-textured as films made on YSZ using the other techniques. However, like the films on YSZ, they have well-developed colonies, as is indicated in the ϕ scan shown in Fig. 1.49. Because the films consist of regions of locally aligned grains, they can be expected to consist of some well-linked current paths. The data in Fig. 1.48 show that is indeed the case. Also interesting is the fact that they appear to exhibit a larger irreversibility field than thinner films made by more controlled deposition techniques and having much sharper *c*-axis FWHM. Two possible reasons for the difference in the field are:

- the larger J_c (H_{ab}) component present when the field is nominally applied perpendicular to the substrate owing to the less perfect *c*-axis alignment and
- enhanced irreversibility field at *H//c* owing to creation of flux-pinning defects.

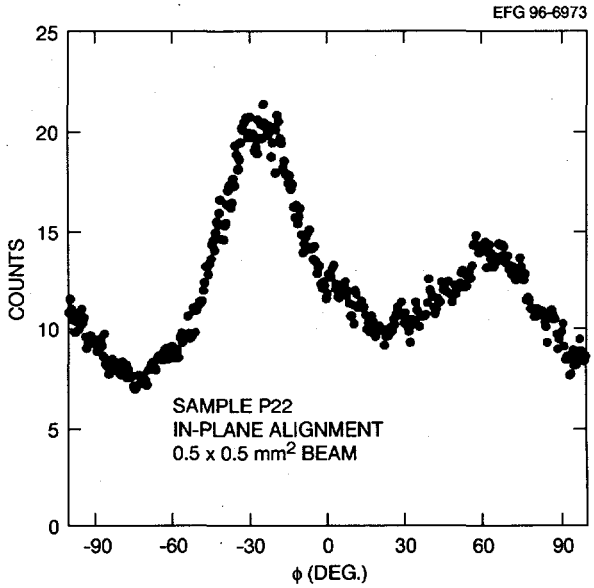

Fig. 1.49. Strong local in-plane (i.e., "colony") structure is observed in *c*-axis-aligned regions.

Factors limiting J_c in thick powder deposits

Several factors contribute toward the low J_c's achieved in powder deposits compared with spray-pyrolyzed deposits. These include:

- Compositional inhomgeniety. In general, a fine dispersion of phases is desirable. This is naturally obtained using a multicoat spray-pyrolysis technique for depositing the precursor. Although bulk methods to synthesize powders result in considerable composition in homogeniety, powders fabricated using aerosol pyrolysis are similar

to precursors made by spray-pyrolysis. Most work at ORNL has focused on powders made using this technique. Typical powders are of 1-μ diam and retain the compositional homgeniety within each particle. This factor is therefore not considered a limiting factor in our case.

- Effect of a rough silver interface in hindering texture development. This was found to be one of the important factors limiting J_c's in thick powder deposits. Precursor films deposited using spray-pyrolysis can be deposited under conditions such that the film is very dense after postannealing. Densities greater than 80% are easily achieved, and no mechanical densification steps are necessary, such as pressing or rolling. On the other hand, powder deposits made by either spin- or dip-coating need significant mechanical deformation for densification. Typically, a pressing step is employed after film coating. Because the silver substrate is much softer than the ceramic powders, the powders penetrate the silver and create a very rough interface.

In 1995 we showed that the Tl-1223 forms during thallination in a two-zone reactor, first, at the film/substrate interface on the side closer to the thallium source. Then the growth front moves up through the thickness and along the length of the film. This, together with the tendency of most superconductors including Tl-1223 to form interfaces with the low-surface energy (001) plane, results in a situation schematically illustrated in Fig. 1.50(*c*). Figure 1.50(*a* and *b*) shows an example of a rough and a smooth interface with silver in Tl-1223 films. A rough interface results in the nucleation of *c*-axis misaligned grains. Because growth along the *ab* plane is faster than along the *c*-axis, these plates quickly go through the thickness of the film. This is illustrated in Fig. 1.50(*c*), which shows schematically how *c*-axis misaligned grains are nucleated at rough silver interfaces. Any material trapped between growing misaligned plates is prevented from reacting and typically remains in the final film as second phases. Examples of this effect are given in Fig. 1.51(*a–c*), which shows cases when phases containing primarily (Ba,Cu)O, (Ca,Cu)O, and (CaO), respectively, are trapped as a result of this growth at rough interfaces. Growth of such *c*-axis misoriented thereby presents a major hurdle to fabricate highly textured films.

The significant effect of having a smooth interface in obtaining highly textured films is well illustrated in Fig. 1.52(*a* and *b*), which shows results of a 3-μm spray-pyrolyzed film on well-polished silver substrate. Figure 1.52(*a*) compares *c*-axis rocking curves of films on various substrates. Clearly, the film on polished silver has a much sharper rocking curve than a rough silver substrate. Shown also is a typical rocking curve for films on YSZ. Shown on the right in Fig. 1.52(*b*) is a contour map of in-plane orientation of the film on polished silver. Very well developed colonies as large as 5 mm are observed.

Alternate deposition techniques

To obviate the need for mechanical densification of precursor films, two new methods were explored as possible routes. These are:

- Sputtering. Using extremely high deposition rates, precursor films were deposited on silver. The films were found to be very homogeneous chemically. Thallinated films were found to be very flat and well textured and contained a negligible amount of porosities and second phases. Very high J_c's of 5×10^5 A/cm^2 have been obtained at 77 K, 0 T.
- Thermal spraying. Plasma-spraying techniques were used to deposit precursor films at high rates on silver substrates. Initial films were found to be fairly homogeneous and relatively flat. Further optimization is required to form films of higher densities such as those made by sputtering.

EFG 96-6974

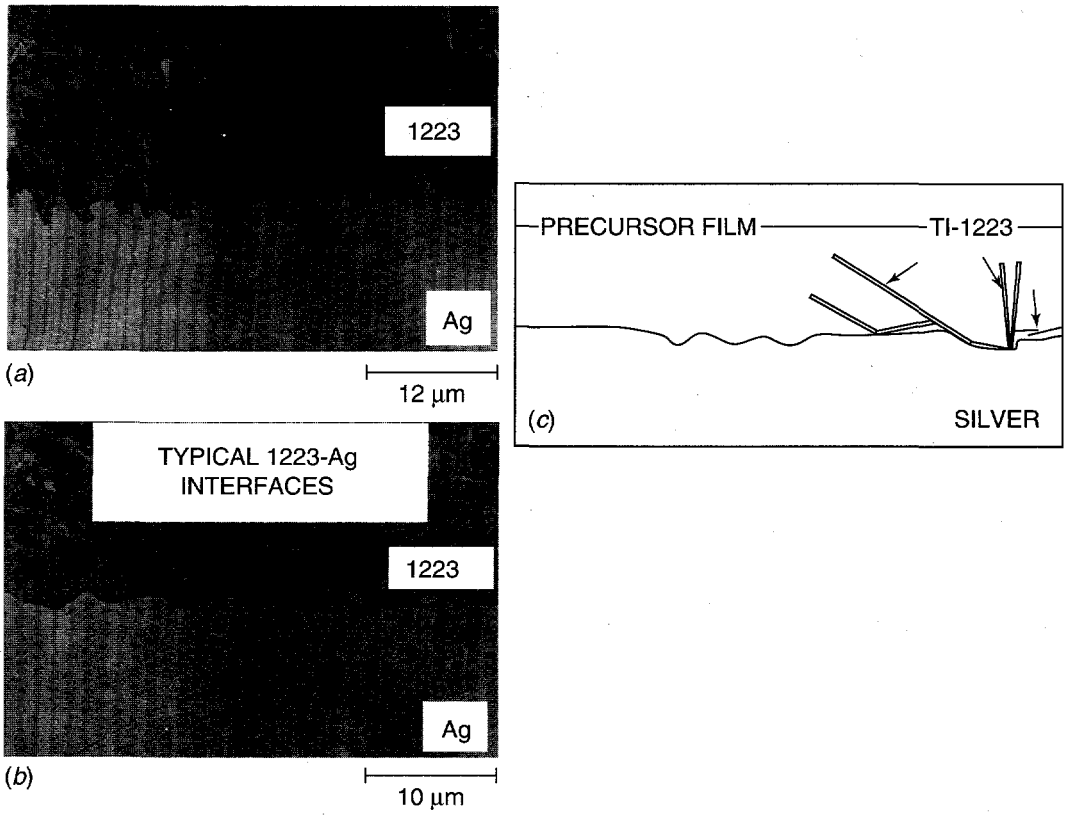

Fig. 1.50. Effect of substrate roughness on texture and phase formation of TI-1223: (*a* and *b*) a rough and a smooth interface with silver; (*c*) nucleation of misaligned grains to form (001) interfaces with silver during crystallization.

EFG 96-6975

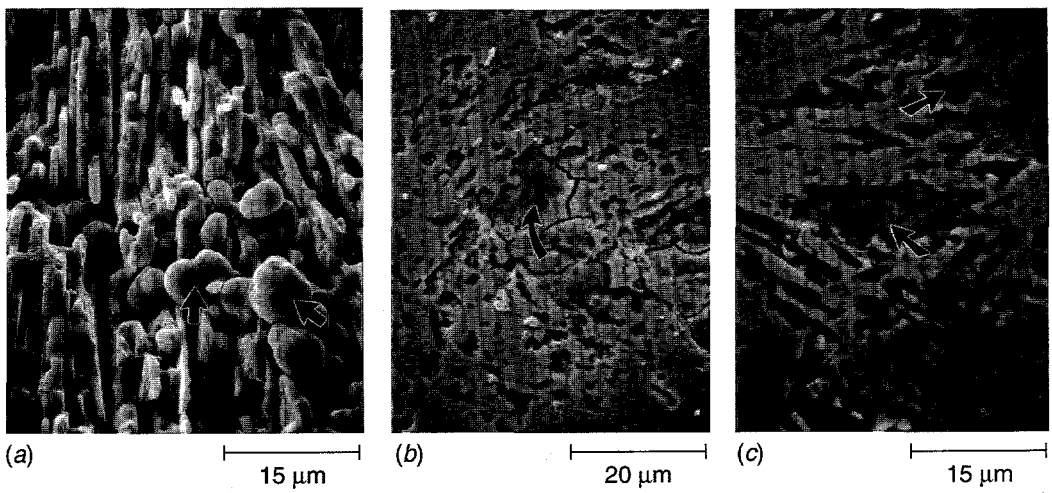

Fig. 1.51. The precursor film is trapped between growing spherulites, resulting in a significant fraction of unreacted material: (*a*) (Ba,Cu)O with some Ca and TI; (*b*) (Ca,Cu)O with large amounts of TI and Ca; (*c*) (CaO) with some Cu, Ba, and a large amount of TI.

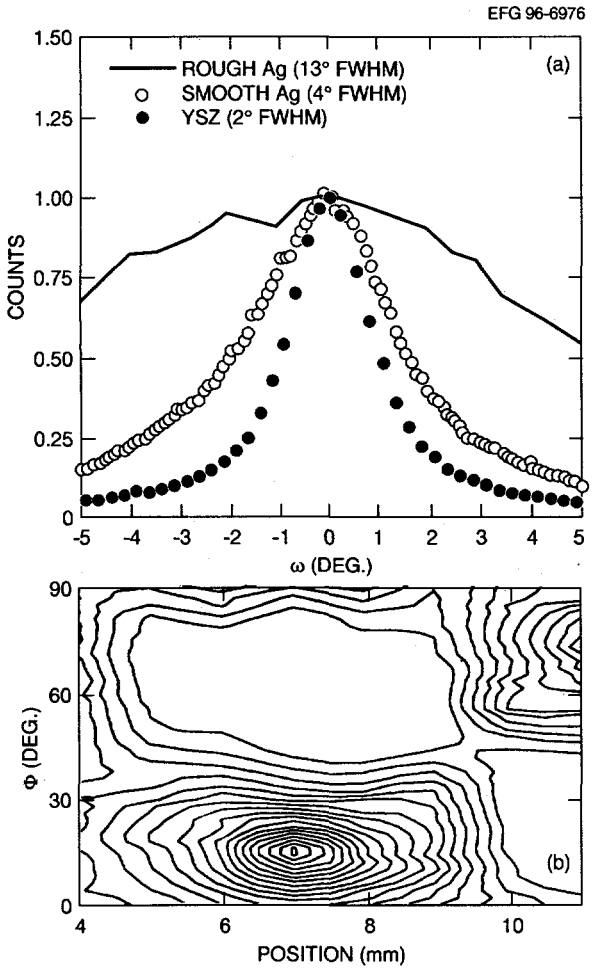

Fig. 1.52. Smooth substrates resulting in well-textured and transformed films with high J_c: (*a*) Tl-1223 (0010) rocking curves correlate with substrate roughness; (*b*) largest colonies observed in spray-prolyzed films on polished silver. J_c (0 T, 77 K) = 65 kA/cm^2; J_c (0.5 T, 77 K) = 10 kA/cm^2.

Artificial flux-pinning centers in Tl-1223

To enhance the irreversibility field in Tl-1223, a new method was explored. Using aerosol powder synthesis in which controlled doping can be performed, inert ceramic oxide particles were introduced into the precursor powders. These powders were used to make films that were subsequently thallinated. Figure 1.53 (*a* and *b*) shows images of dispersed oxide particles. Although no enhancement in transport J_c has so far been obtained in these films, the process looks very promising and further optimization is required.

Limitations to J_c in thick spray-pyrolyzed films

Very thick films (~10 μm) with high J_c are required to meet the industry-stated J_c criterion of 10 A/mm. However, even though high J_c's are readily obtained with 3-μm spray-pyrolyzed films, thicker films result in lower J_c's. To investigate this problem, films with varying thicknesses were received from GE. Figure 1.54(*a*) shows the critical current density of films at various thicknesses and the relative density of the films. At very low thicknesses the densities are low and so is the J_c. However, for films greater than 2 μm, the density of the films is unchanged; the J_c starts to decrease beyond 6 μm.

Figure 1.54(*b*) shows *c*-axis rocking curves for films of various thicknesses. Each rocking curve here appears to be a superimposition of two components: a very well textured component and a weakly textured component. This is well illustrated in Fig. 1.55(*a*), which shows this clearly for 3- and 10-μm films. The 3-μm film has a much larger component of the well-textured region. Figure 1.54(*b*) demonstrates that the weakly textured region increases in fraction as the film gets thicker. In each case, however, the region of the film perhaps at the interface, which is well-textured also, has a well-developed colony structure. This is shown in Figure 1.55(*b*), which shows the most likely *a*-axis grain orientations of the region in the film with a well-developed *c*-axis texture. These observations suggest that perhaps the dominant effect in reducing the J_c of thicker films may be the loss of *c*-axis texture and hence the lesser tendency to form the colony structure that is considered essential to well-linked current flow.

However, growth of highly textured thick films of Tl-1223 is not impossible if one obtains some degree of biaxial texture. This is well illustrated in Figure 1.56(*a* and *b*), which shows structural characterization of a 10-μm film made

EFG 96-6977

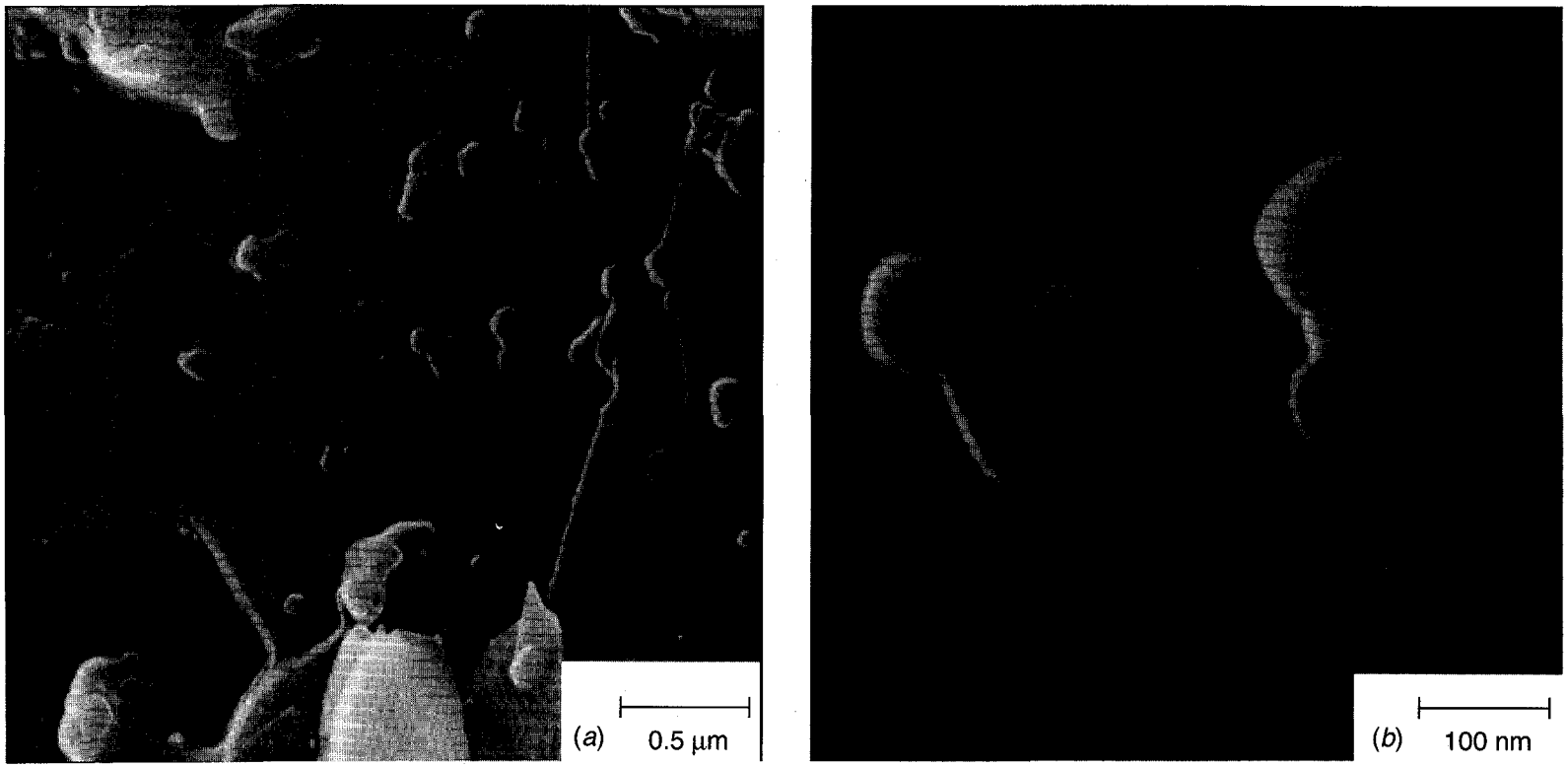

Fig. 1.53. Second-phase particles distributed homogeneously with Tl-1223 grains: (*a*) magnification: 20,000X; (*b*) magnification: 100,000X.

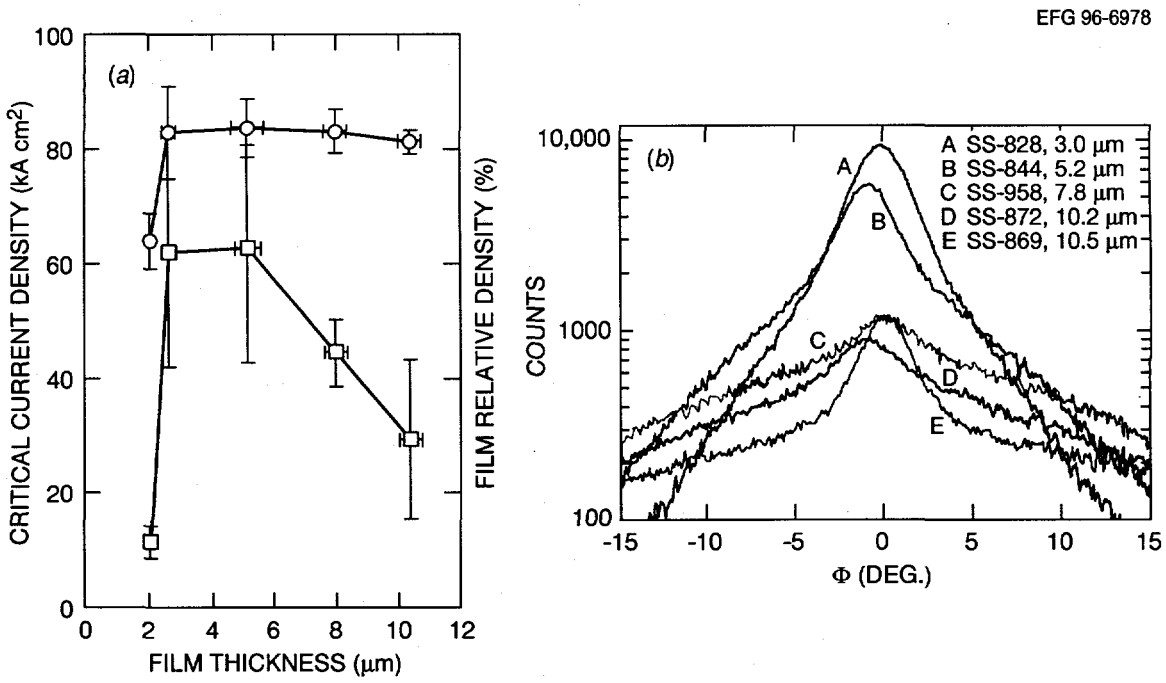

Fig. 1.54. Limitations to J_c in thick spray-pyrolized films (>3 μm): (*a*) critical current density of films at various thicknesses and relative density; (*b*) *c*-axis rocking curves for films of various thicknesses.

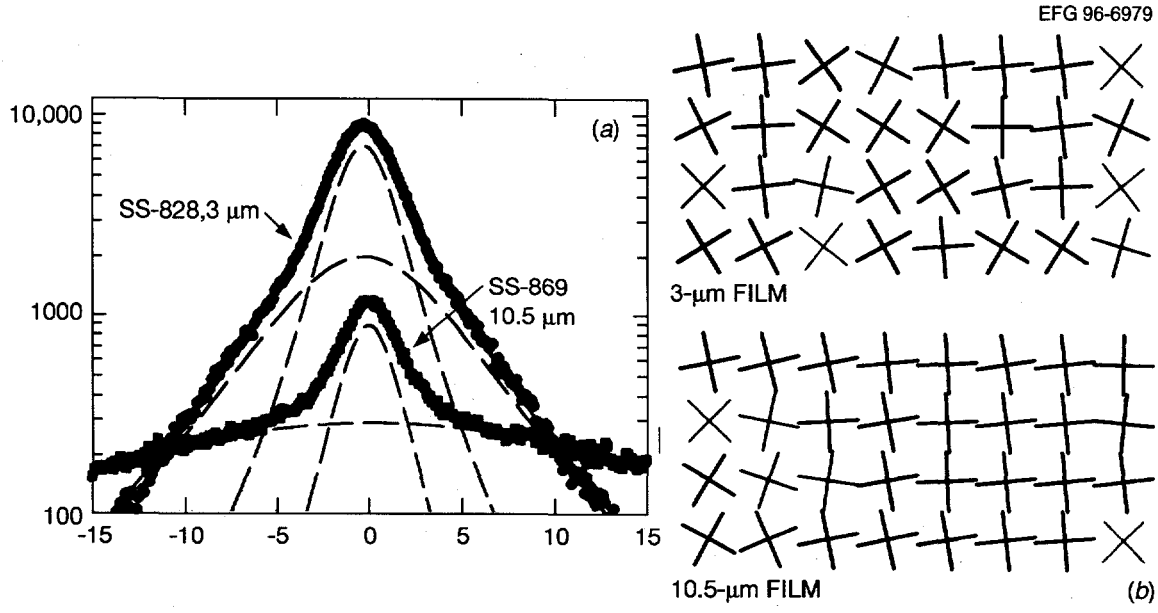

Fig. 1.55. Thicker spray-pyrolyzed films have decreased *c*-axis texture: (*a*) two components of the *c*-axis rocking curve; (*b*) maps of *a*-axis grain orientations.

at the National Renewable Energy Laboratory using the two-zone thallination process on a single crystal of $LaAlO_3$. Figure 1.56(*a*) shows that the film is very well *c*-axis textured with an FWHM of 1.4°. Figure 1.56(*b*) shows a ϕ scan indicating that the film is very well textured in-plane, too, and has an epitaxial relationship with the substrate. This result is significant in two ways: first, it demonstrates for the first time that films as thick as 10 μm can be grown in an epitaxial manner using bulk processing techniques; second, it points to a method when the *c*-axis texture of the film does not deteriorate with increasing thickness. Possible routes to make thick conductors with high J_c that may retain the texture through the thickness include:

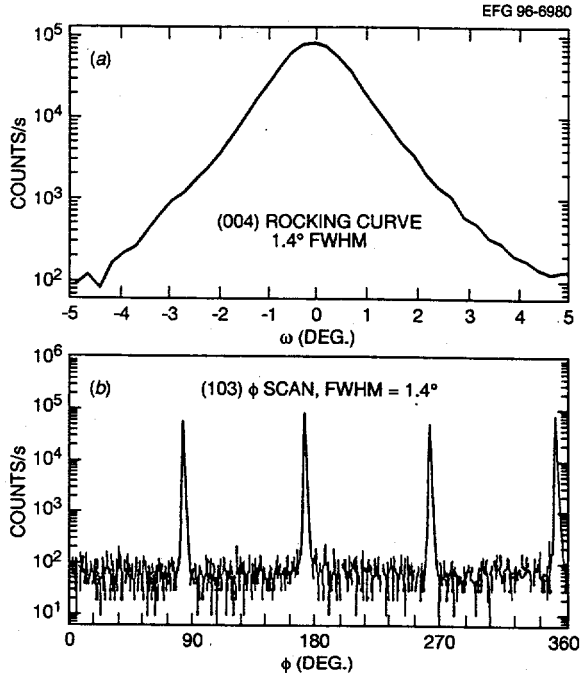

Fig. 1.56. Tl-1223 film grown at the National Renewable Energy Laboratory and characterized at Oak Ridge National Laboratory: (*a*) film has a strong *c*-axis texture; (*b*) film is well textured in-plane and has an epitaxial with the substrate.

- create large colonies with dimensions larger than the thickness of the conductor (however, in such a case, the conductor width may become an important design parameter),
- create some macroscopic biaxial texture between colonies, and
- fabricate biaxially textured films.

REFERENCES

1. M. Murakami et al., *Supercond. Sci. Technol.* **4**, S49 (1991).
2. D. F. Lee, V. Selvamanickam, and K. Salama, *Physica C* **202**, 83 (1992).
3. V. Selvamanickam et al., *IEEE Trans. On Appl. Supercond.* **5**, 1826 (1995).
4. D. M. Kroeger, H. S. Hsu, and J. Brynestad, "Method for Preparation of (Bi-Pb)$_2$Sr$_2$Ca$_2$Cu$_3$ Oxide Powders," U.S. Patent 5,395,821 (1995).
5. M. Sato et al., *Appl. Phys. Lett.* **64**, 640 (1994).
6. Y. Yamade et al., *Physica C* **185–89**, 2483 (1991).
7. M. Cooke and C. Larke, *J. Inst. Metals* **71**, 371, (1945).
8. S. X. Dou et al., *Supercond. Sci. Technol.* **6**, 195 (1993).
9. J. W. Ekin et al., *Appl. Phys. Lett.* **61**, 858 (1992).
10. Dimos et al., *Phys. Rev. B* **41**, 4038 (1990).
11. Hensel et al., *Physica C* **205**, 329 (1993).
12. Cho et al., *Appl. Phys. Lett.* **64**(22), 3030 (1994).
13. Bollman et al., *Crystal Lattices, Interfaces, and Matrices*, 1982.
14. Zhu et al., *J. Mater. Res.* **6**, 2507 (1991).
15. Umezawa et al., *Physica C* **261**, 198 (1992).
16. Bulaevskii et al., *Phys. Rev. B* **48**, 13798 (1993).

17. Tkacyzk et al., *Phys. Rev. B* **45**, 12506 (1992).
18. Caplin et al., paper presented at the Proceedings of the 1994 Applied Superconductivity Conference, Boston, Mass.; to be published in the proceedings.
19. P. Majewski, *Adv. Mater.* **6**, 593 (1994).
20. L. N. Bulaevskii et al., *Phys. Rev. B* **48**, 13798 (1993).
21. A. P. Malozemoff, p. 6 in *Superconductivity and Its Applications*, Vol. 251, ed. Y. H. Kao, A. E. Kaloyeros, and H.S. Kwok, AIP, New York, 1992.
22. L. N. Bulaevskii et al., *Phys. Rev. B* **45**, 2545 (1992).
23. J. H. Cho et al., *Appl. Phys. Lett.* **64**, 3030 (1994).
24. B. Hensel et al., *Physica C* **205**, 329 (1993).
25. B. Hensel, G. Grasso, and R. Flükiger, *Phys. Rev. B* **51**, 15456 (1995).
26. A. Umezawa et al., *Physica C* **219**, 378 (1994).
27. J.-L. Wang et al., *Physica C* **230**, 189 (1994).
28. N. Tomita et al., *Jpn. J. Appl. Phys.* **31**, L942 (1992).
29. S. E. Babcock and D. C. Larbalestier, J. *Phys. Chem. Solids* **55**, 1125 (1994).
30. D. Dimos et al., *Phys. Rev. Lett.* **61**, 219 (1988).
31. D. Dimos, P. Chaudhari, and J. Mannhart, *Phys. Rev. B* **41**, 4038 (1990).
32. E. Sarnelli et al., *Appl. Phys. Lett.* **65**, 362 (1994).
33. T. Nabatame et al., *Appl. Phys. Lett.* **65**, 776 (1994).
34. A. Goyal et al., *Appl. Phys. Lett.* **66**, 2903 (1995).
35. M. F. Sykes, D. S. Gaunt, and M. Glen, *J. Phys.* A **9**, 97 (1976).
36. M. F. Sykes and J. W. Essam, *Phys. Rev.* **133**, A310 (1964).
37. L. R. J. Ford and D. R. Fulkerson, *Flows in Networks*, Princeton Univ. Press, Princeton, N.J., 1962, p. 17.
38. A. Goyal, E. D. Specht, and D. M. Kroeger, to be published.
39. E. D. Specht et al., *Phys. C* **242**, 164 (1995).
40. T. Nabatame et al., *Appl. Phys. Lett.* **65**, 776 (1994).

AN AUTOMATED SYSTEM FOR CURRENT-VOLTAGE CHARACTERIZATION OF CERAMIC SUPERCONDUCTORS

The successful development of an HTS ceramic conductor requires knowledge of the behavior of the conductor's *I-V* characteristics over a range of current, temperature, externally applied magnetic field, and magnetic field orientation. Information of this type is extremely useful both as a practical measure of conductor performance and as a tool to better understand more intrinsic properties of the superconducting material, such as mechanisms for internal dissipation.[1-6] Although many experimental systems for obtaining *I-V* characteristics of HTS have been described in the literature,[7-10] none has an automated capability of providing *I-V* data for a conductor over the ranges of current, temperature, field, and field orientation that are appropriate for thorough conductor characterization. To provide these data can involve considerable operator time and material expense (e.g., liquid helium costs). For this reason, a fully automated, integrated apparatus was designed featuring rapid unattended data acquisition and closed-cycle helium refrigeration.

Description and Capabilities

Figure 2.1 shows a schematic of the apparatus hardware. A conductor sample (~2.5–7.5 cm long) is placed on a copper plate that is in thermal contact with the second stage of a high-output (70 W at 77 K, 16 W at 20 K), two-stage, Gifford-McMahon helium cryostat (CVI CGR511). The high-output cryostat provides rapid cool-down (~45 min) to operating temperatures and is required to overcome the heat load from a pair of 100-A dc, copper current leads. The cryostat is mounted on a copper-wound magnet. It is capable of tilting, which allows measurements to be made in the absence of the effects of the magnet's residual pole face magnetization (~6 mT), and rotating, which enables the orientation of the applied magnetic field with respect to the sample to be varied over a range of 270° with a resolution of ±0.3°.

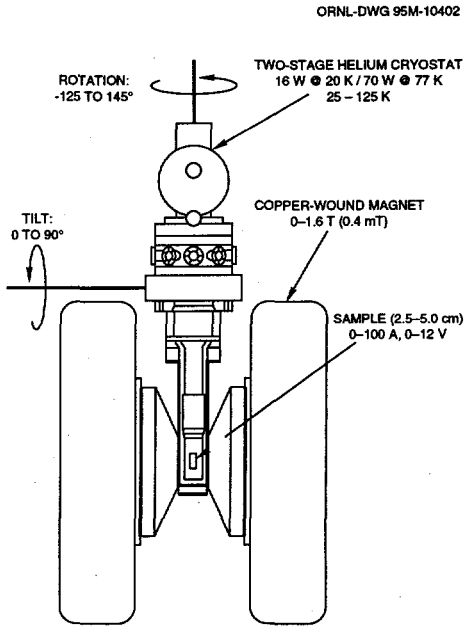

Fig. 2.1. Schematic of the apparatus hardware for measuring *I-V* characteristics.

The magnitude of the externally applied magnetic field is established by the output of a current-controlled power supply and ranges from ~6 mT to 1.6 T in steps of 4 mT. Field strength at the sample is measured with a temperature-compensated Hall probe that is fixed to the back of the copper sample holder within 0.6 cm of the sample's center. Prior to collection of *I-V* data for a particular field strength, the magnet current can be automatically adjusted to attain the desired Hall probe voltage.

The temperature of the sample is monitored and controlled with a ceramic resistance

temperature sensor that is held in direct contact with the center of the sample by a spring-loaded pogo pin and thermal grease. Using a resistance heater imbedded in the copper sample holder, the temperature of the sensor can be maintained to within ±10 mK over the entire temperature range (25–125 K). The thermal response time of the sensor is ~0.2 s.

A block diagram of the pulse electronics is shown in Fig. 2.2(*a*). Data acquisition is accomplished with a board (TransEra 420) that is installed in the back plane of an IBM-compatible PC and that contains a 14-bit digital-to-analog converter (DAC) and a 12-bit analog-to-digital converter (ADC). The DAC and ADC are synchronized using a 4-MHz onboard clock and are both capable of sampling at a rate of 200,000/s; each is equipped with a 512-sample buffer. The DAC is used to program the sample current; the ADC is used to alternately measure the sample current (i.e., voltage across a 1-mΩ series resistor) and the differential sample voltage.

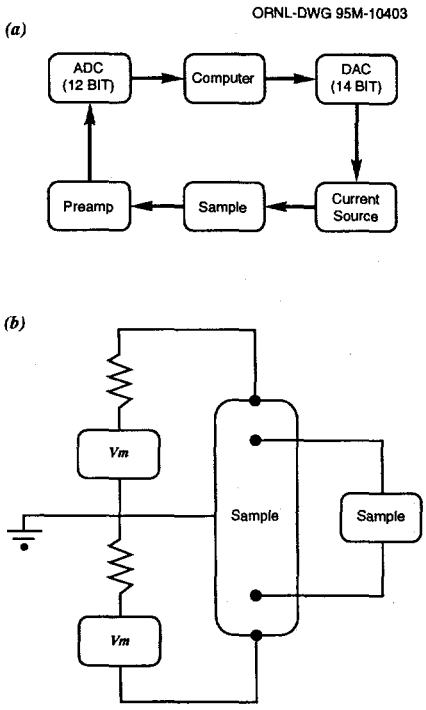

Fig. 2.2. Schematic of the apparatus electronics for measuring *I-V* characteristics: (*a*) block diagram of the pulse electronics and (*b*) details of the power supply interconnections.

Application of Current

Current is provided to the sample by a pair of 0.64-cm-diam copper leads. The leads are thermally linked to the 77-K first stage of the cryostat by a pair of 40-cm^2 copper plates that are electrically isolated with 2.5-μm-thick Mylar. Four 0.5-mm-thick sapphire sheets (~2 cm^2 each) establish a thermal linkage between the copper current leads and the copper sample plate. Indium pressure contacts establish an electrical linkage between the current leads and the sample. Voltage is measured across a 1-cm length of the sample with gold-coated pogo pins.

Currents of up to 100 A are applied to the sample either continuously or as pulses (2–100 ms duration) by a pair of high-speed (~50-μs rise time) power supplies (Kepco ATE6-100) that are connected in series [Fig. 2.2(*b*)]. One supply (*Vm*) is voltage-programmed by the DAC to control the sample current; the other supply (*Vs*) is configured to follow the voltage of *Vm*. For pulsed measurements the gain of *Vs* relative to *Vm* is adjusted to reduce the common mode voltage on the voltage probes. This adjustment effectively establishes the center of the sample at ground potential throughout a pulse. A common mode voltage can arise from an imbalance in the resistances of either the current leads or the current contacts to the sample and results in errors in the measurement of the differential sample voltage. Because the common mode rejection ratio of the preamplifier (PAR 5113) decreases with increasing frequency, adjustments of power supply gain are more important for pulses of short duration.

Figure 2.3(*a*) shows the time response of the system to a 3.5-ms square pulse from the DAC. To correct data for signal background, data is obtained before and during the application of current. The sample current follows the square DAC pulse with an ~50-μs time constant. The sample voltage seen by the ADC through the preamplifier (0.33-ms time constant) exhibits a significant overshoot at the leading edge of the current pulse; this can lead to electronic overloads. The magnitude of the overshoot

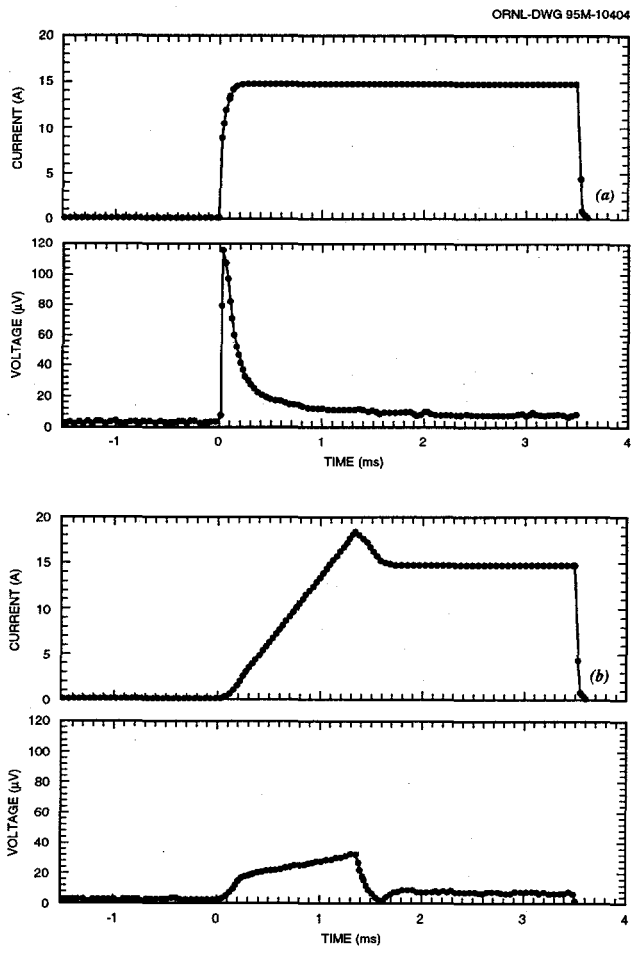

Fig. 2.3. Typical time profiles of current and voltage: (*a*) 3.5-ms square pulse and (*b*) 3.5-ms programmed ramp with overshoot.

increases with an increase in the amplitude of the square current pulse, suggesting the existence of an inductive coupling between the voltage and current leads.

Inductive pickup on the voltage leads can be reduced either by modifying the geometry of the *I-V* leads (e.g., twisting lead pairs) or by reducing the time derivative of current. Because design constraints place severe restrictions on modifying the particular lead geometry of this system, pulse shaping has been considered as a means to reduce the magnitude of inductive pickup. Figure 2.3(*b*) shows the response of the system to a 3.5-ms pulse with a programmed ramp up, overshoot, and ramp down. Compared with the square pulse, the ramped pulse results in much less overshoot in sample voltage. Tailoring the current pulse shape and duration has been implemented with this apparatus to optimize the system response.

A typical experiment to obtain *I-V* characteristics of a conductor involves several temperatures, magnetic fields, and field orientations. For fixed temperature, field, and orientation, an *I-V* curve of ~20–50 points is obtained in ~5–10 min. For each *I-V* point, current pulses of a particular amplitude are repetitively applied to the sample and averaged until a specified statistical significance of sample voltage (generally ±0.5 μv) is obtained. The sample voltage is determined from that portion of the pulse for which time-dependent transients have decayed. The duty cycle for pulsing (i.e., percent of time during repetitive pulsing that the current is on) is adjustable between ~0.01 and 10% to avoid cumulative sample heating caused by a finite contact resistance. During data acquisition the averaged current and voltage pulses for each *I-V* point are displayed to help identify problems of sample heating.[11] Such problems can usually be solved by reducing the duty cycle or duration of the pulse.

Points on an *I-V* curve can be spaced either equally or exponentially in current. Exponential spacing usually results in more rapid acquisition of data and more precise determinations of I_c. To further reduce data acquisition time, points are initially spaced coarsely as current is increased from zero until a prespecified sample voltage is exceeded; then a finer spacing of points is used.

Results

Figure 2.4 shows a portion of the *I-V* characteristics obtained for a $Bi_2Sr_2Ca_1Cu_2O_x$ HTS deposit on silver. The data shown were recorded in ~4 h without operator attention. Using a 1-μV/cm criterion, transport critical currents were obtained for these data (Fig. 2.5). The dependence of I_c on H and T [Fig. 2.5(*a*)

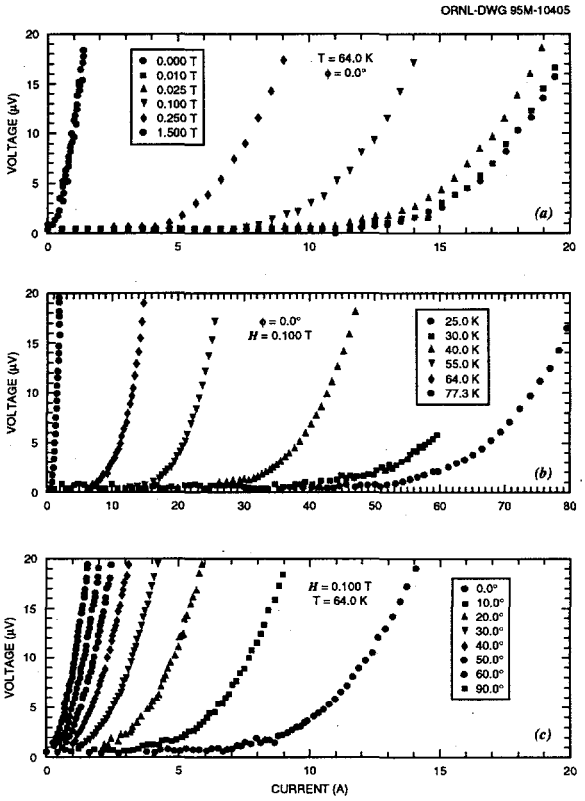

Fig. 2.4. *I-V* characteristics obtained for a $Bi_2Sr_2Ca_1Cu_2O_x$ high-temperature superconducting deposit on a silver tape: (*a*) variable applied magnetic field for fixed temperature and fixed orientation, (*b*) variable temperature for fixed orientation and fixed applied magnetic field, and (*c*) variable orientation for fixed applied magnetic field and fixed temperature. The applied field, *H*, is in all cases perpendicular to the direction of current flow; ϕ = 0° is for *H* perpendicular to the tape surface normal, and ϕ = 90° is for *H* parallel to the tape surface normal.

and (*b*)] is typical of bismuth-based oxide superconductors and is consistent with dissipation arising from flux creep with small pinning potential.[12,13] Dependence of I_c on the orientation of the applied magnetic field [Fig. 2.5(*c*)] reflects the intrinsically anisotropic properties of $Bi_2Sr_2Ca_1Cu_2O_x$ and the crystallographic texture of the oxide deposit.

Conclusions

Data of this type are obviously valuable for evaluating conductor performance under field and temperature conditions specific to a particular application (e.g., motor windings, power transmission lines, and transformer windings). Both application design and conductor development are facilitated by the rapid, automated characterization that this apparatus provides. Control of current, temperature, magnetic field, and field orientation is fully automated and requires no user interaction. Automation and closed-cycle helium refrigeration together provide extremely cost-effective operation.

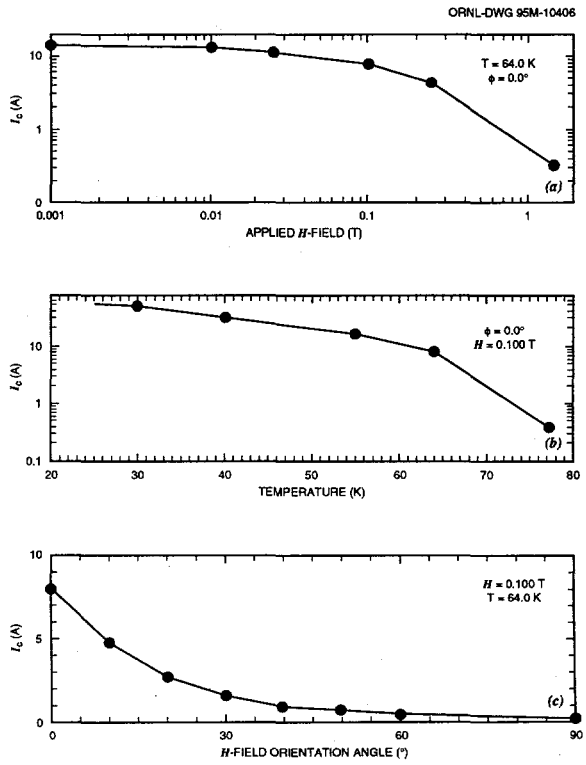

Fig. 2.5. Transport critical current (I_c) obtained for data in Fig. 2.4 using a 1-μV/cm criterion.

AC WIRES AND COILS FOR POWER APPLICATIONS

Development of HTS AC Conductors

In continuing theoretical studies on ac losses in HTS tapes, ASC has developed models to guide ac conductor development, notably the second generation ac conductor. By the same token, ORNL recently developed a complementary calorimetric ac loss measurement apparatus, and systematic ac loss measurements were performed on the ac conductors. ASC provided valuable guidance to ORNL to enhance the sensitivity of ORNL's instrumentation.

Analysis of the previously measured high-ac-loss HTS tapes showed that such losses could be due to one or both of the following: filaments are effectively bridged together under the applied ac field; ac field components are perpendicular to the broad face of the tape. The loss with perpendicular ac field was found to depend on the square of the width to the thickness ratio of the tape. These findings have guided ASC in further development of ac conductors.

ASC successfully developed ac conductors with 8, 16, and 85 twisted filaments of Bi-2223, some of which had a high-resistivity matrix. Photomicrographs of the conductor showed that the lower filament count ones were clearly unbridged. Small test coils were fabricated out of these conductors for ac loss measurements.

Following the lead of ORNL, ASC also developed a complementary calorimetric ac loss measurement apparatus. This was accomplished by enclosing the superconducting sample, along with a calibration heater and a thermometer, inside a G-10 thermal isolation cylinder. The temperature rise of the conductor due to ac loss is compared with the calibration heater power. The apparatus at ASC uses an HTS coil to supply the ac field. It can measure ac loss in liquid helium or liquid nitrogen. Field amplitude of up to 0.15 T and 10–60 Hz is available in this facility. The apparatus at ORNL uses a room temperature coil outside a variable temperature cryostat to supply the ac field. Temperatures ranging from 4.2 to 100 K can be used for the measurements. Field amplitude of up to 0.1 T and 40–500 Hz is available in this facility. The sensitivities of these apparatus were found to be 1 mW/cm^3 at 77 K and 5 μW/cm^3 at 4.2 K.

Using both the facilities at ASC and at ORNL, sample coils of the ac conductors were measured for their ac losses. The ac loss data were carefully correlated to the various material properties of the conductor such as twisting, bridging, aspect ratio, and matrix resistivity. Figure 2.6 shows an example of the loss result when the sample was subjected to ac fields perpendicular to the broad face of the tape. For the 16-filament twisted conductor, the filament became effectively coupled (as in the case of the untwisted conductor) at field magnitude greater than 25 mT, which was consistent with the

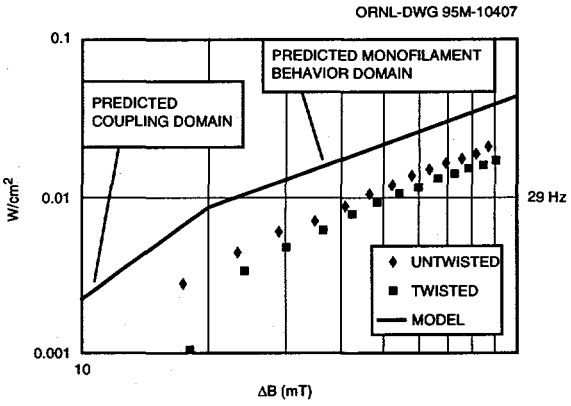

Fig. 2.6. Losses (ac) of 16-filament conductors in 29-Hz ac fields perpendicular to the broad face of the tape.

theoretical prediction. Figure 2.7 shows the comparison of eight-filament twisted and untwisted conductors with 75-mT ac field parallel to the broad face of the tape in power frequency range. Reduced loss of ~2 mW/cm^3 was obtained for the twisted-filament conductor.

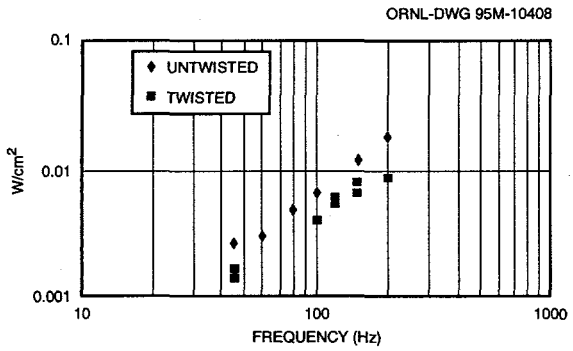

Fig. 2.7. Losses (ac) of eight-filament conductors in 75-mT ac fields parallel to the broad face of the tape.

Quench Behavior of HTS Tape and Coil

Stability and normal zone propagation experiments were performed on a single-length and a double-pancake coil made of Bi-2223/silver HTS tape. Experiments were conducted with liquid nitrogen and gaseous helium cooling at 5–77 K. No distinctive normal zone propagation was observed in the single-length conductor tests. Nonuniform critical currents were observed, however, over the length of the conductor. To dramatize the effect on the stability of a magnet wound with this kind of nonuniform conductor, a pancake coil was wound with conductors composed of a two-tape bundle on the inner turns and a single-tape bundle on the outer turns.

Figure 2.8(*a*) shows the coil current and voltage traces for a run of holding the current constant for a long time at 6 K. The coil was charged to 50 A in about 210 s and held at that value. Little coil voltage change was seen for the next 160 s. Then the voltage increased rapidly and reached a level of ~5.5 V in another 15 s. The coil current dropped to ~20 A at the same time. No operator action was taken during this period. The coil quenched, and its voltage rise was limited only by the power supply compliance limitation of 6 V. Manual discharge of the coil was finally implemented at 530 s.

Figure 2.8(*b*) shows the thermometer readings of the coil for the same run. A small and steady temperature rise (~ 0.15 K/s) was seen on both thermometers after the current reached 50 A. Only a very small temperature difference was seen between the ID and the grading point of the coil. The temperature at the grading point, T_1, was about 8 K higher than that at ID, T_0, by 370 s, the time at which the coil voltage began to rise sharply. The average coil temperature was about 35 K then. At this time the coil temperature also began to rise sharply. Thus, we saw a gradual temperature rise followed by a rapid voltage and temperature rise of the coil when it quenched.

Similar delayed quench behavior at a fixed current was observed at other test runs with coil starting temperatures of 20–77 K. Thus, we observed coil quenches without a distinctive "normal" front propagation or a large temperature gradient.

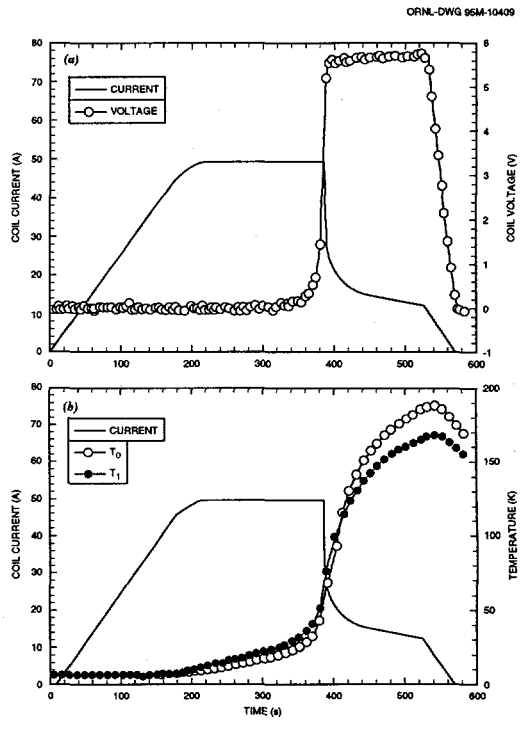

Fig. 2.8. Coil current, voltage, and temperature traces of a current charge that was held, starting at a coil temperature of 6 K. Thermometer T_0 was located at the ID of the coil, and T_1 was located at the grading point.

The objective of this project was to develop the technology needed to produce HTS coils for electric power applications in ac mode. In this cooperative agreement between ASC and ORNL, substantial progress toward this end was achieved in two areas: (1) the milestone of producing ac loss measurements in a high-resistivity matrix, twisted-filament, HTS pancake coil was completed, and (2) quench behavior of HTS tape and pancake coil was measured and its nature (which is different from that of a low-temperature superconductor) was analyzed.

SUPERCONDUCTING TRANSFORMER PROJECT

The initial objectives of the Superconducting Transformer Project were (1) evaluation of markets, technical and economic feasibility, and benefits to society of HTS power transformers of medium (30 MVA) to a large rating; (2) development of a low-cost, wind-after-react HTS conductor suitable for use in transformers and in other ac apparatus; and (3) design, construction, and testing of an ~1-MVA, single-phase HTS demonstration transformer. Significant progress in the first two objectives resulted in the decision to continue into the demonstration phase. Organizations participating in the project are ORNL, IGC, Waukesha Electric Systems, Rochester Gas and Electric Company, and key university consultants. Rensselaer Polytechnic Institute provides consulting under subcontract to IGC.

Design Choices

Several design choices were examined; specific details, however, are proprietary. Sizes from 10–50 MVA operating at a nominal 138 kV were evaluated. The design approach was calculated from input values for the transformer specifications, the cost and properties of an HTS conductor, and other factors such as core losses, transformer capital cost, and total owning cost (TOC). In many cases we examined the transformer TOC, capital cost, dimensions, and total weight. The following design issues were resolved by this analysis:

- instantaneous fault recovery from 10× fault current;
- low-cost, reliable refrigeration;
- 550-kV basic insulation level to withstand lightning;
- use of low-cost, near-term conductors;
- utility systems compatible reactance;
- low-loss leads and bushings;
- loss-reducing winding designs;
- low dielectric losses;
- reduced weight and size;
- low capital cost; and
- substantially lower TOC.

From these studies, two basic designs will be more closely evaluated: Design I is an open cycle, liquid nitrogen–cooled unit; Design II, a closed cycle, cryogen-free unit. The net results of this analysis are summarized in Figure 2.9. These technical and economic evaluations and market analysis led to the selection of an 18-, 24-, or 30-MVA, three-phase, 138–13.8 kV design as a base reference design. This design size is the "dead center" of the small power transformer market (see Table 2.1). In addition, literature review and analysis by Rensselaer Polytechnic Institute and ORNL established that, for the dielectric systems chosen, performance was probably acceptable if the intergap region were subdivided with appropriate solid dielectric materials. This follows standard design practice in both oil-filled and dry transformer design.

ORNL-DWG 95M-10410

LOSS EVALUATION FACTORS ($/kW)			
A =	$2,500		
B =	$430		
	COST ($K)		
YEAR	DESIGN I	DESIGN II	CONVENT.
1995	$2,615	$430	$250
2000	$230	$255	$250
2005	$195	$240	$250
	NORMALIZED		
	COST ($K)		
YEAR	DESIGN I	DESIGN II	CONVENT.
1995	10.46	1.72	1.00
2000	0.92	1.02	1.00
2005	0.78	0.96	1.00

	LOSES (kW)		
	CORE	I^2R	REFRIG.
CONVENT.	14.3	158.7	0
DESIGN I	14	0	12.1
DESIGN II	14	0	30

	TOC ($K)		
YEAR	DESIGN I	DESIGN II	CONVENT.
1995	$2,680	$540	$354
2000	$295	$365	$354
2005	$260	$350	$354

	NORMALIZED TOC ($K)		
YEAR	DESIGN I	DESIGN II	CONVENT.
1995	7.57	1.53	1.00
2000	0.83	1.03	1.00
2005	0.74	0.99	1.00

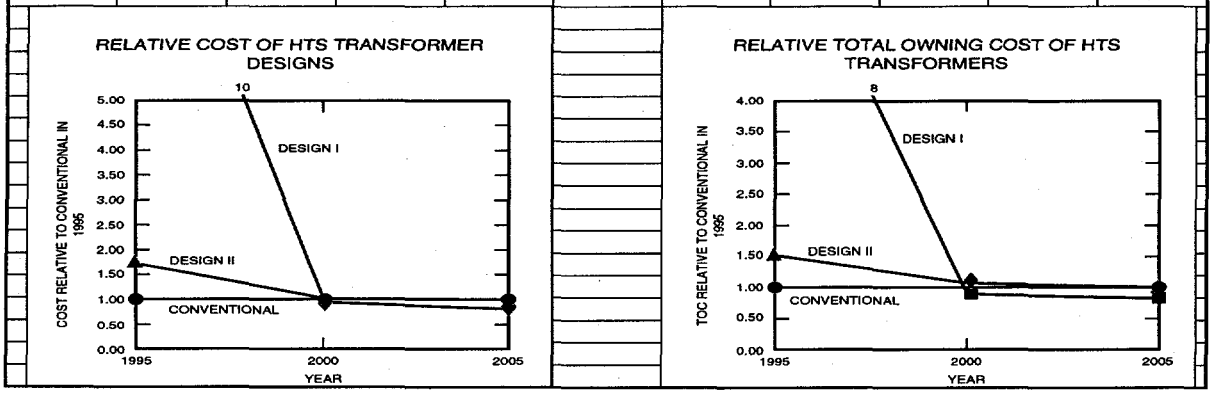

Fig. 2.9. Cost comparison: Design I, Design II, and conventional transformer.

Table 2.1. Power transformer market in the United States[a]

	10–100 MVA	>100 MVA
Units	874	78
Total MVA	33,000	26,000
Total value	$260M	$109M

[a]World growth rate would be about double that of the U.S. market, and the above data would be about four-fold.

Transport Property Measurements and Conductor Coatings

Transport property measurements of candidate conductors for HTS transformers were determined in concert with IGC. IGC provided short lengths [~5 cm (~2 in.)] of surface-coated Bi-2212/silver conductors to ORNL for characterization. The critical current (I_c) of eight of these conductors was determined for a temperature range (25–77 K), an applied magnetic field (0–1.5 T), and field orientation (−90 to +90°). At 25 K and $H = 0$ T, conductors showed I_c's of from ~20 to >100 A. These values of I_c decreased from ~2 to 10 A at 77 K and zero field. Several commercially available epoxy coatings were evaluated for effectiveness in providing protection of Bi-2212 surface-coated silver conductors from environmental degradation. Protection of the conductor appears to be acceptable. Details of behavior with field orientation and magnitude are proprietary.

Cryogenics and Refrigeration

In Design 1, the windings would be cooled using an open cycle, liquid nitrogen–cooled system. The main advantage of this

configuration is simplicity, particularly if liquid nitrogen is also used as part of the dielectric system. In Design II a closed cycle, cryogen-free configuration would use force-cooled windings. The windings themselves would thus enclose the coolant, but a separate compressor would be needed to circulate coolant through them.

Two main questions must be answered in choosing the refrigeration system: How will the cooling source be provided? How will this cooling be transferred to the windings and heat shields? Because the power consumed by the refrigerator depends strongly on the operating temperature, values near 77 K are desirable. At this temperature, a separate actively cooled thermal shield may not be needed. However, high temperature increases the superconductor cost, since more conductor is required to compensate for the reduced operating current density. Clearly, the two design configurations chosen address this issue in significantly different manners. While the best choice will be determined, preliminary results do not provide a clear-cut winner.

AC Losses

Direct measurements of ac losses for the proposed conductors' controlled field are yet to be done. Preliminary estimates, made by IGC and based on a model by Wilson, were checked by ORNL and appeared reasonable. Direct measurements using the calorimetric method should provide reasonable engineering data if an acceptable test configuration can be placed in the measurement apparatus. IGC has suggested a scaleable measurement that closely simulates transformer conditions. ORNL will conduct these loss measurements with the test configuration supplied by IGC.

SUPERCONDUCTIVITY PARTNERSHIP INITIATIVE: ROTOR INSTRUMENTATION FOR 100-MVA GENERATOR

The rotor of a superconducting generator contains the superconducting field windings, support structure, heat shields, vacuum insulation, torque tubes, heat exchangers, and rotating couplings to bring cold helium gas and/or liquid in and out; it is therefore much more complex than a conventional generator rotor. Particularly for early test models, instrumentation must be provided inside the rotor to assess its performance and to protect it from damage. To prove superconducting generator reliability under varying operating conditions, long-term tests are required. Thus, a rugged and durable system must be developed to transfer signals from sensors installed in the rapidly spinning rotor out to a stationary data collection system. The parameters to be measured include temperature, strain, and magnetic field. Small resistive voltages on the field winding are of interest but would be difficult to measure in the presence of the much larger inductive voltages used to control the field. Winding current, coolant flow, and pressure are also of interest but can be measured in the stationary frame.

The most direct and obvious way to transfer signals across the rotating interface would be by brushes and slip rings. However, GE has had poor experience with frost buildup and excessive wear on slip rings on the earlier 20-MVA superconducting generator project. The wear problem makes a noncontact method of transferring the signals preferable. Earlier, GE has been interested in previous work at ORNL to develop an optical system using laser-induced fluorescence of certain phosphors for remote cryogenic thermometry. ORNL agreed to carry out further evaluation on this approach and to continue looking at other methods such as electronic telemetry.

Laser-Induced Fluorescence

Laser-induced fluorescence is a versatile technique for measuring properties at a solid surface. Using a clear epoxy binder, a powdered phosphor is applied to the surface of interest. A pair of optical fibers bring in UV laser light to excite the phosphor and to return emitted light to

a monochromator and photomultiplier tube. The photomultiplier tube signal is applied to a digital storage oscilloscope that in turn downloads the data to a computer. Following the UV excitation pulse, the phosphor emits light in a discrete spectrum that is sensitive to various conditions at the phosphor surface. Because the fibers do not have to touch the surface, remote noncontact monitoring of the surface is possible.

Methods of measuring temperature, magnetic field, and strain were discussed. The concensus was that a single phosphor could give both temperature and magnetic field information by measuring the decay time and Zeeman splitting of certain spectral lines in the phosphor La_2O_2S doped with europium. If terbium were added, strain information could also be extracted.

The preferred configuration would be to bring the optical fibers in radially through the stator cooling ducts and couple to the phosphors with quartz windows in the rotor EM shield. Fig. 2.10 shows possible arrangements of the phosphor at various locations in the rotor. In the figure, the system is just starting to look at a phosphor spot in the Inconel shield (a quartz window is not really needed here because it is outside the vacuum envelope). Clockwise from this location, there are windows to the outer heat shield, outer torque tube, field winding, inner heat shield, and inner torque tube. Different locations are accessed by changing the laser pulse timing. The estimated cost of the system hardware (not including the data acquisition computer) is ~$14,000, of which $5000 is the laser cost. The phosphor cost is negligible; so the incremental cost per channel is basically the cost of a quartz window, ~$200.

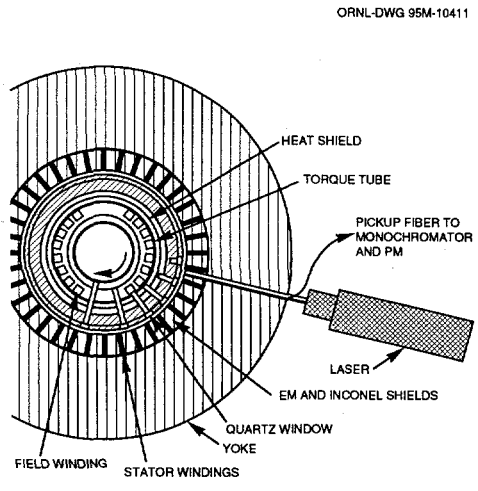

2.10. Laser-Induced Fluorescence System installed in superconducting generator.

Fiber-optic Transmission

Fiber-optic transmission systems are widely used in utility, industrial, and communications applications. A transmitter on the rotor contains an A/D convertor and LED circuit to convert electrical sensor signals to light pulses. The optical fibers from the various channels would be brought to an "optical slip ring" assembly. This would probably be a series of lucite rings surrounding the shaft. Each fiber would point radially outward into a ring, which would carry its light to a fiber from a fixed receiver unit. The light intensity would be modulated because of the changing optical path length through the lucite as the shaft rotates, but this should not compromise the D/A conversion in the receiver as long as digital "0" and "1" can be distinguished reliably. Experiments have shown that such a device is feasible. The response time of the modules is 0.5 s.

The modules cost only ~$470 for each transmitter-receiver pair; so individual channels can be used on each sensor without multiplexing. The transmitters are ~13 cm (5 in.) long and weigh ~0.45 kg (1 lb). They are not made for high-g force rotating environments and would likely have to be internally potted with epoxy. Care would be needed to achieve a well-balanced transmitter assembly. Furthermore, power for the transmitters and sensor excitation would have to come from batteries on the rotor or a rotating transformer. The units can be supplied ready for 14- to 18-V ac power. Although we have not found a commercial fiber-optic transmission system for

rotating equipment, adaptation of the available stationary equipment appears straightforward.

Electronic Telemetry Systems

In conjunction with their 300-MVA superconducting generator program, Westinghouse Electric Corporation performed extensive investigations into data telemetry from rotating cryogenic systems in the early 1980s. To see what changes had occurred since they had looked at the commercial telemetry equipment, ORNL staff searched the *Thomas Register* for currently offered systems. The only system that appeared to be adequate was offered by Wireless Data Corporation (WDC). The analog signal from a sensor is used to frequency-modulate an FM-band carrier signal. A shaft-mounted transmitter sends this signal to a stationary loop antenna that encircles the shaft. The stationary electronics module recovers the sensor signal in much the same way as in an FM radio receiver. The sensors and shaft-mounted electronics can be either battery- or induction-powered. The transmitters are very rugged and can withstand 15,000–30,000 g in various models.

In principle, a system could be put together to handle any kind of sensor with a voltage output. However, nonstandard sensors have special excitation needs and may have to be impedance-matched to the transmitter input; thus, it is advisable to have the factory carry out any needed modifications. Manufacturer data sheets for several sensors that appear appropriate are included in our report to GE. WDC offers several complete turnkey systems for different applications. A six-channel multiplex system with 100-Hz frequency response is available.

Recommendations

The WDC telemetry system has the advantage of immediate commercial availability and would be the best choice for the rotating cryogenic test stand and generator protype. GE recently ordered two six-channel multiplex systems from WDC for their rotating test cryostat. The laser-induced fluorescence system shows great promise but has so far had only an engineering demonstration for temperature measurement. It has the advantage of requiring no electronics on board the rotor. With further development and hopefully commercialization, it may well be less expensive than the telemetry system because the incremental cost per channel is low, and it could be a better choice for production units. Fiber-optic transmission systems also show promise but require commercial development of the rotating interface and perhaps structural modifications to the transmitter modules for vibration and high-g forces. An Appendix to the report to GE gives manufacturer data on all major equipment needed for each system investigated.

REFERENCES

1. J. Bardeen and M. J. Stephen, *Phys. Rev.* **140**, 1197 (1965).
2. Y. B. Kim, C. F. Hempstead, and A. R. Strnad, *Phys. Rev.* **139**, 1163 (1965).
3. P. W. Anderson, *Phys. Rev. Lett.* **9**, 309 (1962).
4. M. V. Feigel'man et al., *Phys. Rev. Lett.* **63**, 2303 (1989).
5. V. M. Vinokur, P. H. Kes, and A. E. Koshelev, *Physica C* **168**, 29 (1990).
6. M. P. A. Fisher, *Phys. Rev. Lett.* **62**, 1415 (1989).
7. M. Nilsson-Mellbin, A. Parikh, and K. Salama, *Physica C* **223**, 19 (1994).
8. T. R. Askew et al., *J. Mater. Res.* **6**, 1135 (1991).
9. L. Kirkup, W. Kalceff, and G. Stockton, *Rev. Sci. Instrum.* **63**, 2044 (1992).
10. M. N. Kunchur, D. K. Christen, and J. M. Phillips, *Phys. Rev. Lett.* **70**, 998 (1993).
11. T. R. Askew et al, *IEEE Trans. Appl. Supercond.* **3**, 1398 (1993).
12. N. Savvides, *Physica C* **165**, 371 (1990).
13. J. W. C. DeVries, G. M. Stollman, and M. A. M. Gijs, *Physica C* **157**, 406 (1989).

Summary of Technology Partnership Activities

BACKGROUND

ORNL is a key part of DOE's national effort on electric power applications of HTS. ORNL has formed effective teams that combine the resources of the Laboratory with the entrepreneurial drive of private companies. New technology transfer methods, a feature of the ORNL Superconducting Technology Program for Electric Power Systems since its inception in 1988, have resulted in 32 superconductivity "pilot center" cooperative agreements and 2 cooperative research and development agreements (CRADAs). In addition, licensing agreements, joint inventions, and joint publications with the private industry partners have ensured that there is technology transfer throughout the program.

Technology partnering on Laboratory-industry teams may occur in several ways. Spinoff technology partnering involves the licensing of patentable Laboratory inventions to industry, continued product or process development to the point of demonstration of commercial viability, or both. Licensing of Laboratory spinoff technologies is how spectator firms can participate in this national program. However, this type of technology partnering is the traditional one-way variety in which the Laboratory invents and private industry applies. In the ORNL program the cooperative development level of technology partnering is emphasized: joint industry-Laboratory teams work on a problem that (1) requires combined resources and expertise and (2) has a clear objective of industrial commercialization. For the project to succeed, each partner depends on the success of the other.

Most of the cooperative projects with private industry and the Laboratory precompetitive research and development projects are developing key technology in which commercialization of the results is expected to occur after a minimum of 3–5 years. Some activities are also of a higher-risk, longer-term nature for which new markets, or a shift of markets, to embrace HTS are expected if the project succeeds. For example, the ORNL RABiTS™ process represents a new way to produce strongly linked YBCO wires using an industry-scaleable process. This wire may still be the only option for practical performance levels in high magnetic fields at temperatures greater than 77 K.

RELATIONSHIP TO THE DOE MISSION

The ORNL program mission is that of its program sponsor, DOE's Office of Utility Technologies, Superconductivity Program: to develop the technology base necessary for industry to proceed to commercialization of electric energy applications of HTS. HTS will enable new energy-efficient motors, transformers, and transmission lines and will also provide electric power equipment manufacturers with strategic technology for global competitiveness. Electric utilities can defer acquisition of new transmission rights-of-way with successful introduction of superconducting cables. System stability and protection will be enhanced with the introduction of fault current limiters. Distributed utility systems in the future, which will include distributed generation systems, will benefit from the small size and weight of the next generation of electric power equipment.

FUNDING

DOE funding for the program, subcontracting activities in 1995, and a summary of funds-out cooperative agreements are shown in Tables 3.1 and 3.2 and in Fig. 3.1.

Table 3.1. Superconducting Technology Program funding: authorization and outlay by fiscal year

	New budget authorization/outlay ($ × 1000)				
	1989–1991	1992	1993	1994	1995
Direct scientific and technical[a]	5218	3213	3511	3334	3434
Management and outreach	449	280	294	298	300
Subtotal	5667	3493	3805	3632	3734
Subcontracts[b]	154	439	428	496	198
Funds-out cooperative agreements	1749	1072	867	821	611
Total program	7570	5004	5100	4949	4543

[a]See Fig. 3.1 for distribution of funding for Oak Ridge National Laboratory.
[b]Details are provided in separate tables. Funds-out cooperative agreements provide direct financial support to U.S. industry for cost-shared cooperative research and development.

TECHNOLOGY PARTNERSHIP APPROACH

Our interdisciplinary approach uses all resources available at ORNL to meet the program goals for joint industry-Laboratory development of HTS technology for electric power applications. Our superconductivity agreement mechanism interlinks research and development projects with industry and universities that optimize utilization of facilities, expertise, and program resources for the benefit of all participants. This program also coordinates the ORNL activities with the other national laboratories, government agencies, university centers, and industry groups, including the Electric Power Research Institute.

Cooperative agreements ensure that technology development is industry-driven. The Office of Science and Technology Partnerships and patent counsel work together to place these agreements. Where appropriate, these efforts are coordinated with projects within ORNL that are funded by the DOE Office of Energy Research, as well as Work for Others and ORNL Director's Research and Development Fund projects. Effective funds-out to industry is used to supplement industry cost share. In FY 1995 more than $800,000 funds-out to industry and universities was provided through cooperative agreements and subcontracts. To keep industry involved from the start of the program and to ensure commercialization potential, these technology partnering mechanisms are augmented by CRADAs, user agreements, and licensing activities.

Responsiveness to American industry has high priority in this program. An ORNL ad hoc technical review committee, consisting of a program manager, a scientific coordinator, a manager for conductor development, and a manager for applications development, reviews all inquiries from industry and recommends a project for possible funding. This review ensures that (1) the proposed work fits the program mission, (2) the work is collaborative, (3) there is legitimate commercial interest, and (4) the work is feasible. Substantial private-sector cost share is required on cooperative agreements.

ORNL provides support to the DOE Headquarters (DOE-HQ) Superconductivity Program for Electric Power Systems by identifying, guiding, and monitoring research and development at ORNL and ORNL subcontractor sites and by performing coordination, analysis, and planning of activities

Table 3.2. Superconductivity Program—summary of cooperative agreements as of September 30, 1995

Participant	Approved term	Type[a]	Total agreement cost share ($ x 1000)			Technology area
			By DOE to ORNL	By DOE to industry	By industry	
Advanced Fuel Research (completed)	2/1/90–9/30/92	NFE	230	0	442	In-situ HTS film deposition monitor
American Magnetics (completed)	8/10/89–8/9/92	NFE	100	0	480	Char. of MOCVD deposited multifilament conductors
American Superconductor (completed)	9/1/91–11/15/96	FO	1139	650	710	Coil fabrication, tech. development, and testing
American Superconductor (completed)	4/1/89–11/15/96	FI	2090	0	1705.4	Fabrication of powder-in-tube wire and tape
Astronautics (completed)	9/1/91–2/28/95	FO	600	450	820	Magnetic refrigeration
CeraNova Corporation (completed)	8/1/93–1/31/95	FO	90	25	75	Melt-processed YBCO wire for leads and coils
Consultec Scientific (completed)	6/1/89–12/31/90	FO	38	45	64	Deposition target device
Corning (completed)	6/1/89–12/31/93	FO	325	275	316	Deposition on flexible ceramic substrates
CPS Superconductor (completed)	4/1/91–3/31/93	NFE	80	0	50	Conductor fab.—continuous filament melt-textured YBCO
Dow Corning (I-IIa) (completed)	7/1/90–9/31/91	FO	110	50	67	Thick film deposition
DuPont (completed)	7/1/89–3/31/91	NFE	225	0	250	Thin film devices and bulk applications
Electric Power Research Institute	7/13/93–7/12/96	C	176	0	4535	Variable speed superconducting motors, power electronics, and SMES; transmission cables (SPI)
Energy Conversion Devices (completed)	5/1/91–3/31/93	NFE	90	0	90	Deposition of conductors
General Electric (A1) (completed)	12/15/88–2/28/89	FI	5	0	45	Thallium HTS material processing
General Electric (SPI)	12/1/93–11/30/95	NFE	400	0	1173	Thallium wire development and generator design

Table 3.2 (continued)

Participant	Approved term	Type[a]	Total agreement cost share ($ x 1000)			Technology area
			By DOE to ORNL	By DOE to industry	By industry	
General Electric (B1)	10/1/89–12/31/95	FO	895	520	614	Laser deposition of conductors; thallium deposited conductors
General Electric (C1) (completed)	4/1/90–12/31/90	NFE	135	0	140	Thallium HTS material processing
HiTc Superconco (completed)	3/1/90–4/30/91	NFE	40	0	50	Magnetic bearings
Innovative Materials Technology (completed)	10/1/89–3/31/90	FI	50	0	50	Composite tape fabrication
Intermagnetics General Corp.	10/1/91–9/30/97	FO	1452	965	856	HTS transformer; BSCCO 2212 tape development
Intermagnetics General Corp. (completed)	9/1/91–8/31/94	NFE	100	0	100	Thallium powder-in-tube conductor
IBM (completed)	2/1/90–1/31/93	NFE	255	0	673	Optimize flux pinning via ion-induced defects
IBM (completed)	2/1/90–5/31/95	FO	201	389	186	Optimize flux pinning via ion-induced defects
Neocera (completed)	2/1/91–1/31/93	FO	80	111.6	95.7	Laser ablation multitarget deposition
Oxford Instruments	1/94–12/95	C	150	0	175	Develop technology for dip-coated BSCCO-2212 wire
Plastronic, Inc.	10/22/93–9/30/95	NFE	165	0	225	Apply wire-forming technology to produce BSCCO wire
Saphikon (completed)	2/1/92–4/30/94	NFE	50	0	492	Deposited conductor fabrication
SUNY-Buffalo (completed)	7/1/89–10/30/92	FO	165	250	255	Laser deposition of conductors
Stevens Institute of Technology (completed)	1/1/90–5/31/92	FO	90	105	100	MOCVD deposition for electronic devices
Superconductive Components, Inc.	3/15/95–3/14/97	NFE	25	0	25	Scale-up of the production of superconducting and precursor powders synthesized by aerosol decomposition method

Table 3.2 (continued)

Participant	Approved term	Type[a]	Total agreement cost share ($ x 1000)			Technology area
			By DOE to ORNL	By DOE to industry	By industry	
Superconductivity, Inc. (completed)	10/1/89–3/31/93	NFE	180	0	133	Magnetic energy storage for end-use applications
Textron Specialty Materials (completed)	8/1/89–3/31/91	NFE	60	0	45	Deposition of conductors
University of Wisconsin—Madison	8/1/92–9/30/95	FO	110	60	150	Aerosol powder synthesis
Westinghouse Electric (completed)	4/1/89–12/31/93	FO	1200	750	800	Powder scale-up, BSCCO wire fabrication, and leads
Total			11,101	4,645.6	15,987.1	
		FY 1993/94 subcontracts				
University of New Mexico	4/1/93–3/31/94			45		Study the generation of Pb-Bi-Sr-Ca-Cu-O (BSCCO) powders by aerosol decomposition
H. Hsu	11/15/93–11/14/94			48		Material synthesis and conductor fabrication
Imtech	9/23/94–9/22/95			65		Superconducting powder synthesis/scale-up
University of Tennessee	4/1/93–11/30/93			58		Advanced analytical electron microscopy techniques for HTS conductors
Georgia Institute of Technology	4/15/93–4/14/94			20		Study of combustion pyrolysis method for processing YBCO superconductors
SAIC	4/94–9/94			19		Prepare paper on evaluation of technology in Lab-industry partnership
National Institute of Standards and Technology (via Interagency Agreement)	8/93–7/95			200	200	BSCCO and TBCCO phase diagram support

[a]NFE = no-funds-exchange; FO = funds-out; FI = funds-in; and C = CRADA.

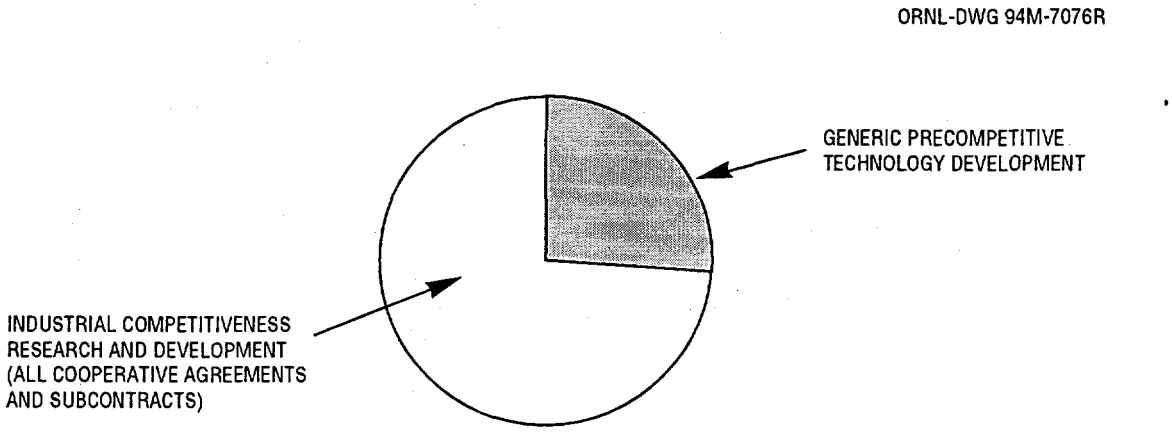

Fig. 3.1. ORNL funding distribution: FY 1995 new budget authorization and outlay.

related to the national program. Some of the various activities performed as part of this task include the following:

- technical, program, and budget guidance;
- project identification and development;
- exploratory research and development;
- support of consultants and subcontracts providing technical, program, or technology partnering support;
- identification, placement, and technical monitoring of subcontractors, review committee members, and workshop guests;
- guidance and support on technology partnering;
- publication of reports and proceedings from workshops;
- identification and initiation of cooperative agreements, interagency agreements (i.e., National Institute of Standards and Technology), and memoranda of understanding;
- distribution of reports to program managers;
- coordination of the Laboratory's Industrial Overview Committee;
- preparation of assessments to address technical, economic, regulatory, and institutional issues in the DOE program;
- coordination of interlaboratory technical team meetings;
- assistance to the DOE-HQ program manager in preparation of the Superconducting Technology Program Annual Operating Plan;
- assistance in the open annual review meeting preparations and contracting;
- collection and dissemination of programmatic information and program-wide assessments;
- assistance in organizing the Superconducting Technology Program workshops (one per year); and
- review of industrial collaboration opportunities through multilaboratory meetings and conference calls.

ORNL works with the other program laboratories to address issues such as communication among program participants, workshop and meeting implementation, planned

competitive solicitations and superconductivity agreements, and coordination of technical and economic assessments.

An Industrial Overview Committee is charged with reviewing program activities and advising Laboratory management as to program progress, policy, and direction. The committee consists of representatives of electric utilities, original equipment manufacturers, and HTS wire manufactures. This committee meets twice a year at ORNL, Argonne National Laboratory, or Los Alamos National Laboratory.

PROGRAM MEASURES

One new cooperative agreement was executed during FY 1995: Superconductive Components. New Statements of Work were negotiated, and agreements were extended with ASC, IGC, GE, and Oxford Instruments. Seven new invention disclosures were submitted by ORNL or industry principal investigators. These are listed in Table 3.3 together with all others for the program.

Table 3.3. Superconducting Technology Program invention disclosures

ESID No.	Subject	Submitted by
935-X	Method for Fabricating Continuous Ribbons of High-Temperature Superconductors	V. K. Sikka and C. E. Dunn
1018-X	Improved $Y_1Ba_2Cu_3O_7$ Superconductor	A. D. Marwick and L. Civale (IBM), and J. R. Thompson (ORNL)
964-X	Chemically Compatible Substrate/Jacket Alloy for Oxide Superconductors	D. M. Kroeger, F. A. List III, and J. Brynestad
1039-X	Method for Preparation of $(Bi\text{-}Pb)_2Sr_2Ca_2Cu_3$ Oxide Powders (Patent 5,395,821 issued 3/7/95)	D. M. Kroeger, J. Brynestad, and H. S. Hsu
1040-X	Method for Preparing Superconducting Wires from Oxide Powders	D. M. Kroeger and H. S. Hsu
1058-X	Rolled Current Density, High-Temperature Ribbon Superconductors from Stacked Predeposited Strips	G. A. Whitlow and J. C. Bowker (Westinghouse) and D. M. Kroeger and F. A. List III
1124-X	Improved, Strain-Tolerant High-Temperature Superconductor (87X-SD925C)[a]	G. A. Whitlow and W. R. Lobic (Westinghouse)
1129-X	An Improved Heat Treatment for Composite Conductors Using $Bi_2SR_2CaCu_2O_x$ Superconductor Material (87X-SD925C)[a]	J. C. Bowker and G. A. Whitlow (Westinghouse)
1131-X	Method of Forming Superconducting Joints Between Tapes of Oxide Superconductors (87X-SE934V)[a]	R. H. Arendt and K. W. Lay (GE)
1155-X	Method for Fabricating High-Current-Density, Oxide Superconductor Ribbons (HTSPC-001)[a]	V. K. Sikka
1185-X	Bipolar Pulse Field for Magnetic Refrigeration (Patent 5,357,756 issued 10/25/95)	M. S. Lubell
1193-X	Process for Fabricating Continuous Lengths of Superconductor (86X-SD925C)[a]	D. M. Kroeger and F. A. List III
1233-X	High-Current Density, High-Temperature Superconductors by Deformation of High-Density Materials (87X-SD925C)[a]	G. A. Whitlow, W. R. Lovic, and J. C. Bowker (Westinghouse), D. M. Kroeger and F. A. List III (ORNL)
1384-X	Process to Enhance Superconducting Phase Formation, Grain Alignment, and Fracture Properties of High-Temperature Superconductors	V. Selvamanickam and D. M. Kroeger
1450-X	Improved-Efficiency High-T_c Superconducting Magnet Lead Materials	R. K. Williams
1467-X	Superconducting Structure and Method for Making Same	R. K. Williams and J. Brynestad

Table 3.3 (continued)

ESID No.	Subject	Submitted by
1471-X	HTS Coil Grading to Compensate for Anisotropic Behavior of HTS Conductor (86X-SK700V)[a]	D. Aized and R. Schwall (American Superconductor)
1511-X	Enhancement of Persistent Currents in High-T_c Superconductors (86X-SF645V)[a]	L. Krusin-Elbaum, A. D. Marwick, and J. F. Ziegler (IBM), J. R. Thompson (ORNL), and P. Lisowsik (LANL)
1512-X	Method for Preparation of Textured $YBa_2Cu_3O_x$ Superconductor	V. Selvamanickam, A. Goyal, and D. M. Kroeger
1632-X	Materials and Fabrication Method for Producing High-T_c Superconducting Tapes (ORNL 93-0180)[a]	R. K. Williams (ORNL) and K. R. Marken, Jr. (Oxford)
1636-X	Low-Loss Multifilamentary Superconductor for ac Applications	M. S. Lubell
1638-X	Buffer Template for *c*-Axis-Oriented Perovskite Films on Crystalline Metals	David P. Norton and J. D. Budai
1640-X	Method of Fabricating High-Temperature Superconductors with Enhanced "Bi-Axial" Texture	A. Goyal, E. D. Specht, D. M. Kroeger, D. K. Christen, J. D. Budai, and D. P. Norton
1654-X	A Sol-Gel Process for Synthesis of Barium-Calcium-Copper-Oxide Superconductor Precursor	M. Paranthaman and D. B. Beach
1676-X	Torsional Texturing of Superconducting Oxide Substrates (86X-SK700V)[a]	C. J. Christopherson, G. N. Riley, and J. Scudiere (American Superconductor)
1687-X	Making a Transposed Cable out of High-Temperature Superconducting (HTS) Tapes	J. W. Lue
1697-X	Powder-in-Tube and Thick-Film Methods of Fabricating High-Temperature Superconductors Having Enhanced "Biaxial" Texture	A. Goyal and D. M. Kroeger
1770-X	Structures for High-J_c in a Magnetic Field with Arbitrary Orientation (86X-SK700V)	C. J. Christopherson and G. Snitchler (American Superconductor)
1784-X	Method of Preparing Preferentially Oriented, High-Temperature Superconductors by Seeding	D. F. Lee, A. Goyal, and D. M. Kroeger
1802-X	Low Thermal Conductance, High Thermal Capacity Support for High-T_c Superconducting Current Leads	R. K. Williams

[a]Numbers in parentheses are cooperative agreement numbers under which the work was conducted.

FY 1995 Presentations and Publications

L. J. Masur, E. R. Podtburg, C. A. Craven, and A. Otto (ASC), Z. L. Wang (NIST), D. M. Kroeger (ORNL), and J. Y. Coulter and M. P. Maley (LANL), "Bi-axial Texture in $Ca_{0.1}Ba_2Cu_4O_8$ Composite Wires Made by Metallic Precursors," *Physica C* **230**, 274–82 (1994).

M. Paranthaman, J. R. Thompson, J. Brynestad, and D. M. Kroeger (ORNL), and Y. R. Sun (UT), "Evidence for Phase Stability and Weak Links in Polycrystalline $HgBa_2CuO_{4+\delta}$," *Appl. Supercond.* **2**(5), 359–65 (1994).

E. D. Specht, A. Goyal, and D. M. Kroeger (ORNL), and J. A. DeLuca, J. E. Tkaczyk, C. L. Briant, and J. A. Sutliff (GE), "The Effect of Colonies of Aligned Grains on Critical Current in High-Temperature Superconductors," *Appl. Phys. Lett.*, submitted for publication.

A. Goyal, E. D. Specht, D. M. Kroeger (ORNL), and J. A. DeLuca, J. Sutliff, and J. E. Tkaczyk (GE), "Formation of Colonies of Locally Aligned Grains During Thallination of Spray-Pyrolyzed $Ba_2Ca_2Cu_3O_x$ Thick Films," presented at the Applied Superconductivity Conference, Boston Mass., Oct. 17–21, 1994; to be published in *IEEE Trans. Appl. Supercond.*

J. R. Thompson and D. K. Christen (ORNL), L. Krusin-Elbaum and A. D. Marwick (IBM), Y. C. Kim (UT), R. Wheeler (ANL), C. Li, S. Patel, and D. T. Shaw (NYSIS), and P. Lisowski and J. Ullmann (LANL), "Persistent Current Density and Flux Creep in Bi-Sr-Ca-Cu-O/Ag Tapes with Splayed Columnar Defects from 0.8 GeV Proton Irradiation," presented at the Applied Superconductivity Conference, Boston, Mass., Oct. 17–21, 1994; to be published in *IEEE Trans. Appl. Supercond.*

J. W. Lue, L. Dresner, and S. W. Schwenterly (ORNL), and D. Aized, J. M. Campbell, and R. E. Schwall (ASC), "Stability Measurements on a 1-T High-Temperature Superconducting Magnet," presented at the Applied Superconductivity Conference, Boston, Mass., Oct. 17–21, 1994; to be published in *IEEE Trans. Appl. Supercond.*

V. Selvamanickam (IGC) and C. Bamberger, P. M. Martin, and D. M. Kroeger (ORNL), "Improved Strain Tolerance in Aligned MgO-Whisker-Reinforced $(BiPb)_2Sr_2Ca_2Cu_3O_{10}$ Tapes," presented at the Applied Superconductivity Conference, Boston, Mass., Oct. 17–21, 1994; to be published in *IEEE Trans. on Appl. Supercond.*

V. Selvamanickam (IGC), P. M. Martin and D. M. Kroeger (ORNL), and M. Tomsic (Plastronic), "Fabrication of $(Bi,Pb)_2Sr_2Ca_2Cu_3O_{10}$ Tapes by a Tubular Wire Process," presented at the Applied Superconductivity Conference, Boston, Mass., Oct. 17–21, 1994; to be published in *IEEE Trans. Appl. Supercond.*

M. Paranthaman, A. Goyal, D. E. Heatherly, and D. M. Kroeger (ORNL), "Fabrication of Anisotropic Tl-1212, Tl-2212, Tl-1223, and Tl-2223 Particles Using Aerosol Flow Reacted Powders," presented at the Applied Superconductivity Conference, Boston, Mass., Oct. 17–21, 1994; to be published in *IEEE Trans. Appl. Supercond.*

A. Goyal (ORNL), "Advances in the Processing of High-Temperature Superconductors for Bulk Applications," *J. Met.*, Special Edition (December 1994).

D. M. Kroeger and A. Goyal (ORNL), "Models for Long-Range Current Flow in Polycrystalline High-J_c Oxide Superconductors," *J. Met.*, Special Edition (December 1994).

L. J. Masur, E. R. Podtburg, C. A. Craven, and A. Otto (ASC), Z. L. Wang (NIST), and D. M. Kroeger (ORNL), "Advances in Processing and Properties of $YBa_2Cu_4O_8$ Conductors," *J. Met.*, submitted for publication.

D. M. Kroeger, A. Goyal, and E. D. Specht (ORNL), J. E. Tkaczyk, J. Sutliff, and J. E. DeLuca (GE), Z. L. Wang (NIST), and G. N. Riley (ASC), "Local Texture and Grain Boundary Misorientations in High-J_c Oxide Superconductors," presented at the Proceedings of the 7th New York State Institute Conference on Superconductivity and Applications, Sept. 7–9, 1994, Buffalo, New York; to be published in the preceedings.

M. Paranthaman and D. B. Beach (ORNL), "Growth of Highly Oriented $TlBa_2Ca_2Cu_3O_{9-y}$ Superconducting Films on Ag Substrates Using a Dip-Coated Barium Calcium Copper Oxide Sol-Gel Precursor," *J. Am. Ceram. Soc.*, submitted for publication.

J. Brynestad, M. Paranthaman, A. Goyal, D. E. Heatherly, and D. M. Kroeger (ORNL), "Formation of Thallium-Based High-Temperature Superconductors Using Aerosol-Flow-Reacted Precursor Powders," presented at the Proceedings of Harald A. Oeye International Symposium, University of Trondheim, Norway, Feb. 2–3, 1995; to be published in the proceedings.

M. S. Walker, C. M. Trautwein, and L. R. Motowidlo (IGC), D. R. Dietderich (Lawrence Berkeley Laboratory), and F. A. List (ORNL), "Practical, Coated BSCCO-2212 High-T_c Superconductors," presented at the 1994 Applied Superconductivity Conference; to be published in *IEEE Trans. Appl. Supercond.*

A. Goyal and D. M. Kroeger (ORNL), Z. L. Wang (NIST), Y. R. Sun (UT), J. R. Thompson (ORNL and UT), and Y. T. Chou, J. Yun, and M. P. Harmer (Lehigh University), "Studies on Superplastically Deformed 123/Ag Composites," presented at the 1994 Applied Superconductivity Conference; *IEEE Trans. Appl. Supercond.* **5**, 1452 (1995).

A. Goyal, M. Paranthaman, Q. He, F. A. List, E. D. Specht, D. K. Christen, and D. M. Kroeger (ORNL), J. E. Tkacyzk (GE), and P. Haldar (IGC), "Fabrication, Processing, and Properties of Tl-1223 Conductors," presented at the 1994 Applied Superconductivity Conference; *IEEE Trans. Appl. Supercond.* **5**, 1405 (1995).

K. Salama and A. S. Parikh (TCSUH), and M. N. Kunchur and D. K. Christen (ORNL), "Processing and Properties of High-J_c Grain Boundaries in Melt-Textured $YBa_2Cu_3O_x$," submitted to Proceedings of the International Cryogenic Materials Conference, Oct. 24–26, 1994.

Y. C. Kim and Y. R. Sun (UT), J. R. Thompson (ORNL and UT), and D. K. Christen, M. Paranthaman, and E. D. Specht (ORNL), "Surface Barriers, Irreversibility Line, and Pancake Vortices in Aligned $HgBa_2Ca_2Cu_3O_{8+\delta}$ Superconductor," *Phys. Rev. B.*, submitted for publication.

E. C. Jones, D. K. Christen, D. P. Norton, and D. H. Lowndes (ORNL), "Conventional Behavior in the Upper Critical Field of 'Infinite-Layer' $Sr_{0.9}Nd_{0.1}CuO_{2-\delta}$, the Least Anisotropic High-T_c Superconductor," *Phys. Rev. Lett.*, submitted for publication.

Y. C. Kim (UT), J. R. Thompson (ORNL and UT), J. G. Ossandon (University of Talca), and D. K. Christen and M. Paranthaman (ORNL), "Equilibrium Superconducting Properties of Grain-Aligned $HgBa_2Ca_2Cu_3O_{8+\delta}$," *Phys. Rev. B.*, submitted for publication.

L. Krusin-Elbaum and C. Field (IBM Research Center), L. Civale (Centro Atomico Bariloche), and J. R. Thompson (ORNL and UT), "Accommodation of Vortices to Columnar Defects: Evidence for Large Entropic Reduction of Vortex Localization," *Phys. Rev. Lett.*, submitted for publication.

D. M. Kroeger, A. Goyal, and E. D. Specht (ORNL), *"Texture and Grain Boundary Misorientation Distributions in Polycrystalline HTS,"* invited abstract at the Cryogenic Engineering Conference and International Cryogenic Materials Conference, Columbus, Ohio, July 17–21, 1995.

A. Goyal, D. P. Norton, Q. He, J. D. Budai, E. D. Specht, D. M. Kroeger, M. Paranthaman, and D. K. Christen (ORNL), "Fabrication of Biaxially Aligned Polycrystalline HTSC Conductors," invited abstract at the Cryogenic Engineering Conference and International Cryogenic Materials Conference, Columbus, Ohio, July 17–21, 1995.

J. W. Lue and M. S. Lubell (ORNL), and D. Aized, J. M. Campbell, and R. E. Schwall (ASC),"Quenches in a High-Temperature Superconducting Pancake Coil," abstract submitted at the 14th International Conference on Magnet Technology, June 12–16, 1995, in Tampere, Finland, and to the Cryogenic Engineering Conference and International Cryogenic Materials Conference, Columbus Ohio, July 17–21, 1995.

D. K. Christen, Q. He, M. Paranthaman, C. E. Klabunde, R. Feenstra, A. Goyal, F. A. List, D. M. Kroeger, J. E. Tkaczyk, J. A. DeLuca, Z. F. Ren, and J. H. Wang (ORNL), "Superconducting Transport Properties of Tl-1223 Deposits on Polycrystalline Substrates," abstract submitted to the 1995 International Workshop on Superconductivity, Maui, Hawaii, June 1995.

L. Civale (Centro Atomico Bariloche), L. Krusin-Elbaum and C. Field (IBM Research Center), J. R. Thompson (ORNL and UT), and R. Wheeler and M. A. Kirk, (Argonne National Laboratory),"Arresting of Vortex Motion in YBaCuO Crystals with Splay in Columnar Defects," *Physica C* **2969**, 235–40 (1994).

Y. R. Sun, J. R. Thompson, J. Schwartz, D. K. Christen, Y. C. Kim, M. Paranthaman (ORNL), "Surface Barrier in Hg-Based Polycrystalline Superconductors," *Phys. Rev. B* **51**, 581 (1995).

T. P. Sheahen, R. E. Rosenthal, R. A. Hawsey, S. W. Freiman, and J. G. Daley (ORNL), "Evaluation of Technology Transfer by Peer Review," *J. Tech. Transfer* **19**(3-4), 100–109 (December 1994).

H. Safar, J. H. Cho, M. P. Maley, J. O. Willis, J. Y. Coulter, J. L. Ullmann, and P. W. Lisowski (LANL), G. N. Riley, Jr., and M. W. Rupich (ASC), J. R. Thompson (ORNL), and L. Krusin-Elbaum (IBM), "Enhancement of Transport Critical Current Densities at 75 K in Bi-2223/Ag Tapes by Means of Fission Tracks from Irradiation by 0.8 GeV Protons," *Appl. Phys. Lett.*, submitted for publication.

M. N. Kunchur, D. K. Christen, and C. E. Klabunde (ORNL), and K. Salama (TCSUH), "Exploring the Dissipative Regime of Superconductors for Practical Current-Lead Applications," *Appl. Phys. Lett.*, submitted for publication.

D. F. Lee (ORNL), A. Satpathy and K. Salama (TCSUH), and V. Selvamanickam (IGC), "Effect of Hot Isostatic Pressing on the Microstructure and Critical Current Density of Directional Solidified $YBa_2Cu_3O_x$ Superconductors," *Supercond. Sci. Technol.* (March 1995).

A. Goyal, E. D. Specht, and D. M. Kroeger (ORNL), T. A. Mason and D. J. Dingley (Texsem Corporation), and G. N. Riley (ASC), "Grain Boundary Misorientations and Percolative Current Paths in High-J_c Powder-in-Tube $(Bi,Pb)_2Sr_3Ca_3O_x$,"*Appl. Phys. Lett.*, submitted for publication.

J. E. Tkaczyk, J. A. Sutliff, J. A. DeLuca, P. J. Bednarczyk, and C. L. Briant (GE), Z. L. Wang (Georgia Tech), and A. Goyal, D. M. Kroeger, D. H. Lowndes, and E. D. Specht (ORNL), "Texture and Transport in Spray-Pyrolyzed $TlBa_2Ca_2Cu_3O_9$ Thick Films," *J Mat. Res.*, submitted for publication.

Y. Zhang, M. Mironova, and K. Salama (University of Houston), and D. F. Lee (ORNL), "Evidence of Enhanced Flux Pinning by Dislocations in Deformed Textured $Y_1Ba_2Cu_3O_x$ Superconductor," *J Appl. Phys.*, submitted for publication.

A. Goyal, E. Specht, D. M. Kroeger, and D. K. Christen (ORNL), and J. E. Tkaczyk, J. A. DeLuca, and J. A. Sutliff (GE), "Effect of the Colony Microstructure on Transport Critical Current of High J_c Tl-1223 Thick Films," submitted to 1995 ISTEC/MRS International Workshop on Superconductivity, Maui, Hawaii, June 18–21.

G. N. Riley, Jr., and C. J. Christopherson (ASC), "Advances in Twisted Filament Bi-2223 Composite Conductor," paper submitted to the 1995 ISTEC/MRS International Workshop on Superconductivity, Maui, Hawaii, June 18–21.

C. J. Christopherson and G. N. Riley, Jr. (ASC), "Development of Twisted High-Temperature Superconductor Composite Conductors," *Appl. Phys. Lett.* **66**(17), 2277–79 (Apr. 24, 1995).

D. K. Christen, Q. He (UT), M. Paranthaman, C. E. Klabunde, R. Feenstra, A. Goyal, F. A. List, and D. M. Kroeger (ORNL), J. E. Tkaczyk and J. A. DeLuca (GE), Z. F. Ren, C. A. Wang, and J. H. Wang (SUNY-Buffalo), "Superconducting Transport Properties of Tl-1223 Deposits on Polycrystalline Substrates," extended abstract presented at the 1995 International Workshop on Superconductivity, Maui, Hawaii, June 18–21.

C. K. Subramaniam and A. B. Kaiser (Victoria University of Wellington), and M. Paranthaman (ORNL), "Thermoelectric Power and Resistivity Measurements on Oxygen-Annealed $HgBa_2Ca_2Cu_3O_{8+\delta}$ Superconductors," *Phys. Rev. B* **51**, 1330 (Jan. 1, 1995).

H. A. Blackstead and D. B. Pulling (University of Notre Dame), and M. Paranthaman and J. Brynestad (ORNL), "Field- and Temperature-Dependent Surface Resistance of Superconducting Polycrystalline Multiple-Phase Hg-Ba-Ca-Cu-O: Evidence for Dirty-Limit Behavior," *Phys. Rev. B* **51**, 3783 (Feb. 1, 1995).

C. E. Vallet, M. Paranthaman, S. Shu, and D. B. Beach (ORNL), "AFM and STM Imaging of $YBa_2Cu_3O_{7-x}$ Thin Films," abstract presented at the Eighth International Conference on Scanning Tunneling Microscopy/Spectroscopy and Related Techniques, July 23–28, Snowmass Village, Colo.

M. Paranthaman, D. E. Heatherly, and P. M. Martin (ORNL), "Phase Evolution Studies of $(Tl,Pb)(Sr_{1.6}Ba_{0.4})Ca_2Cu_3O_y$ Superconductors," *Mater. Res. Bull.*, submitted for publication.

A. Goyal, E. D. Specht, and D. M. Kroeger (ORNL), "Effect of Texture on Grain Boundary Misorientation Distributions in Polycrystalline High-Temperature Superconductors," *Appl. Phys. Lett.*, submitted for publication.

D. M. Kroeger, A. Goyal, and E. D. Specht (ORNL), "Paths for Current Flow in Polycrystalline High-Temperature Superconductors," extended abstract submitted at the 1995 International Workshop on Superconductivity, June 18–21, Maui, Hawaii.

J. W. Lue and M. S. Lubell (ORNL), and D. Aized, J. M. Campbell, and R. E. Schwall (ASC), "Spontaneous Quenches of a High-Temperature Superconducting Pancake Coil," presented at the 14th International Conference on Magnet Technology, Tampere, Finland, June 11–16, 1995, and published in IEEE *Trans. on Magn.*

Y. C. Kim (UT), J. R. Thompson (UT and ORNL), and D. K. Christen, M. Paranthaman, and E. D. Specht (ORNL), "Enhanced Irreversibility Field and Current Stabilization by Pb Substitution in Aligned Tl-1223 High-T_c Superconductor," *Physica C*, submitted for publication.

R. A. Hawsey (ORNL) and J. G. Daley (DOE), "The U.S. Department of Energy's National Program on Wire Applications of High-Temperature Superconductors," *J. Met.* **47**(8) (August 1995).

A. Goyal, E. D. Specht, and D. M. Kroeger (ORNL), T. A. Mason and D. J. Dingley (Texsem Corporation), and G. N. Riley (ASC), "Microtexture and Mesotexture in High-J_c Bi-2223," invited paper in *J. Electron. Mater.*

J. W. Lue and M. S. Lubell (ORNL), and D. Aized, J. M. Campbell, and R. W. Schwall (ASC), "Quench Development in a High-Temperature Superconducting Tape," presented at the ICMC/CEC, Columbus, Ohio, July 17–21, 1995.

N. H. Hur and J. R. Thompson (ORNL and UT), B. C. Chakoumakos, M. Paranthaman, and D. K. Christen (ORNL), "Structure and Superconducting Properties of $(Tl_{0.8}Bi_{0.2})(Sr_{1.6}Ba_{0.4})Ca_2Cu_3O_{9-\delta}$," *Physica C*, submitted for publication.

Z. L. Wang (Georgia Institute of Technology), and D. H. Lowndes, D. K. Christen, D. M. Kroeger, C. E. Klabunde, and D. P. Norton (ORNL), "Growth-Induced Columnar Defects in $YBa_2Cu_3O_{7-x}$," *Physica C*, submitted for publication.

D. F. Lee (ORNL), A. Satpathy (TCSUH), V. Selvamanickam (IGC), and K. Salama (TCSUH), "The Effect of Hot Isostatic Pressing on the Microstructure and Critical Current Density of Directional Solidified $YBa_2Cu_3O_x$ Superconductors," *Supercond. Sci. Technol.* **8**, 423–29 (1995).

A. Goyal, D. P. Norton, Q. He (UT), M. Paranthaman, E. D. Specht, J. D. Budai, D. M. Kroeger, D. K. Christen, R. Feenstra, and J. R. Thompson (ORNL), "Fabrication of Biaxially Aligned Polycrystalline HTSC Using a New Process," invited abstract presented at the MRS Fall Meeting, November 27–December 1, 1995, Boston, Mass.

J. W. Lue and M. S. Lubell (ORNL), and D. Aized, J. M. Campbell, and R. E. Schwall (ASC), "Quenches in a High-Temperature Superconducting Tape and Pancake Coil," *Cryogenics*, accepted for publication .

J. R. Thompson, D. K. Christen, M. Paranthaman (ORNL), L. Krusin-Elbaum, A. D. Marwick (IBM), L. Civale (Centro Atomico Bariloche), R. Wheeler (Ohio State University), J. G. Ossandon (University of Talca), and P. Lisowski and J. Ullmann (LANL), "The Impact of Tailored Defects on Length Scales and Current Conduction in High T_c Superconductors," chapter in *Lectures in Physics*, ed. P. Klamut, J. Klamut, V. Beel, and B. Dabrowski, Springer-Verlag, Heidelberg, 1996.

J. R. Thompson, D. Paul, Z. L. Wang, D. M. Kroeger, and D. K. Christen (ORNL), "Thermal Stability and Annealing of Columnar Defects in $Bi_2Sr_2Ca_1Cu_2O_8$/Ag Superconductor," *Appl. Phys. Lett.* **67**, 1007 (1995).

Z. F. Ren, C. A. Wang, J. H. Wang (SUNY Buffalo), D. J. Miller, J. D. Hettinger, K. E. Gray (ANL), and D. K. Christen (ORNL), "Composition and Phase Development of Epitaxial Superconducting $Tl_{0.78}Bi_{0.22}Sr_{1.6}Ba_{0.4}Ca_1Cu_3O_{9-\delta}$ Thin Films by Laser Ablation and Postannealing," *Physica C*, submitted for publication.

S. P. Tirumala and K. Salama (University of Houston), and D. M. Kroeger and D. F. Lee (ORNL), "Reaction Kinetics and Thermomechanical Processing of Bi-2223 Tapes Made from Aerosol Precursors of Various Stoichiometry," abstract submitted at the MRS 1996 Spring Meeting, Apr. 8–12, San Francisco.

A. Goyal, D. P. Norton, E. D. Specht, M. Paranthaman, Q. He (UT), P. M. Martin, J. D. Budai, D. M. Kroeger, D. K. Christen, F. A. List, and J. R. Thompson (ORNL), "Fabrication of Biaxially Textured Superconductors Using the RABiTS Process," abstract submitted to the MRS 1996 Spring Meeting, Apr. 8–12, San Francisco.

E. Kadyrov and D. C. Larbalestier (University of Wisconsin), and D. K. Christen (ORNL), "Effect of Heavy-Ion Irradiation on the Critical Current Density of Nb–47 wt % Ti Thin Films," *Appl. Phys. Lett.*, submitted for publication.

Q. He, D. K. Christen, C. E. Klabunde, M. Paranthaman, J. R. Thompson, A. Goyal, and D. M. Kroeger (ORNL), and J. E. Tkaczyk, K. W. Lay, and A. J. Pedraza (GE), "High-Current Superconducting $Tl_1Ba_2Ca_2Cu_3O_y$ Thick Films on Polycrystalline Ag by Spin Coating," *Appl. Phys. Lett.* **67**, 294 (1995).

J. R. Thompson (ORNL and UT), D. Paul (Tennessee Tech), Z. L. Wang (Georgia Tech), and D. M. Kroeger and D. K. Christen (ORNL), "Thermal Stability and Annealing of Columnar Defects in $Bi_2Sr_2Ca_1Cu_2O_8$/Ag Superconductor," *Appl. Phys. Lett.* **67**(7), (Aug. 14, 1995).

J. E. Tkaczyk and K. W. Lay (GE Corporate Research and Development), and D. Schultz and P. A. Parilla (National Renewable Energy Laboratory), "Development of a Scalable Tl-1223 Tape Process—Thallination of Powder Precursor Coatings," presented at the ICMC/CEC, Columbus Ohio, July 17–21, 1995.

J. E. Tkaczyk, J. A. Sutliff, J. A. DeLuca, B. J. Bednarczyk, and C. L. Briant (GE Corporate Research and Development), Z. L. Wang (Georgia Tech), and A. Goyal, D. M. Kroeger, D. H. Lowndes, and E. D. Specht (ORNL), "Texture and Transport in Spray-Pyrolyzed $TlBa_2Ca_2Cu_3O_9$ Thick Films," *J. Mater. Res.* **10**(9) (September 1995).

M. N. Kunchur, D. K. Christen, and C. E. Klabunde (ORNL), and K. Salama (TCSUH), "Exploring the Dissipative Regime of Superconductors for Practical Current-Lead Applications," *Appl. Phys. Lett.* **67**(6) (Aug. 7, 1995).

M. Paranthaman and B. C. Chakoumakos (ORNL), "Crystal Chemistry of $HgBa_2Ca_{n-1}Cu_nO_{2n+2+\delta}$($n$ = 1,2,3,4) Superconductors," *J. Solid State Chem.*, submitted for publication.

E. D. Specht, A. Goyal, and D. M. Kroeger (ORNL), "2D and 3D Percolation in High-Temperature Superconductors," *Physica C*, submitted for publication.

INTERNAL DISTRIBUTION

1. E. E. Bloom
2. J. D. Budai
3. D. K. Christen
4. D. F. Craig
5. L. M. Dickens
6. A. Goyal
7–16. R. A. Hawsey
17. Q. He
18. E. C. Jones
19. D. M. Kroeger
20. D. F. Lee
21. F. A. List III
22. M. S. Lubell
23. J. W. Lue
24. P. M. Martin
25. B. W. McConnell
26. D. P. Norton
27. W. P. Painter
28. M. Paranthaman
29. J. B. Roberto
30. B. Saffian
31. A. C. Schaffhauser
32. S. W. Schwenterly
33. J. Sheffield
34. S. S. Shoup
35. V. K. Sikka
36. E. D. Specht
37. J. O. Stiegler
38–41. J. W. Turner
42. J. VanCoevering
43. R. K. Williams
44–45. Laboratory Records Dept.
46. Laboratory Records—RC
47. Central Research Library

EXTERNAL DISTRIBUTION

48. U. Balachandran, Argonne National Laboratory, ET/212, 9700 South Cass Avenue, Argonne, IL 60439-4838
49. R. D. Blaugher, National Renewable Energy Laboratory, 1617 Cole Boulevard, Golden, CO 80401
50. J. W. Bray, General Electric Corporate Research and Development, Building K-1, Room 1C25, P.O. Box 8, Schenectady, NY 12301
51. J. G. Daley, EE-142/FORS, U.S. Department of Energy, Office of Utility Technologies, 6H-34, 1000 Independence Avenue, S.W., Washington, DC 20585-0121
52. R. Eaton, EE-142/FORS, U.S. Department of Energy, Office of Utility Technologies, 6H-034, 1000 Independence Avenue, S.W., Washington, DC 2085-0121
53. J. R. Gaines, Jr., Superconductive Components, Inc., 1145 Chesapeake Avenue, Columbus, OH 43212
54. P. M. Grant, Electric Power Research Insititute, P.O. Box 10412, Palo Alto, CA 94303
55. J. E. Hack, Midwest Superconductivity, Inc., 1315 Wakarusa Drive, Lawrence, KS 66049
56. P. Haldar, Intermagnetics General Corporation, P.O. Box 461, Latham, NY 12110-0461
57. R. L. Hughey, Jr., Southwire Company, One Southwire Drive, Carrollton, GA 30119
58. R. C. Johnson, Rochester Gas and Electric, 89 East Avenue, Rochester, NY 14649-0001
59. D. C. Larbalestier, University of Wisconsin–Madison, Applied Superconductivity Center, 1500 Johnson Drive, Madison, WI 53706
60. K. W. Lay, General Electric Corporate Research and Development, Building K-1, Room 1C25, P.O. Box 8, Schenectady, NY 12301

61. W. C. Lin, U.S. Department of Energy, Office of Assistant Manager for Energy Research and Development, Oak Ridge Field Office, P.O. Box 2008, Oak Ridge, TN 37831-6269
62. K. R. Marken, Jr., Oxford Superconducting Technology, P.O. Box 429, Carteret, NJ 07008-0429
63. C. Matzdorf, Energetics, Inc., 7164 Columbia Gateway Drive, Columbia, MD 21046
64. S. P. Mehta, Waukesha Electric Systems, 400 S. Prairie Ave., Waukesha, WI 53186-5937
65. D. M. Moon, Westinghouse Electric Corporation, Science and Technology Center, 1310 Beulah Road, Pittsburgh, PA 15235-5098
66. J. W. Muehlhauser, University of Tennessee Space Institute, B. H. Goethert Parkway, MS 8, Tullahoma, TN 37388-8897
67. D. E. Peterson, Los Alamos National Laboratory, Superconductivity Technology Center, P.O. Box 1663, MS K763, Los Alamos, NM 87545
68. C. Platt, EE-142/FORS, U.S. Department of Energy, Office of Utility Technologies, 6H-034, 1000 Independence Avenue, S.W., Washington, DC 2085-0121
69. G. B. Riley, American Superconductor Corporation, Two Technology Drive, Westborough, MA 01581
70. C. H. Rosner, Intermagnetics General Corporation, P.O. Box 461, Latham, NY 12110-0461
71. E. Peter Roth, Sandia National Laboratories, MS 0752, P.O. Box 5800, Albuquerque, NM 87185-0752
72. D. Driscoll, Reliance Electric Co., 24800 Tungsten Road, Cleveland, OH 44117
73. U. K. Sinha, Southwire Company, One Southwire Drive, Carrollton, GA 30119
74. G. Snitchler, American Superconductor Corporation, Two Technology Drive, Westborough, MA 01581
75. J. E. Tkaczyk, General Electric Corporate Research and Development, Building K-1, Room 1C25, P.O. Box 8, Schenectady, NY 12301
76. M. J. Tomsic, Plastronic, Inc., 35 Marybill Drive, Troy, OH 45373
77–78. U.S. Department of Energy, Office of Scientific and Technical Information, P.O. Box 62, Oak Ridge, TN 37831-0062
79. T. Vanderah, National Institute of Standards and Technology, Ceramics Division, Building 223, A-256, Gaithersburg, MD 20899
80. M. S. Walker, Intermagnetics General Corporation, P.O. Box 461, Latham, NY 12110-0461
81. D. O. Welch, Brookhaven National Laboratory, Materials Science Division, Upton, Long Island, NY 11973
82. G. J. Yurek, American Superconductor Corporation, Two Technology Drive, Westborough, MA 01581